ABSTRACT

Title of thesis: ROTORCRAFT BROWNOUT MITIGATION THROUGH FLIGHT PATH OPTIMIZATION USING A HIGH FIDELITY ROTORCRAFT SIMULATION MODEL

Jillian Alfred, 2012

Thesis directed by: Professor Roberto Celi
Department of Aerospace Engineering

Brownout conditions often occur during approach, landing, and take off in arid climates and involve the entrainment of loose sediment and dust into the rotor flow field. Research into brownout mitigation through operational means such as flight management have presented significant steps forward in reaching possible methods, but the approaches include many simplifications and assumptions in modeling the rotorcraft, as well as the approach profiles. This thesis describes a rotorcraft brownout mitigation study through flight path optimization using a high fidelity rotorcraft model. A flight dynamics model was coupled to a free-vortex method (FVM) model and particle tracking model to more accurately calculate the aerodynamics of the rotor with a full rotorcraft model. In addition to the model coupling, an approach profile following method was developed for the time-integration to specify the path of the rotorcraft through space. An optimization study was then performed using this flight dynamics model in a comprehensive brownout simulation. The optimization found a local shallow optimum approach and a global steep

optimum approach minimized the intensity of the resulting brownout clouds. These results confirmed previous mitigation studies and operational methods. The results also demonstrated that the addition of a full rotorcraft model into the brownout simulation changed the characteristics of the velocity field, and hence changing the characteristics of the brownout cloud is produced.

ROTORCRAFT BROWNOUT MITIGATION THROUGH FLIGHT PATH OPTIMIZATION USING A HIGH FIDELITY ROTORCRAFT SIMULATION MODEL

by

Jillian Samantha Alfred

Thesis submitted to the Faculty of the Graduate School of the
University of Maryland, College Park in partial fulfillment
of the requirements for the degree of
Master of Science
2012

Advisory Committee:
Dr. Roberto Celi
Dr. J. Gordon Leishman
Dr. Inder Chopra

Dedicated to my parents

Thanks for pushing me all these years

Acknowledgments

First and foremost I would like to thank my advisor, Dr. Roberto Celi, for his consistent support and advice throughout this process. I would also like to give thanks to Dr. J. Gordon Leishman for bring me into the brownout group, and allowing me to further the current research being done on this incredibly interesting topic. In addition, I need to thank my other committee member, Dr. Inderjit Chopra.

Secondly, I would like to give thanks to all the people in the lab that I have had the pleasure of working with these past couple of years. My research would not have been possible with out the consistent help of and support of John Tritschler who pioneered the methods of my research. I so much appreciate that even though with a wife and two kids and a job, you were found time to answer all my crazy emails and video chats in my time of need. I would also like to give my appreciation to Ananth Sridharan for all his help with HeliUM and helping me get through all those moments when I was ready to throw the computer out the window. Additionally, I'd like to thank Monica Syal and Bharath Govindarajan for answering my millions of questions throughout this process. Moreover, I would like to thank the rest of the gang in the lab including Hunter Nelson, Will Staruk, Joe Schmaus, and Jüergen Rauleder who all provide an endless source of procrastination and discussion.

I am also very grateful to my parents, Ken and Toby Alfred, for supporting me all these years and allowing me to follow my dreams. Last but certainly not least, I would like to thank my boyfriend, Jeremy Knittel, for his constant support

throughout this whole process and helping me keep my mental stability. I could not have gotten through this without him.

To any one I might have forgotten, you know who you are. Thanks!

Table of Contents

List of Tables

List of Figures

List of Symbols

Symbols

$\mathbf{A}$	State matrix
$\mathbf{B}$	Control matrix
$B(\mathbf{X})$	Objective function
C_T	Thrust coefficient
$d\mathbf{l}$	Vortex element
$\mathbf{e}$	Error vector
$\hat{\mathbf{e}}_x,\ \hat{\mathbf{e}}_y,\ \hat{\mathbf{e}}_z$	Unit vector of undeformed preconed blade reference frame
$\hat{\mathbf{e}}'_x,\ \hat{\mathbf{e}}'_y,\ \hat{\mathbf{e}}'_z$	Unit vector of deformed blade reference frame
$g_j(\mathbf{X})$	Behavior constraint
$I_{b_{i,j}}$	Bound vortices influence matrices
$I_{NW_{i,j}}$	Near wake influence matrices
J	LQR cost function
$\mathbf{K}$	Controller matrix
K_{set}	Set of controllers based on flight path angle
K_{spd}	Set of controllers based on flight speeds
M	Blade mode number
N	Blade harmonic number
N_b	Number of blades
N_s	Number of spanwise segments on each blade
p	Roll rate of the fuselage
$\mathbf{p}_{app}$	Boundary of discrete points on the approach profile
$\mathbf{p}_{VRS}$	Boundary of discrete points for the VRS constraint
$\mathbf{p}_{HV}$	Boundary of discrete points for the HV constraint
Q	State weighting matrix
$\mathbf{q}$	Blade section applied moment vector
q	Pitch rate of the fuselage
$\mathbf{R}_B$	Position vector
R	Main rotor radius
R	Controls weighting matrix
$\mathbf{r}$	Position vector to point 'P'
$\mathbf{r}$	Reference vector
r	Yaw rate of the fuselage
r_{pd}	Peak range of acceleration
t	Time
$\mathbf{u}$	Control vector
u	Longitudinal component of velocity
$\mathbf{V}_\infty$	Free stream velocity
$\mathbf{V}$	Velocity at a point in space
v	Lateral component of velocity

v_0	Initial velocity
w	Vertical component of velocity
w_{tip}	Flapping displacement of the undeformed blade
$\mathbf{X}$	Trim vector
$\mathbf{X}_B$	Body trim states
$\mathbf{X}_I$	Inflow trim states
$\mathbf{X}_R$	Rotor trim states
$\mathbf{X}_0$	Initial trim solution
x	Longitudinal position
x_{state}	Actual state vector
$\mathbf{y}$	State vector
y	Lateral position
z	Vertical position

α	Fuselage pitch angle
α_{app}	Approach angle
β	Blade flapping angle
β_p	Blade precone angle
β_{1c}	Longitudinal flapping
β_{1s}	Lateral flapping
β	Side slip angle
Γ	Vortex strength
γ	Flight path angle
δ_{1c}	Lateral cyclic pilot stick input
δ_{1s}	Longitudinal cyclic pilot stick input
δ_0	Collective pilot stick input
δ_t	Tail rotor collective pilot stick input
$\boldsymbol{\epsilon}$	Residual vector
ζ	Wake age of the filament
θ_0	Collective
θ_{1c}	Lateral cyclic
θ_{1s}	Longitudinal cyclic
θ	Pitch angle
λ_t	Tail rotor inflow
ϕ	Roll angle
Ψ	Azimuthal position of the blade
ψ	Yaw angle
Ω	Main rotor rotational speed
$\vec{\omega}$	Vorticity

Subscripts

$(..)_B$	Rigid body states
$(..)_{BM}$	Blade motion
$(..)_F$	Fuselage reference frame
$(..)_{FVM}$	FVM model reference
$(..)_{man}$	Maneuver
$(..)^{N_h}$	Number of harmonics
$(..)_R$	Rotor states
$(..)_\infty$	Free-stream
$\dot{(..)}$	Time derivative

Abbreviations

AC	Aerodynamic Center
AE	Algebraic Equation
CFD	Computational Fluid Dynamics
CG	Center of Gravity
CPU	Central Processing Unit
CUDA	Compute Unified Device Architecture
EA	Elastic Axis
FOV	Field of Vision
FVM	Free Vortex Method
GPU	Graphic Processing Unit
HHC	Higher Harmonic Control
HV	Height-Velocity
IGE	In-Ground-Effect
LQR	Linear Quadratic Regulator
MPI	Message Passing Interface
NASA	National Aeronautics and Space Administration
ODE	Ordinary Differential Equation
PC2B	Predictor-Corrector, Two-Point Backward
RAM	Random Access Memory
VRS	Vortex Ring State

Chapter 1

Introduction

1.1 Rotorcraft Brownout

Rotorcraft brownout is the condition in which the flow field of a rotorcraft while operating during maneuvers such as approach, landing, or take off in desert or dry, dusty environments, uplifts sediment particles from the ground and generates a cloud that obscures the pilot's field of view (FOV) (Fig. 1.1). In many cases, these obscurations result in the degradation of visual cues and give motion cue anomalies that affect the pilot's ability to safely fly the rotorcraft. In fact, studies have shown that the occurrence of brownout is the leading cause of human-factor related helicopter mishaps during military operations [1].

Brownout Cloud Development

Brownout is a complex two-phase fluids phenomenon involving dust clouds that evolve in space- and time. Figure 1.2 shows the relationship between the in-ground-effect (IGE) aerodynamics of a hovering helicopter and the development of a brownout cloud, with a few of the known primary physical mechanisms for development of the cloud being identified. The combination of downwash flow from the rotor and the proximity of the rotor wake vortices to the bed of dust (sediment) induces an unsteady velocity field that has the ability to cause the motion of the

Figure 1.1: A helicopter encountering brownout conditions during a landing maneuver (courtesy of Optical Air Data Systems LLC) [2].

loose sediment. A good understanding of the characteristics of the rotor flow field during IGE operations is important because the rotor wake is responsible for the various fluid dynamic forces that mobilize and uplift the dust particles. Such forces involve shear, pressure, turbulence, interparticle cohesion, and gravity [3].

The flow field that results from a rotor operating in ground-effect, even in the absence of sediment particles, is very complicated. A flow visualization image and schematic diagram of IGE rotor flow is shown in Fig. 1.3. As the flow field approaches the ground plane, the swirl velocities of the tip vortices increase in intensity. This intensification because of stretching counters the typical diffusive behavior of the tip vortices that can be seen in out-of-ground-effect (OGE) flow, and causes the vortices to persist in the flow for much longer. The persistence of the vortices is now known to significantly impact the development of a brownout

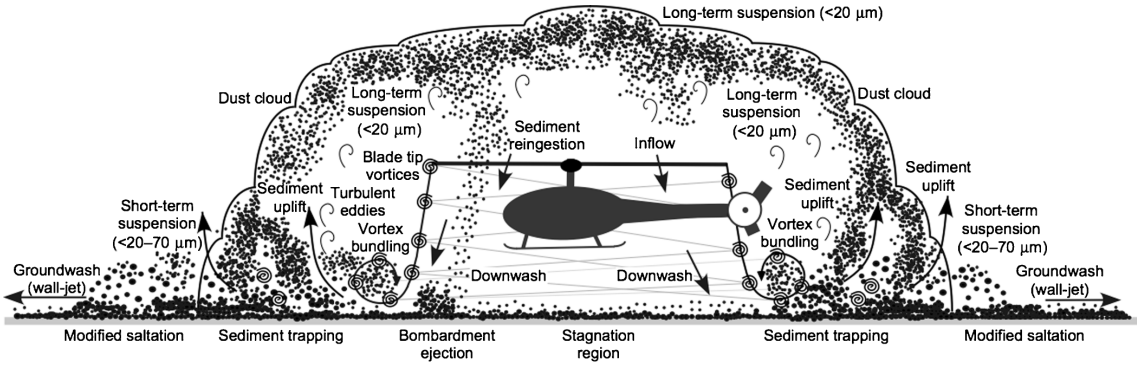

Figure 1.2: A schematic of in-ground-effect aerodynamics and the brownout problem [2].

cloud [4], [5].

When the IGE rotor flow interacts with a sediment bed, several sediment transport mechanisms are known to contribute to the development of a brownout dust cloud. Figure 1.4 shows a few of these mechanisms. Once mobilized, particles are rapidly convected away by the three-dimensional, turbulent, unsteady flow. Larger particles tend to be suspended for shorter durations, while smaller particles can remain in long-term suspension. In some instances, suspended particles may be recirculated through the rotor disk and consequently impact the ground and eject many more particles by means of bombardment ejections. In fact, bombardment has been shown to be one of the more important mechanisms in the formation of brownout dust clouds [7]-[9].

Im principle at least, it is possible to change the characteristics of the brownout cloud by altering the IGE flow. By changing the time over which the rotor wake is impinging on the ground, as well as at what angle the flow hits the ground, more

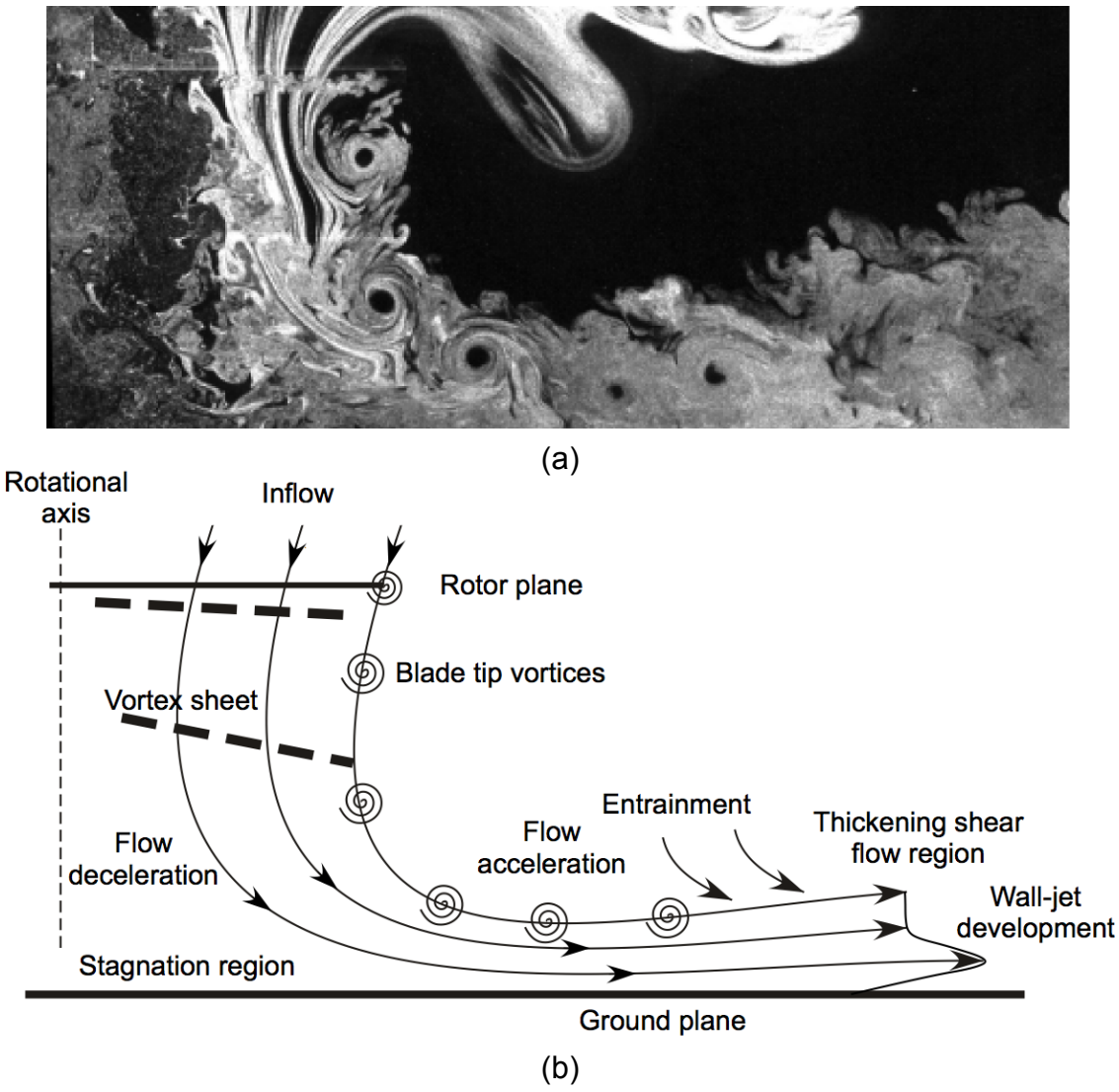

Figure 1.3: A rotor in ground-effect: (a) flow visualization and (b) schematic diagram [6].

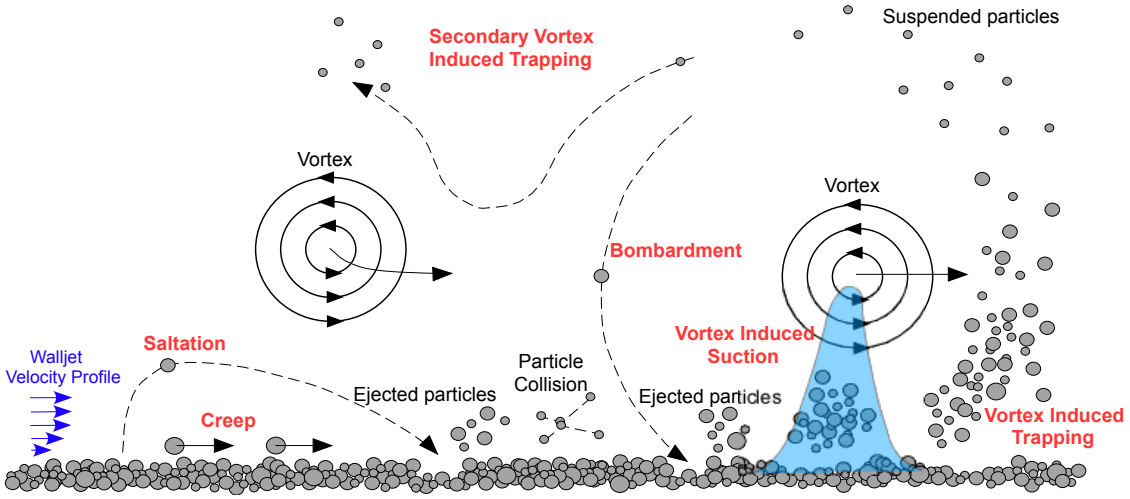

Figure 1.4: Schematic showing the different modes of dust particle motion and the fundamental uplift mechanisms seen in the near-wall region [5].

or less sediment particles will be uplifted. To this end, certain takeoff and landing techniques have been employed to minimize the severity of the developing brownout cloud. For example, pilots have adopted strategies such as attempting to "outrun" the cloud so that pilot's field of view (FOV) remains clear for a majority of the maneuver. While these strategies are generally accepted among pilots, they are the result of experience and have not been confirmed by means of models.

1.2 Literature Review

The present research can be separated into two major areas: brownout simulation and rotorcraft dynamics simulation. The breadth of brownout research is quite broad because of the multidisciplinary nature of the brownout problem. Research on brownout has been done in the fields of measurement and characterization, modeling and simulation, experimentation, sensors and cueing aids, and maintenance

considerations [2]. In recent years, several comprehensive flight dynamics simulation models have been developed in industry, academia, and research institutions [15]. The following section details the previous work in brownout and rotorcraft dynamics simulations that led to the specific development of the methodology used in this thesis work.

1.2.1 Brownout Research

In the field of brownout cloud modeling and simulation, Syal et al. [10] developed a Lagrangian dust cloud simulation methodology. A Lagrangian Free Vortex Method (FVM) was coupled to a viscous semi-empirical approximation for the boundary layer flow near the ground, and modeled the flow field generated by an isolated main rotor in ground effect operations over a sediment bed. The model included several mechanisms of particle entrainment, including shear forces, pressure forces, and bombardment ejections. A numerically efficient particle tracking methodology was developed where individual particles or clusters of particles were tracked in the flow. The methodology was validated against available measurements, including flow field measurements that have been made with laboratory- and full-scale rotors in ground effect conditions. The predicted dust clouds were also compared against measurements of developing dust clouds produced by a helicopter during different flight maneuvers and demonstrated good agreement.

Hu et al. [11] improved upon the computational efficiency of the dust cloud calculations through parallelization of graphics processing units (GPUs) and algo-

rithmic modifications to drastically decrease computational times. This model was utilized by Kalra et al. [12] and Thomas et al. [13], coupling the dust cloud methodology to a CFD-based methodology for modeling a hovering rotor in ground effect. The dust cloud methodology was further extended by Syal et al. [14] to examine the possibility of brownout mitigation using a slotted-tip blade by implementing a semi-empirical modification to the tip vortex characteristics. Based on the analysis of the dust clouds it was shown that with a slotted-tip blade fewer particles were mobilized from the sediment bed, and the overall density of the brownout cloud within the critical regions of the pilot's FOV was generally lower.

Tritschler et al. [2] employed the dust cloud simulation to develop a methodology for operational brownout mitigation through flight path optimization. The coupled FVM model and dust cloud model was used to simulate the effect of different landing approach profiles on the brownout cloud. A metric for the overall density of the cloud was created based on a time-averaged density of the dust particles in the pilot's FOV. It was for this metric that the flight path was optimized. This study found that the optimizer "preferred" flight profiles that were much more aggressive than typical flight profiles used by pilots. These profiles favored methods that would either "outrun" the cloud at shallow approach angles, or land at steeper angles that minimized the amount of time that the rotor wake was in contact with the ground. Operationally, these"preferred" approaches correlated well with the approaches that pilots tend to use in the field.

Tritschler's methodology provided a significant step for studying methods of possible operational mitigation of brownout, a field in which very little academic

research has been done. However, this study included sevel modeling simplifications and the rotorcraft model consisted of only an isolated main rotor. To reach the next step in mitigation studies, a more detailed model of the helicopter is required. A fundamental aim of the present research is to couple a more detailed, high-fidelity rotorcraft flight dynamics model with Tritschler's methodology for brownout mitigation.

1.2.2 Rotorcraft Dynamics Simulation

The flight dynamics model used in the present study, also known as HeliUM in its current implementation, has been developed at the University of Maryland over several years. Cheng [15] presented a brief history of the simulation model, and it is summarized here along with further developments since then.

The model is originally from the helicopter simulation model GenHel [16], specialized for the Sikorsky UH-60 Black Hawk. The rotor was modeled with a rigid blade flap and lag degrees-of-freedom, and the torsional dynamics using a pseudo-modal approach. The fuselage was modeled as a rigid body with aerodynamic coefficients of the fuselage and empennage provided by a look-up table. The fidelity of the GenHel model was improved by Ballin [17] who implemented the engine model and Kim [18], [19] who included the main rotor inflow model using the Pitt-Peters dynamic inflow model. A new trim procedure was also developed with the equations of motion presented in first-order state-space form, which allowed for a linear time-invariant model to be extracted using a perturbation averaging method.

This version of the model, named UM-GenHel, was calibrated based on actual flight test data and is widely used in flight dynamics analysis at NASA Ames Research Center.

The model has continued to be developed at the University of Maryland as a research tool. Turnour [20] extended the rotor blade modeling of UM-GenHel by including the aeroelastic rotor, which was originally developed by Celi [21] and extended by Spence [22] to include the coupled rotor-fuselage formulation. Turnour also added the finite state wake [23] and the Leishman-Nguyen [24] state-space unsteady aerodynamics model. Theodore [25] extended the inflow model to include the maneuvering Free Vortex Wake model [26] as a replacement for the dynamic inflow model.

The simulation was reworked by Fusato [27] for a new implicit formulation of the equations of motions, which made the simulation model more flexible and modular. Cheng [15] introduced Higher-Harmonic Control (HHC) to the simulation, that consisted of superimposing high frequency inputs over the conventional low frequency inputs used to control and manuever the helicopter. Ribera [28] further improved upon the wake model, adding the Bhagwat-Leishman [24] time-marching free-vortex wake model. After Ribera, the simulation was updated from Fortran 77 to Fortran 95, and the Free Wake models were uncoupled from the simulation. Juhasz [30] extended the simulation for the XV-15, which included a rigid and flexible wing model.

1.3 Research Objectives

The objectives of the present research were:

1. To recouple the Free Vortex Method (FVM) model to the flight dynamics simulation to create a high-fidelity rotorcraft model. Furthermore, to optimize the trim procedure and validate the results with flight test data.

2. To develop a methodology for approach profile following during time-integration of the flight dynamics model.

3. To apply the coupled high fidelity model to the brownout mitigation though flight path optimization methodology presented by Tischler et al. [2] and compare the results.

1.4 Thesis Organization

This thesis is divided into five chapters. The first chapter describes the basic problem of brownout and why it occurs. It further describes the brownout mitigation procedures and simulations that provide the background and basis for the present work.

The second chapter describes the methodology of the entire brownout mitigation simulation. This methodology contains a description of both the flight dynamics and FVM models and their subsequent coupling, along with a description of the dust cloud simulation and the optimization procedure.

The third chapter presents the validation of the coupling of the flight dynamics

and FVM models. It also presents the results of the approach profile implementation. The results of the brownout mitigation through flight path optimization study are also presented in this chapter. In addition, an interpretation of the results is presented.

The forth and final chapter gives a summary of the conclusions drawn from the coupling of the models as well as the optimization and recommendations for future research.

Chapter 2

Methodology

2.1 Overview

The brownout mitigation simulation approach takes place within a numerical optimization framework which consists of three steps. First, the rotor wake corresponding to the desired landing maneuver is calculated using the helicopter flight dynamics model coupled with the wake model. The resulting wake determines the flow field surrounding the rotor and close to the ground. Second, the motion of the dust particles generated by the flow field is computed. Last, an objective function based on the dust particle's geometry is calculated and a numerical optimizer is used to create a new desired landing maneuver. The process is repeated until the desired level of convergence of the objective function is reached. The basis of this process has been described in [2], and the key elements and modifications to the process will be discussed here.

2.2 High-Fidelity Helicopter Flight Dynamics Modeling

A high-fidelity helicopter flight dynamics model is used to accurately model the states of the helicopter during the maneuver. The model consists of main rotor and fuselage equations of motion, as well as the tail rotor inflow dynamics. In addition,

the main rotor consists of flexible blades that are discretized using a finite-element method. This section contains a brief summary of the main assumptions used, as well as the rotor and fuselage equations of motion. A full description of the model can be found in [31].

2.2.1 Overview

The mathematical model used in this study describes the rigid body dynamics of the aircraft, the coupled flap-lag-torsion-axial dynamics of each main rotor blade, and the inflow dynamics of the main rotor and the tail rotor. With the exception of the free vortex wake, the mathematical model is formulated as a system of first-order, coupled, non-linear ordinary differential equations of the form:

$$\dot{\mathbf{y}} = \mathbf{f}(\mathbf{y},\ \mathbf{u};\ t) \tag{2.1}$$

where $\mathbf{y}$ is a vector of states, $\mathbf{u}$ is a vector of controls, and t is time. The coupled wake does not contribute any additional dynamic equations to the basic first-order form of the equations of motion. The wake model is discussed in more depth in the following sections.

The state vector $\mathbf{y}$ takes the form (for a four-bladed rotor):

$$\mathbf{y}(\psi_i) = [u\ \ v\ \ w\ \ p\ \ q\ \ r\ \ \phi_F\ \ \theta_F\ \ \psi_F\ \ \lambda_t\ \ q_1^1\ \ q_2^1\ \ q_3^1\ \ q_4^1\ \ \dot{q}_1^1\ \ \dot{q}_2^1\ \ \dot{q}_3^1\ \ \dot{q}_4^1 \tag{2.2}$$

$$...q_1^{N_h}\ \ q_2^{N_h}\ \ q_3^{N_h}\ \ q_4^{N_h}\ \ \dot{q}_1^{N_h}\ \ \dot{q}_2^{N_h}\ \ \dot{q}_3^{N_h}\ \ \dot{q}_4^{N_h}] \tag{2.3}$$

in which u, v, w, p, q and r are the velocities and rates in the body fixed coordinate system; ϕ_F, θ_F, and ψ_F are the Euler angles of the fuselage; λ_t is the tail rotor inflow; and q_i^k and $\dot{q}_i^k$ are the generalized displacement and velocity coordinates for blade i and normal mode k in the rotating frame at the azimuth angle ψ_i.

The control vector $\mathbf{u}$ is defined as:

$$\mathbf{u} = [\delta_{1c} \;\; \delta_{1s} \;\; \delta_0 \;\; \delta_t] \tag{2.4}$$

which correspond to the pilot's stick inputs for the lateral and longitudinal cyclic pitch, and the collective pitch controls for the main and tail rotors.

The model is formulated as a series of nested loops, the order from outermost to innermost is as follows: over the rotors, blades, finite-elements, and Gaussian points within the element.

2.2.2 Main Assumptions

The main assumptions made in the formulation of the mathematical model used for the present research are listed below [31]:

1. The undeformed blade is straight with no sweep, droop, or torque offsets.

2. The external wind velocity is zero.

3. The airframe is a rigid body with a constant mass and a uniform mass distribution; the $X - Z$ plane is a plane of symmetry.

4. For the standard four-bladed, utility helicopter configuration, the pitch angle

of the horizontal stabilizer is fixed for a given flight condition, and the control logic for the automatic positioning of the horizontal stabilizer is not modeled.

5. The fuselage and tail surface aerodynamics are derived from wind tunnel tests without the main rotor. The aerodynamic coefficients are provided in the form of look-up tables as functions of angle attack and sideslip, which are not necessarily small angles. Stall, compressibility, and unsteady aerodynamic effects are neglected for the fuselage and tail

6. The blades are assumed to be rigid in flap, lag and torsion inboard of the flap and lag hinges, and the respective hinges are coincident.

7. The blade cross-sections are symmetric with respect to the major principal axes.

8. The blade cross-sectional area centroid and elastic axes are coincident, which means that the tension center is coincident with the elastic axis. However, cross-sectional centers of gravity (CG), aerodynamic centers (AC), and elastic axes (EA) need not be coincident.

9. Blade chord, built-in twist, stiffness and mass properties, and cross-sectional offsets are defined at discrete spanwise stations, and vary linearly in between.

10. The blade is built of an isotropic, linearly elastic material.

11. Bernoulli-Euler beam theory is used, implying that plane cross sections remain plane and perpendicular to the elastic axis during deformations. The effects of shear deformation are neglected.

12. The blade undergoes moderate deflections, implying small strains and finite rotations.

13. Structural damping forces are viscous.

14. The effects of dynamic stall are not included. Quasi-steady stall and compressibility effects are modeled through tables of lift, drag and moment coefficients. The unsteady aerodynamic effects, including circulatory effects and the acceleration type non-circulatory effects, are neglected with the exception of pitch damping.

15. Aerodynamic forces and moments on the blade section are based on the airflow velocity at the elastic axis of the blade.

16. All blades are assumed to have identical mass, stiffness, and geometric properties.

17. The blades rotate at a constant angular speed, Ω. Engine and engine control system dynamics are neglected.

18. The blade pitch control system, including the actuators, is infinitely stiff. Freeplay in the control linkages is not modeled. The swashplate and tail rotor collective control are attached rigidly to the pilot controls.

2.2.3 Main Rotor Equations of Motion

The dynamics of the main rotor blades are treated individually in the rotating frame where equations for each blade are formulated independently, rather than

considering the dynamics of the rotor system as a whole and formulating the equations in the non-rotating frame. This modeling of the individual blades by separate (although coupled) equations allows for analysis of system with dissimilar blades. For the case of the present study, the blades are all assumed to be identical and follow the same track.

The main rotor blades are modeled as flexible beams undergoing coupled flap, lag, torsion, and axial motion. They are attached to a hub that may have large amplitude linear and angular motions. The blade equations of motion are nonlinear coupled, partial differential equations with periodic coefficients. These equations are transformed into a system of nonlinear, coupled, *ordinary* differential equations using a finite element discretization to eliminate the spatial variable. The discretization is based on Galerkin's method of weighted residuals. The resulting beam finite element has 15 modal degrees-of-freedom, namely: flag and lag bending displacement and slopes at the ends of the element, for a total of 8 degrees-of-freedom; torsional rotations at the ends of the element and at the element mid-point; and axial displacements at four equally spaced nodes within the element, including the two end points. The aerodynamic, structural, tensile, and inertial load vectors are calculated numerically, using Gaussian integration.

A modal coordinate transformation is used to reduce the number of degrees-of-freedom, and consequently, the number of equations that describe the dynamics of each rotor blade. Coupled, rotating blade mode shapes are used in the transformation. The result is a system of nonlinear, coupled, second-order ordinary differential equations with time-varying coefficients, that is converted to first-order form and

coupled to the remainder of the mathematical model.

2.2.4 Fuselage Equations of Motion

The main assumption in the formulation of the fuselage equations of motion is that the body of the helicopter is rigid. The fuselage equations consist of the non-linear force and moment equilibrium equations and the equations that relate the aircraft angular rates p, q, and r and the rates of change of the Euler angles ϕ_F, θ_F, and ψ_F, respectively.

External loads are applied at the center of gravity of the body, and include contributions from the main and tail rotors as well as aerodynamic loads applied directly to the fuselage. The loads from the main rotor are of inertial and aerodynamic origin. Aerodynamic forces and moments acting on the body of the fuselage are extracted from non-linear data tables of aerodynamic coefficients.

2.3 Rotor Flow Field Modeling

In the present work, the aerodynamic flow field of the rotor was modeled using a time-accurate Free Vortex Method (FVM) [29]. Ground effect was modeled using an image rotor system. An inviscid-viscous method was utilized to predict the flow field arising from a combination of the rotor flow (modeled as an inviscid potential flow by the FVM) and the resulting viscous flow in the boundary layer at the ground [2].

2.3.1 Computing Induced Velocities Using the Biot-Savart Law

In a FVM, the velocity induced by the wake at any location may be computed by the repeated application of the Biot-Savart Law, and then numerically integrating the induced velocity contribution from each vortex element over the entire flow field. Figure 2.1 shows a schematic of how the application of the Biot-Savart law may be used to compute the velocity $\mathbf{V}$ at a point 'P' from a curved vortex filament of strength Γ. This velocity is given in analytical form by

$$\mathbf{V} = \int \frac{\Gamma}{4\pi} \frac{d\mathbf{l} \times \mathbf{r}}{|\mathbf{r}|^3} \tag{2.5}$$

where $\mathbf{r}$ is the position vector of the point 'P' with respect to the vortex element $d\mathbf{l}$. In the present work, the curved vortex filaments were approximated by straight-line segments, resulting in a reconstruction of the induced velocity field that is second-order accurate [32].

2.3.2 Blade Aerodynamic Model

The main rotor was modeled as N_b rigid, articulated blades, which execute fully independent, time-accurate, flapping motion. In the present work, each blade was modeled as a distribution of vortex singularities (bound vortices) in the flow field using the Weissinger-L lifting surface model [33]; see Fig. 2.2. Each blade was discretized into N_s spanwise segments and one chordwise segment.

Generally, the wake from each rotor blade consists of a vortex sheet and a concentrated tip vortex. The vortex sheet includes vorticity with components normal

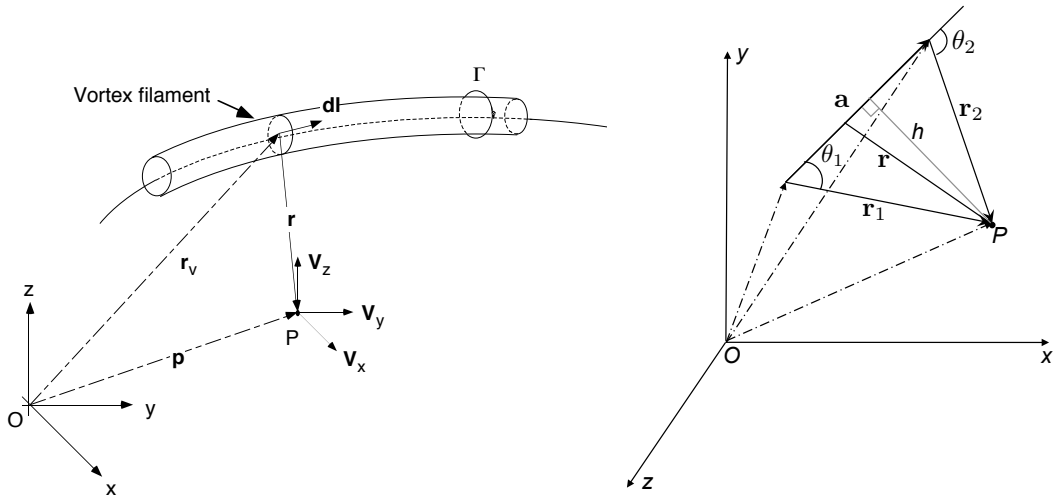

Figure 2.1: Velocity induced at a point 'P' from (a) a curved vortex filament and (b) a straight vortex segment of constant strength [3].

and parallel to the trailing edge of the blade, which are known as trailed and shed vortices, respectively. In the present work, the trailed vortices (i.e., the near wake), was assumed to be rigid and fixed to the blade. The near wake was truncated at $\Delta\psi = 30°$, and was coupled by means of a circulation-preserving boundary condition to a far wake consisting of a rolled-up tip vortex farther downstream.

2.3.3 Free-Vortex Wake Modeling

The vortices of the far wake, which consist of Lagrangian markers that define the straight-line segment approximations to the curved vortex filaments (see Fig. 2.3), were free to convect to force-free locations under the influence of the local velocity field. The motion of the Lagrangian markers is governed by the three-dimensional, incompressible Navier-Stokes equations, which can be written in the

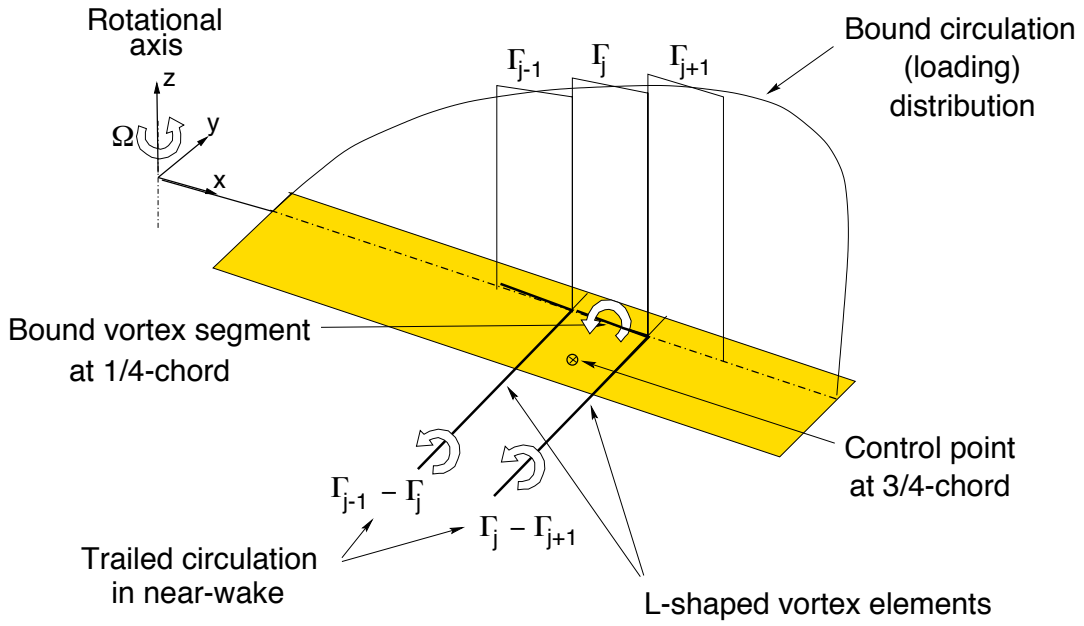

Figure 2.2: Schematic of the Weissinger-L model used to represent the blade [34].

form of the vorticity transport equation, i.e.,

$$\frac{D}{Dt}(\vec{\omega}) = \left(\vec{\omega} \cdot \vec{\nabla}\right) \vec{V} + \nu \Delta \cdot \vec{\omega} \tag{2.6}$$

This equation determines the rate of change of vorticity of a fluid element in terms of the instantaneous values of vorticity $\vec{\omega}$ and the velocity $\vec{V}$. The left-hand side of Eq. 2.6 is the total derivative of vorticity, and includes both the time rate-of-change of vorticity and its convection rate. The first term on the right-hand side of Eq. 2.6 accounts for changes in the length of a vortex filament (the "straining" of the vortex filament) as it is convected in the flow field. The second term on the right-hand side of Eq. 2.6 accounts for the diffusion of vorticity under the action of the turbulence and viscosity of the fluid.

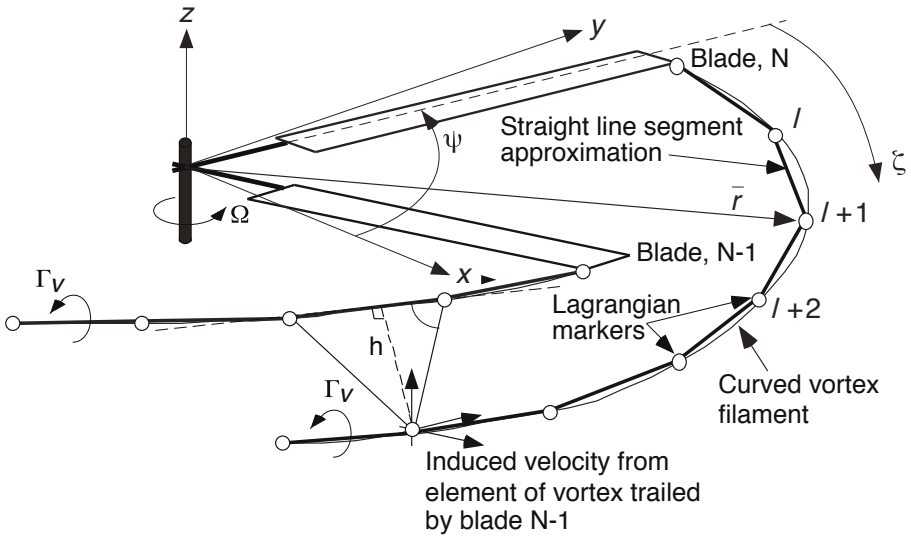

Figure 2.3: Schematic showing the Lagrangian markers used to represent the rotor wake [35].

The straight line segment approximation of the curved vortex filaments mean that all the vorticity is concentrated along the axis of each vortex filament, forming a vortex line singularity. Under inviscid, incompressible, irrotational flow conditions, the vortex lines move as material lines at the local flow velocities. Thus, Eq. 2.6 may be reduced to an advection (wave) equation of the form

$$\frac{d}{dt}(\mathbf{r}) = \mathbf{V}(\mathbf{r}) \tag{2.7}$$

where $\mathbf{r}$ is the position vector of the Lagrangian markers in the vortical wake.

For a rotor blade that rotates with constant angular velocity, $\mathbf{r}$ may be expressed as a function of the azimuthal position of the blade, Ψ, and the age of the filament, ζ, relative to the blade when it was deposited into the wake. In the

non-rotating, hub-fixed coordinate system, Eq 2.7 may be expressed as

$$\frac{\partial \mathbf{r}}{\partial \Psi} + \frac{\partial \mathbf{r}}{\partial \zeta} = \frac{\mathbf{V}}{\Omega} \tag{2.8}$$

where the velocity, $\mathbf{V}$, includes contributions from free-stream effects, induced effects, and additional velocities imposed during the maneuver. This equation is solved using finite difference approximations. The time-accurate, two-step backward, predictor-corrector scheme (PC2B) developed by Bhagwat and Leishman [36] was used in the present work.

2.3.4 Modeling Ground-Effect Using the Method of Images

Ground-effect was modeled using the method of images. An image approach method has been used exclusively in the present work because of its better computational efficiency compared to more complicate models, however this process is less applicable to modeling non-planar or otherwise irregular ground surfaces.

The method of images involves the concurrent simulation of two rotors: a "real" rotor system and an "image" rotor system; see Fig. 2.4. The image rotor system is located at the same lateral and longitudinal positions as the real rotor system, though beneath the ground plane at a negative height of equal magnitude to the height of the real system. The strength of the vortex filaments of the two rotor systems are equal and opposite to each other such that the total normal component of velocity at the ground plane becomes zero when the Lagrangian markers of the real rotor are convected under the influence of both rotor systems. This method,

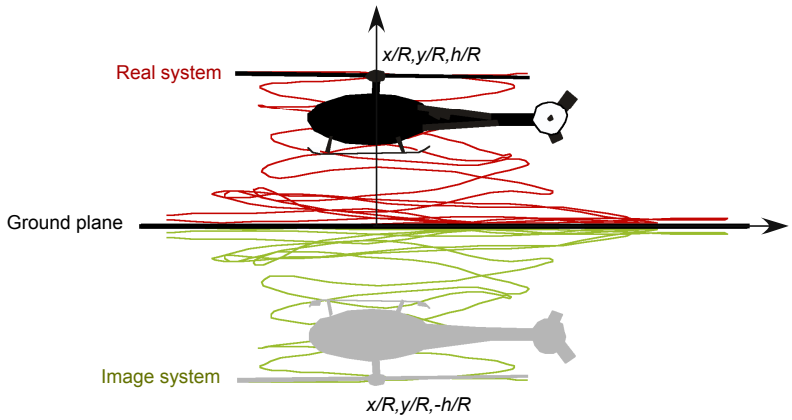

Figure 2.4: A representative free-vortex wake solution obtained using the "method of images" for a rotor in ground-effect [10].

therefore, implicitly satisfies the no-penetration condition at all points over the ground plane.

2.4 Coupling of the Flight Dynamics and the Free Wake

The coupling of the flight dynamics and FVM model allows for the rotor inflow to be calculated by the FVM model, therefore, replacing the need for a dynamic inflow model. Hence, when using the FVM model, the main rotor inflow coefficients and the dynamic inflow equations corresponding to the main rotor are no longer in the trim unknowns or trim equations respectively. The coupling of the flight dynamics and free-wake models precedes as developed in Ref. [28]. The details are summarized here. In addition, the trim process was modified from the trim presented in [28] to create a more computationally efficient and higher fidelity trim, which is explained later in this section.

When passing variables between the models they must be formulated in the

proper discretizations for their respective models. In the flight dynamics model, the azimuth and blade segments are both discretized into 32 Guassian points that are not necessarily evenly spaced. The azimuth and blade segments in the FVM model are discretized into 32 evenly spaced points. When variables are passed to the FVM model, they are linearly interpolated along both the azimuth and the blade to the required evenly spaced points. Before the variables are passed back to the flight dynamics model they are linearly interpolated along the blade segment, then quadratically interpolated along the azimuth back into the Guassian points [28].

2.4.1 Velocity Requirement

As discussed earlier, the total velocity at each blade section is required for the calculation of the bound circulation with the Weissinger-L model [28], i.e.:

$$\sum_{j=1}^{N_s}[I_{b_{i,j}} + I_{NW_{i,j}}]\Gamma_j = \{(\mathbf{V}_\infty + \mathbf{V}_{BM} + \mathbf{V}_{man} + \mathbf{V}_{FW}) \cdot \mathbf{n}\}\, i \tag{2.9}$$

where $I_{b_{i,j}}$ and $I_{NW_{i,j}}$ are the bound and near wake influence coefficient matrices, respectively, and Γ_j is the bound circulation at the blade segment j. The free-stream velocities at the control point,$\mathbf{V}_\infty$, the velocity from the blade motion and flexibility $\mathbf{V}_{BM}$, and the velocities due to the rotation of the helicopter during the maneuver $\mathbf{V}_{man}$ are all provided by the flight dynamics model. The flow velocity V_{FW} is calculated by the FVM.

The free-stream velocity, $\mathbf{V}_\infty$, consists of the hub linear velocities, while the maneuver velocity, $\mathbf{V}_{man}$, consists of the hub angular velocities [28]. Both of these

velocities must be in the global wake coordinate system to be compatible with the FVM model. The velocity from blade motion and blade elastic deformations, $\mathbf{V}_{BM}$ is given by:

$$\frac{d\mathbf{R}_B}{dt} = \frac{\partial \mathbf{R}_B}{\partial t} + \omega \times \mathbf{R}_B \tag{2.10}$$

where $\mathbf{R}_B$ is the position vector of a point on the blade. However, the Weissinger-L model requires the velocities to be at the 3/4 chord location, as opposed to the elastic axis (located in the quarter-chord location) where it is located in the flight dynamics model for the aerodynamic load calculation. To account for this effect, the velocities are computed as in 2.10, but using an adapted position vector:

$$\mathbf{R}_B = e\mathbf{i} + (x_0 + u)\hat{\mathbf{e}}_x + v\hat{\mathbf{e}}_y + w\hat{\mathbf{e}}_z + \underline{y_0\hat{\mathbf{e}}'_y + z_0\hat{\mathbf{e}}'_z} \tag{2.11}$$

which is the position vector of a point that is not necessarily on the elastic axis. The underlined terms in Eq. 2.11 represent the distance of the point from the elastic axis, hence allowing the velocities to be calculated at the 3/4 chord locations on the blades.

2.4.2 Blade Flapping Requirement

The blade flapping angles, $\beta(\psi)$, are necessary to determine the relative positions of the blade control points with respect to the wake filaments in the flow. The flapping angles are also required to determine the release point of the vortex filament at the blade tip. In the uncoupled version of the FVM model used in the

flight dynamics in [2], the blade flapping is prescribed by the blade flapping equation of motion. However, when coupling the FVM and flight dynamics models, the flapping is now a product of the flight dynamics model.

In the flight dynamics model, the blades are flexible and have hinges that can be offset from the axis of rotation. However, the FVM model assumes the blades to be straight, with a flap hinge at the axis of rotation. For this reason, an "equivalent" blade flap angle is defined [28]. Figure 2.5 shows the definition of the "equivalent" flap angle β, which represents the angle between the hub plane and a straight blade hinged at the axis of rotation that has the same tip flap displacement as the elastic blade. The "equivalent" blade flapping angle is given by:

$$\beta(\psi) = \frac{w_{tip}(\psi)}{R} + \beta_p \tag{2.12}$$

where w_{tip} is the flapping displacement of the elastic blade from the undeformed, preconed blade coordinate system, and β_p is the blade precone angle.

While only a rigid flapping angle is given to the FVM model, the effects of blade flexibility are included through the velocity induced by blade motion. The motion of blade from flexibility affects the sectional velocity at each blade control point [35], [34]. The sectional velocity corresponds to $\mathbf{V}_{BM}$ (described in the above section), which is required for the calculation of the bound circulation. Therefore, the velocity from blade motion used for the calculation of the bound circulation accounts for the effects from blade flexibility.

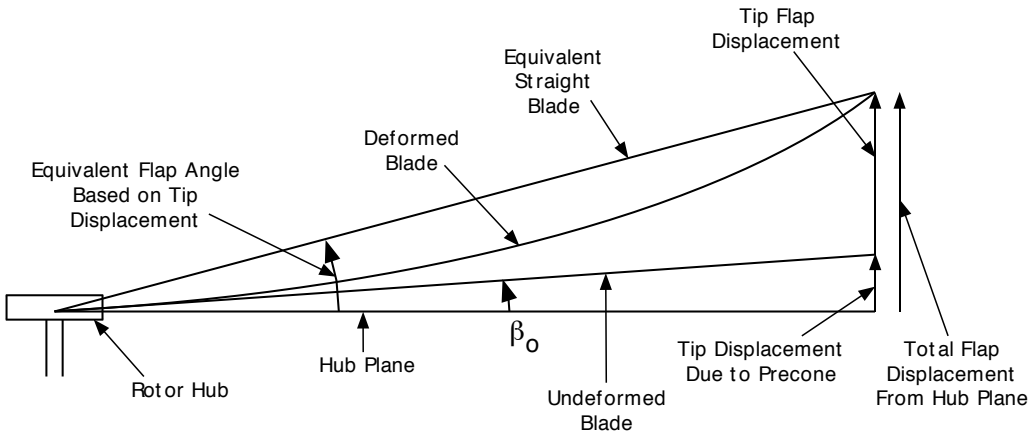

Figure 2.5: Definition of equivalent tip flapping angles for the FVM model [28].

2.4.3 Inflow Exchange

The FVM model outputs the distribution of the induced velocities over the rotor plane, $\lambda(\psi, r)$. The flight dynamics model currently only makes use of the z-component of these induced velocities even though the FVM model calculates the velocity all three directions. This assumption can be made safely for the majority of flight conditions, because the x and y components are much smaller than the z component, hence the inflow can be assumed to be one-dimensional. These velocities are then added to the velocity of the blade section, to obtain the local velocities required to compute the rotor aerodynamic loads [28].

2.4.4 Trim Procedure

Both the flight dynamics and FVM models have separate trim routines when they are decoupled from each other. The goal of the next section is to present a quick

summary of each trim routine, then the coupled version used in the present work. The FVM model has a simplified trim routine that trims to a prescribed rotor thrust, whereas the flight dynamics model has a more extensive model described below.

2.4.4.1 Trim with the FVM Model

The trim procedure used in [2] consists of a simplified trim methodology to calculate the flight control input angles required to obtain the prescribed flight condition. Only the effects of an isolated main rotor system were considered, where the main rotor control inputs are the unknown trim states:

$$\mathbf{x}_{FVM} = \{\theta_0,\ \theta_{1c},\ \theta_{1s}\}^T \tag{2.13}$$

where θ_0 is the collective pitch angle, θ_{1c} is the lateral cyclic angle, and θ_{1s} is the longitudinal cyclic angle. The control vector $\mathbf{x}_{FVM}$ is updated during the trim procedure by solving a linearized system of coupled equations that relate the control inputs, $\mathbf{x}_{FVM}$, to an output vector, $\mathbf{y}_{FVM}$:

$$\mathbf{y}_{FVM} = \{C_T,\ \beta_{1c},\ \beta_{1s}\}^T \tag{2.14}$$

where C_T is the rotor coefficient of thrust, β_{1c} is the lateral flap angle, and β_{1s} is the longitudinal flap angle. The trim routine attempts to minimize the vector:

$$\left\{ \begin{array}{c} C_T - C_{T_{req}} \\ \beta_{1c} \\ \beta_{1s} \end{array} \right\} \rightarrow 0 \tag{2.15}$$

where $C_{T_{req}}$ is the target total thrust coefficient of the rotor system. In this way, throughout a prescribed flight condition, the routine trims to a constant prescribed thrust target as well as zero net flapping with respect to the shaft. The assumptions of using a specific target thrust coefficient and zero flapping are removed when trimming with the coupled flight dynamics and FVM models. Taking these assumptions out provides a more robust trim routine that is trimmed to the full rotorcraft and not just the main rotor.

2.4.4.2 The Base Flight Dynamics Model Trim

The generic trim condition in the flight dynamics model is defined by the total aircraft velocity V, turn rate $\dot{\psi}$, and flight path angle γ. The trim equations make up a system of non-linear algebraic equations, which can be written as:

$$\mathbf{F}(\mathbf{X}) = \mathbf{0} \tag{2.16}$$

The vector of trim unknowns is composed of three parts:

$$\mathbf{X} = \{\mathbf{X}_B \; \mathbf{X}_R \; \mathbf{X}_I\}^T \tag{2.17}$$

where $\mathbf{X}_B$, $\mathbf{X}_R$, and $\mathbf{X}_I$ contain, respectively, the trim unknowns associated with the body, rotor, and inflow. When the FVM model is used to compute the induced velocities, the inflow unknowns are unnecessary and so they are removed from the set of trim unknowns. The body trim unknowns, $\mathbf{X}_B$ are:

$$\mathbf{X}_B = [\delta_0 \;\; \delta_{1c} \;\; \delta_{1s} \;\; \delta_t \;\; \alpha_F \;\; \beta_F \;\; \phi_F \;\; \theta_F \;\; \lambda_t]^T \tag{2.18}$$

where δ_0, δ_{1c}, δ_{1s}, and δ_t are the collective, cyclic, and tail pilot stick inputs respectively; α_F, β_F, ϕ_F, and θ_F are angle of attack, sideslip, pitch angle, and bank angle of the fuselage; and λ_t is the constant tail rotor inflow. The tail rotor inflow is present both when dynamic inflow and the FVM models are used, hence it is included as part of the body trim unknowns.

The corresponding body trim equations consist of the following:

1. *Force and moment equilibrium:* Force and moment equilibrium is enforced by requiring that the linear and angular accelerations of the aircraft be equal to zero when averaged over one rotor revolution:

$$\int_0^{2\pi} \dot{u} \; d\psi = 0 \tag{2.19}$$

and similarly for $\dot{v}$, $\dot{w}$, $\dot{p}$, $\dot{q}$, and $\dot{r}$.

2. *Turn coordination equation:* The condition for turn coordination is that the Y force component be zero when averaged over one revolution [25]:

$$\int_0^{2\pi} [\sin\phi - \frac{\dot{\psi}V}{g}(\cos\alpha\cos\phi + \sin\alpha\tan\theta)\cos\beta]d\psi = 0 \tag{2.20}$$

3. *Relationship between angle of attack and Euler pitch angle:* The flight path angle γ, angle of attack α, sideslip angle β, roll angle ϕ, and pitch angle θ need to satisfy the following equation (Ref. [29]):

$$\int_0^{2\pi} [\cos\alpha\cos\beta\sin\theta - (\sin\beta\sin\phi + \sin\alpha\cos\beta\cos\phi)\cos\theta - \sin\gamma]d\psi = 0 \tag{2.21}$$

4. *Tail rotor inflow:* The tail rotor equation enforces that the tail rotor inflow be constant, on average, over one rotor revolution:

$$\int_0^{2\pi} \dot{u}\, d\psi = 0 \tag{2.22}$$

The blade motion, to convert the differential blade equations into algebraic equations is assumed to be periodic around the azimuth. Each blade has a constant component of motion around the azimuth, as well as three harmonics. The trimmed modal equations have the form:

$$\mathbf{q} = \mathbf{q}_0 + \sum_{i=1}^{N_h} (\mathbf{q}_{ic}\cos i\psi + \mathbf{q}_{1s}\sin i\psi) \tag{2.23}$$

where N_h is the number of harmonics used. Equation 2.23 can easily be differentiated twice to produce the needed modal velocities and accelerations. The corresponding rotor unknowns for the trim algebraic solution are the steady state and harmonic coefficients. In the present work, $N_h = 3$ harmonics are used, so a total of 7 unknowns exist for each blade mode. Assuming that the blades are identical, and perform identical motions in trim, only one blade needs to be taken into account.

The blade equation of motion is transformed from an ordinary differential equation into a set of non-linear algebraic equations using the Galerkin method of residuals. A nonzero vector of residuals $\boldsymbol{\epsilon}$ dependent on the azimuth ψ is created from the deflections $\mathbf{q}$ from Eq. 2.23. The Galerkin method states that the choice of q_0, q_{ic}, and q_{1s} that minimizes on average the residual vector $\boldsymbol{\epsilon}$ is the one which satisfies the following equations [37], i.e.,

$$\begin{aligned} \int_0^{2\pi} \boldsymbol{\epsilon}(\psi)\, d\psi &= 0 \\ \int_0^{2\pi} \boldsymbol{\epsilon}(\psi) \cos j\psi\, d\psi &= 0 \quad j = 1, ..., N_h \\ \int_0^{2\pi} \boldsymbol{\epsilon}(\psi) \sin j\psi\, d\psi &= 0 \quad j = 1, ..., N_h \end{aligned} \tag{2.24}$$

The trim equations are in the form:

$$\mathbf{F}(\mathbf{x}) = \mathbf{0} \tag{2.25}$$

but in general it is not equal to zero but rather a residual that is dependent on blade

azimuth position ψ. This then puts the trim equations in the form:

$$\mathbf{F}(\mathbf{x}) = \mathbf{r} \tag{2.26}$$

where $\mathbf{r}$ is the vector of the residuals obtained by substituting the tentative trim solution $\mathbf{x}$ into the system of equations $\mathbf{F}$. The non-linear algebraic equation solver [38] then adjusts the values of $\mathbf{x}$ to reduce the norm of $\mathbf{r}$ below a certain tolerance and therefore, solve the trim problems.

2.4.4.3 Coupling of the FVM and Flight Dynamics Models in Trim

The trim structure used in [28] places the FVM model in the main trim loop. The FVM model is run to calculate the inflow for each new guess, $\mathbf{X}_K$ of the non-linear algebraic equation solver, as demonstrated schematically in Fig. 2.6. However, the last guesses of the equation solver have very small perturbations from the previous guess and therefore the FVM model is almost insensitive to these small changes of the trim variables. The extra trim guesses leads to a computationally costly simulation with little benefit with a computation time of six to seven hours to trim for a single flight condition. The trim structure was modified to reduce its computational cost, as well as its run time.

The new trim structure proceeds with an inner loop, outer loop structure as demonstrated in Fig. 2.7. The inner loop consists of the basic trim routine as shown in Fig. 2.7(a) and summarized below:

1. The process begins with an initial trim guess, $\mathbf{X}_0$, which is given to the the

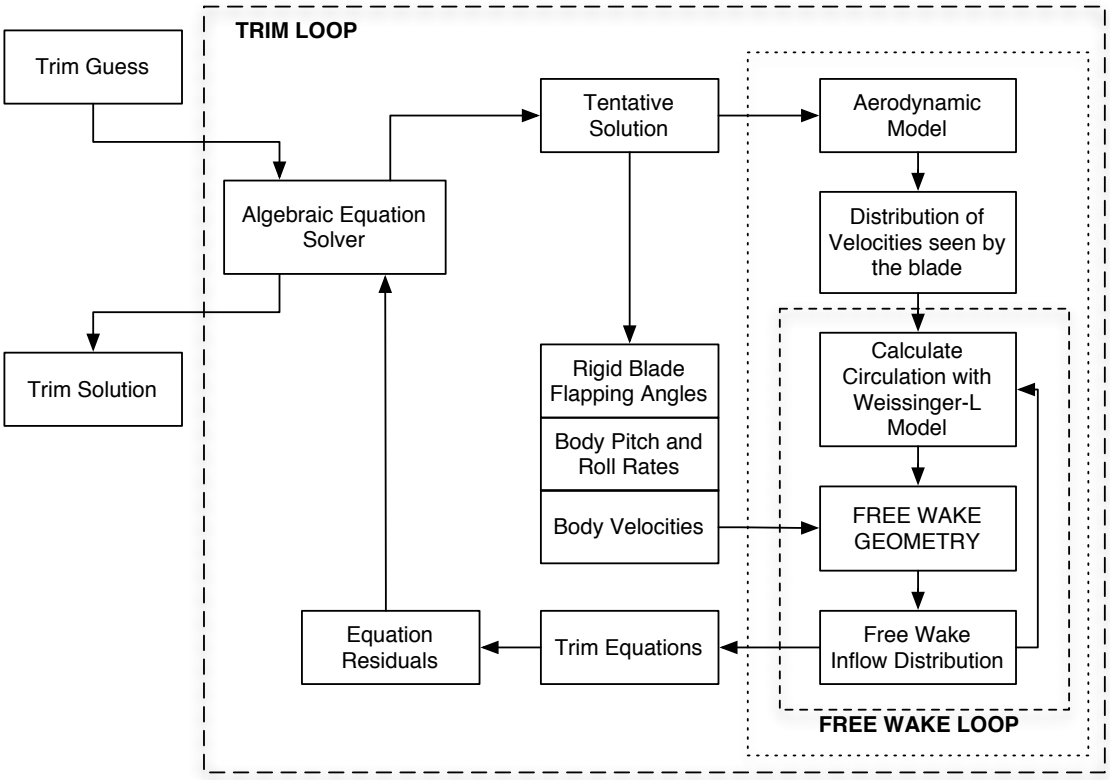

Figure 2.6: Old trim structure [28].

non-linear algebraic equation solver.

2. The algebraic equation solver gives the set of trim variables.

3. The trim variables are transformed from the stick inputs and fuselage angles into the states and their time derivatives using input from the flight condition given. The difference between the trim variables that are used in the algebraic equations and the states used in the ODEs are shown in Table 2.1. The trim variables are also put into the turn coordination, rate of climb of flight path, and tail rotor inflow equations.

4. The states and rates of change are then used to calculate the rotor and fuselage ODEs.

5. Residuals of the ODEs are calculated.

6. Both the ODE residuals and the results of the turn coordination, rate of climb flight path, and tail rotor inflow equations are put in the form of the algebraic trim equations discussed above, and the algebraic equation (AE) residuals are calculated.

7. The residuals are passed to the non-linear algebraic equation solver, and Steps 2 through 7 are repeated until the algebraic equation residuals fall below a certain tolerance and a trim solution is reached.

The outer loop of the new trim structure takes the FVM out of the trim loop as shown in Fig. 2.7(b), and is summarized below:

1. Like in the inner loop, an initial trim guess is given to the system.

2. Initially, the inner loop trim with dynamic inflow and its corresponding states calculates a trim solution based on dynamic inflow.

3. The FVM model uses the trim solution given from the inner loop trim to calculate the velocities seen at the blades and the blade flap angles, as discussed above. The FVM then calculates the induced inflow based on this trim solution, velocities, and flap angles.

4. With the updated induced inflow, the inner trim loop proceeds. In this loop, the dynamic inflow and its corresponding states have been removed, and the updated inflow is used in its place. The inner loop produces an updated set of trim variables.

5. At this point, the current updated trim variables are compared to the trim variables from the previous run of the inner loop to see if the trim variables have converged.

6. Steps 3 through 5 are repeated until the trim variables have converged below a certain tolerance and a trim solution has been reached.

This new method of trim has some advantages over the method used in [28]. The accuracy of the trim solution is increased because of an additional requirement of the trim variable convergence. In the method from [28] the trim solution is reached once the residuals are below a certain tolerance. However, this method has the possibility that a significant change in the trim variables could lead to a result in residuals below the required tolerance even though the trim variables have not converged yet. The added requirement that the trim variables need to be converged ensures that the trim solution is achieved gradually and that the wake geometry and the set of trim variables match.

This trim approach builds on the concept from [28] of fixing the induced velocities during the calculation of trim because the FVM model is insensitive to very small changes to the trim variables. By fixing the induced velocities for the bulk of the trim solution, and trimming with fixed inflow then updating the wake to the new trim solution and repeating the processes, the computational efficiency of the simulation is increased. The modified trim method has computation times around five to ten minutes per flight speed.

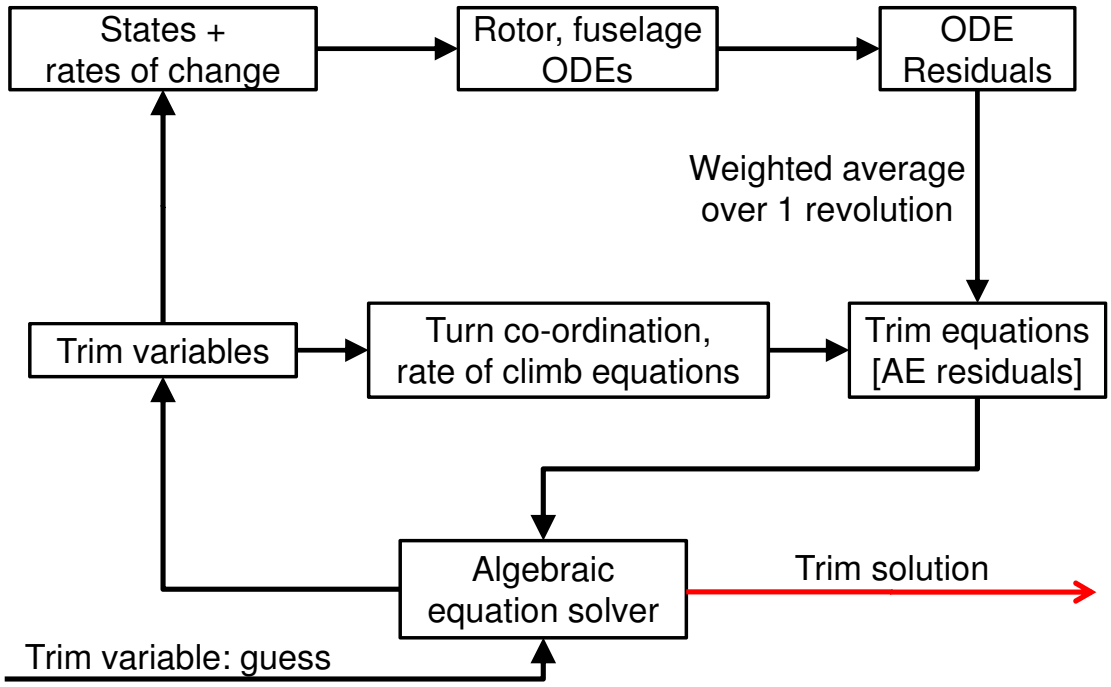

(a) Inner loop trim structure.

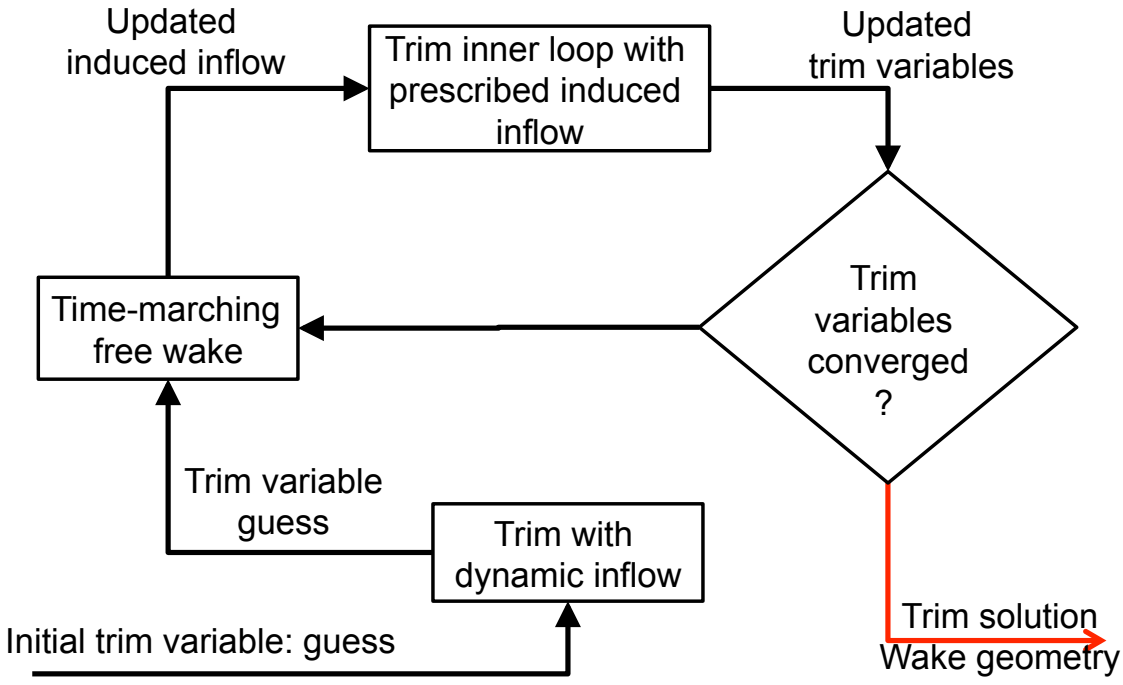

(b) Outer loop structure.

Figure 2.7: Modified trim structure.

2.5 Approach Profile Following in Time Integration

The time-integration of the baseline equations of motion involve the calculation of the dynamic response results for a given set of initial conditions and controls that are applied during the integration, providing a time history for the rotorcraft states based on these given controls. A time history of the free wake response to the given set of controls can also be produced during the time integration. In order to model a specified approach maneuver a method is implemented using inverse simulation to calculate the necessary controls for the rotorcraft to match the profile.

2.5.1 Baseline Integration Procedure

The method of time integration used integrates the full set of non-linear equations with respect to time. The equations of motion are represented in the implicit formulation:

$$\mathbf{f}(\dot{\mathbf{y}}, \mathbf{y}, \mathbf{u}; t) = 0 \tag{2.27}$$

and are integrated numerically using an ordinary differential equation solver. The solver used, DDASSL, is a variable step, variable order Adams-Bashforth method solver in which the derivatives are approximated by a backward-difference formula.

The integration starts from an initial trim solution. From the trimmed state, the non-linear equations of motion are integrated in time for the prescribed duration of the simulation. The result is a set of time-histories of all the states of the model following the pilot-prescribed input controls. When the FVM model is included in the time integration, at each time step the equations of motion are advanced forward

with a fixed induced inflow and then the FVM model is advanced forward one step with the resulting states from the equations of motion fixed.

2.5.2 Integration with the FVM Model

The time-integration with the FVM model proceeds in a similar fashion to the trim. The FVM model can be advanced in time with an arbitrary step size $\delta\psi$, and hence can be coupled with the dynamics model at any desired point in the integration of the equations of motion. When using the time-marching FVM model, it is not necessary to assume that each time the FVM model is evaluated represents a steady-state condition. And because no assumption of periodicity is necessary, the induced velocities do not need to be converged and evaluated for the entire rotor at each call of the wake. At each step the time-marching free wake is advanced only from the previous to the new time [28].

The inputs required for the FVM model during the time integration are the same as those required for trim. In addition to the inputs discussed above, the rotor position in space is given to the FVM model. However, since the integration is only advancing one step at a time, only the new updated values of the flap and the blade velocities at the new azimuth position are required, rather than the values over the entire rotor disk.

2.5.3 Approach Profile Implementation

The brownout simulation requires that the helicopter follow a specified approach profile path. The approach profile is given in terms of the time step and its respective $x,\ y,\ z$ positions and $u,\ v,\ w$ body velocities. The goal of the approach profile implementation is to match the corresponding states from the flight dynamics model to the desired approach.

A stability augmentation control system existed in the flight dynamics model for the time-integration and specified the appropriate pilot stick inputs to keep the helicopter on a steady flight path. The concept of using a controller to specify the stick inputs was expanded to keep the states not only stable but to track a specified path.

The approach profile implementation consists of a controller that is used to find the pilot stick inputs that produce the states required of the prescribed profile. The controller is based on the standard control law:

$$u = Ke = K(r - x_{state}) \tag{2.28}$$

where $\mathbf{u}$ is a vector of the pilot stick inputs, $\mathbf{e}$ is the error between the reference vector containing the specified states r and the actual state vector $\mathbf{x}_{state}$; $\mathbf{K}$ is a matrix with the controller values. The controller is presented schematically in Fig. 2.8.

The input to the controller is the error $\mathbf{e}$ between the reference state $\mathbf{r}$ and the actual state $\mathbf{x}_{state}$. The whole state vector is integrated at each time step, and so full state feedback is assumed. Only the rigid body states are controlled in the present

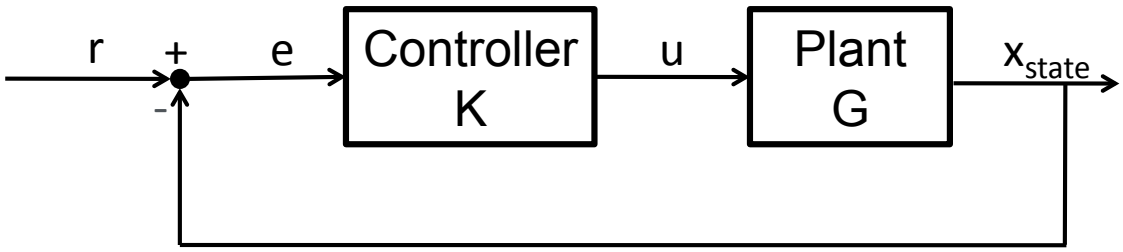

Figure 2.8: Standard control structure

methodology. The states given to the controller are shown below in Eq. 2.29:

$$\mathbf{x}_{state} = \{x\ y\ z\ u\ v\ w\ p\ q\ r\ \phi\ \theta\ \psi\}^T \tag{2.29}$$

and the reference vector consists of the corresponding states. The x, y, and z positions as well as the u and w body velocities for the reference vector are given from the specified approach profile. Because the time-integration proceeds after trim, the rest of the states, the body velocity v and the body rates and angles p, q, r and ϕ, θ, ψ respectively, are given their trim state for the reference vector. The resulting reference vector has the form:

$$r = \{x_{app}\ y_{app}\ z_{app}\ u_{app}\ v_{trim}\ w_{app}\ p_{trim}\ q_{trim}\ r_{trim}\ \phi_{trim}\ \theta_{trim}\ \psi_{trim}\}^T \tag{2.30}$$

The output of the controller is the set of pilot stick inputs required to keep the states on the approach profile:

$$u = \{\delta_0\ \ \delta_{1c}\ \ \delta_{1s}\ \ \delta_t\}^T \tag{2.31}$$

The goal of the controller is to only control the rigid body states. Therefore, the linearized model computed at trim was condensed from its form consisting of all the states to only the rigid body states. The original form of the linearized model can be written as:

$$\begin{Bmatrix} \dot{\mathbf{x}}_B \\ \dot{\mathbf{x}}_R \end{Bmatrix} = \begin{bmatrix} \mathbf{A}_{BB} & \mathbf{A}_{BR} \\ \mathbf{A}_{RB} & \mathbf{A}_{RR} \end{bmatrix} \begin{Bmatrix} \mathbf{x}_B \\ \mathbf{x}_R \end{Bmatrix} + \begin{bmatrix} \mathbf{B}_B \\ \mathbf{B}_R \end{bmatrix} \mathbf{u} \tag{2.32}$$

where the state vector $\mathbf{x}$ has been partitioned into the rigid body states $\mathbf{x}_B$ and the rotor states $\mathbf{x}_R$. The states can be condensed to only the rigid body states by setting $\dot{\mathbf{x}} = \mathbf{0}$ and solving for $\mathbf{x}_R$. The final condensed system can then be written as:

$$\begin{aligned} \dot{\mathbf{x}}_R =& (\mathbf{A}_{BB} - \mathbf{A}_{BR}\mathbf{A}_{RR}^{-1}\mathbf{A}_{RB}) \quad \mathbf{x}_B + (\mathbf{B}_B - \mathbf{A}_{BR}\mathbf{A}_{RR}^{-1}\mathbf{B}_R) \quad \mathbf{u} \\ =& \quad \mathbf{A}_1 \quad \mathbf{x}_B + \quad \mathbf{B}_1 \quad \mathbf{u} \end{aligned} \tag{2.33}$$

where the new system has the 12 rigid body states (including the positions x, y, and z), and 6 degrees of freedom [40]. The controller is then created from this condensed system.

A linear quadratic regulator (LQR) algorithm based on the cost function [39]:

$$J[u] = \int_{t_0}^{t_f} \left\{ \vec{x}^T(t) Q(t) \vec{x}(t) + \vec{u}^T(t) R(t) \vec{u}(t) \right\} dt \tag{2.34}$$

was used for assembling the controller, where Q and R are weighting matrices on

the states and the inputs respectively. The Q matrices were structured so that the weights would be heavier on the body positions and velocities to ensure good tracking. The body angles and angular rates were weighted less heavily so they have the freedom to move as the maneuver required to stay on the proper approach profile while staying close to a nominal value. The body velocity in the y direction v was also held at its trim value, since only profiles in the $x - z$ plane are analyzed here. It is possible that this value could change for approaches to include turns however, the present study focuses on straight approaches only. The R matrix was designed to ensure that the controls stayed within the realistic bounds of the pilot stick inputs. However, the control inputs do not take into account a pilot model, and hence they do not include a delay for human response.

The LQR algorithm was chosen for its robustness and its guarantee of stable poles for the closed loop system. A pole-placement method was originally attempted, but this did not provide the performance or the stability necessary. The LQR method allowed for more specific tuning of each state as opposed to choosing where the various poles would be. Moreover, the LQR algorithm simplified the controller building and well as standardized the process.

The actual controller is assembled from a group of possible controllers based on the flight path angle γ and the total flight velocity V, which are all designed using the LQR method above. The group is broken into three sets of controllers for flight path angles $0°$, $6°$, and $12°$, which correspond to the boundaries for the angle

of descent parameter in the optimization. The angles contained in each set are:

$$\begin{aligned} 0^\circ \text{ set: } & 0^\circ \leq \gamma < 3^\circ \\ 6^\circ \text{ set: } & 3^\circ \leq \gamma < 9^\circ \\ 12^\circ \text{ set: } & 9^\circ \leq \gamma \leq 12^\circ \end{aligned} \tag{2.35}$$

Each flight path angle set consists of controllers built from the linearized models computed at trim for every 5 kts from 0 kts to 150 kts at the flight path angle for the set it belongs to. In each flight path angle set, the LQR tuning parameters are the same for all speeds for consistency and ease of quickly creating a large set of possible controllers.

The process to assemble the appropriate controller is shown in Fig. 2.9, and summarized below:

1. At the beginning of the time integration, the appropriate set of controllers K_{set} based on the flight path angle γ is chosen. Notice that for the current approach profile the flight path angle is consistent and does not change. Hence, the appropriate set of controllers is loaded only once at the beginning of the time integration.

2. Find the speeds, K_{spd}, that the total flight velocity V lies between. If the velocity is less or more than the respective lower and upper bounds, then the controller used will be the one at the bound.

3. Interpolate each entry of the controller, K, based on the difference of the total

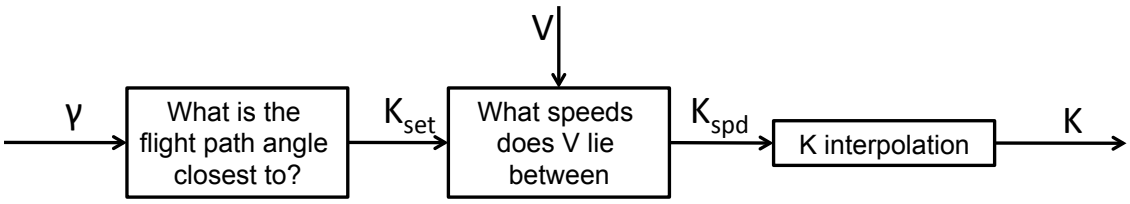

Figure 2.9: Assembling the appropriate controller.

flight velocity and the speeds found above.

While the specific set of controllers corresponding to the flight path angle are only loaded once at the beginning of time integration, the velocity interpolation happens at every time step of the integration. The controller assembly process at each time step assures that the controller is always created for the specific flight condition. Having multiple sets of flight path angles allows the controllers to have different weights depending on the aggressiveness of the angle of descent for a more customizable controller.

The whole time-integration loop proceeds similarly to the trim process. Once the trim process is finished, however, it is possible that the trim states do not match the first step of the approach profile. This outcome can result in an abrupt change in controls, and could destabilize the rotorcraft states. To ensure that this behavior does not occur, the first five rotor revolutions of the time integration are used to linearly move from the trim states to the states required at the first step of the approach profile. The first step of the approach profile is then held for the next ten revolutions to make sure that all transients have been steadied out. Once those first 15 rotor revolutions of the time integration finish, the approach profile proceeds. The

time integration process is summarized below and shown schematically in Fig. 2.10:

1. The simulation begins from the trimmed solution at $\mathbf{t} = 0$.

2. Based on the flight condition, the controller is assembled and the new pilot inputs are calculated.

3. The equations of motion are integrated to time $\mathbf{t} = \mathbf{t} + \boldsymbol{\Delta}\mathbf{t}$ using the DDASSL ODE solver.

4. To calculate the rotor inflow, the blade flap and velocities are saved for the FVM model.

5. The FVM model is marched just one step to the new time $\mathbf{t}$ and the inflow is saved for the next step.

6. If the system has taken the required number of steps, then the simulation is complete, if not steps 2 through 4 are repeated.

2.6 Dust Cloud Modeling

Once the rotor flow has been predicted, the resulting brownout cloud may be modeled. Notice that a one-way coupling is assumed in the present work, meaning that the particle motion is driven by the air but not vice-versa, i.e. a dilute dust cloud assumption. The brownout cloud modeling problem is particularly complicated, in that the model must be capable of modeling several modes of particle uplift and entrainment. Furthermore, the model must contain a sufficient number of dust

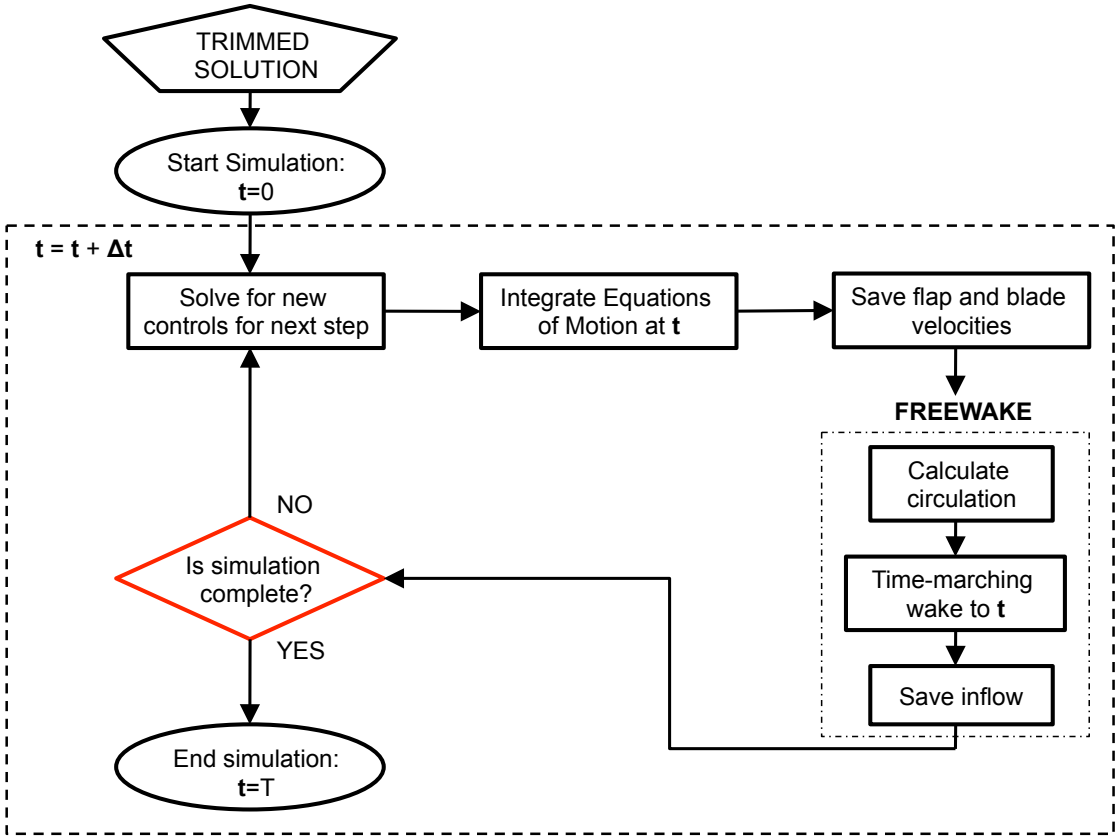

Figure 2.10: Time integration procedure.

particles to represent the essential features and characteristics of the brownout cloud, but not so many particles as to prohibitively increase the computational expense of the calculations [2].

2.6.1 Mobilization of Sediment from the Bed

Accurately modeling the conditions by which individual dust particles become mobilized under the action of an unsteady, turbulent, vorticity-laden rotor flow field is essential for modeling the development of a brownout cloud. Although most prior entrainment models have been based upon the exceeding of a threshold friction velocity, Syal and Leishman [10] proposed a brownout cloud development model

that includes: (i) direct mobilization by exceeding a threshold velocity and/or (ii) the action of unsteady pressure effects (iii) mobilization by bombardment ejection. This is the model that is used in the present work.

Stationary particles in a sediment bed are subjected to several types of forces, such as shear, which can be resolved into components of lift, drag, pressure, inter-particle forces, and gravitational forces. If the moments created by the aerodynamic forces exceed those from the gravitational and inter-particle forces, the particle can become mobilized. This process is known as direct aerodynamic entrainment. However, when previously mobilizaed or uplifted particles impact the sediment, other smaller particles can be ejected through the process of bombardment. While previous models did not include this effect into, the model used in the present study takes into account bombardment ejection [3].

2.6.2 Particle Convection

Once a particle has been entrained into the flow field, a variety of forces govern the particle's motion. A one-way coupling has been assumed in the present work, meaning that the particle motion is driven by the air ,but not vice-versa. Althougth this assumption is not valid in all regions of the flow (particularly in regions that are closest to the ground), it is an assumption that makes an overall solution of the problem much more computationally tractable.

2.6.3 Numerical Implementation

A variety of simplifications must be adopted for the numerical modeling of large-scale brownout clouds. In the present work, the sediment bed was assumed to consist of monodisperse spherical particles that were arranged in layers; see Fig. 2.11a. Initially, only the particles in the top-most layer of the sediment are considered to be "active," meaning that they are eligible to be entrained under the action of the aerodynamic forces. As these particles become entrained in the flow by the different mechanisms, the particles directly beneath become active; see Fig 2.11b. Because only a finite number of layers can be computationally modeled, however, a particle only becomes active after a specified time delay, δt, after the particle in the layer just above it has become active.

Once the particles are entrained, they convect in the flow. When the entrained particles bombard the sediment bed with enough kinetic energy to eject particles, the bombarded particles are treated as new (additional) particles that are introduced into the simulation; see Fig. 2.11c.

Computationally, the dust cloud simulation is very costly, and so a variety of methods were use to accelerate the computation times. In the present work, "message passing interface" (MPI) was utilized for parallelization of the processes on multicore central processing units (CPUs) [41], and "compute unified device architecture" (CUDA) was utilized for parallelization on graphical processing units (GPUs) [42]. These methods resulted in close to 25$\times$ speed-up for the cloud simulation.

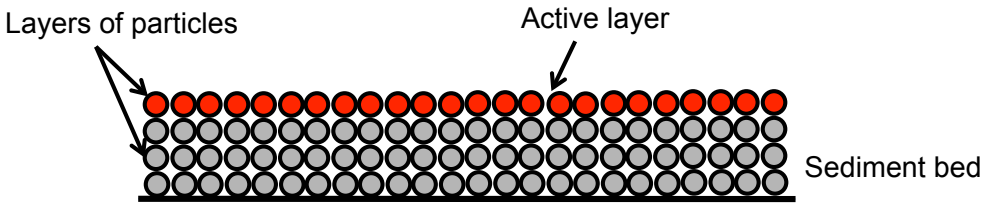

(a)

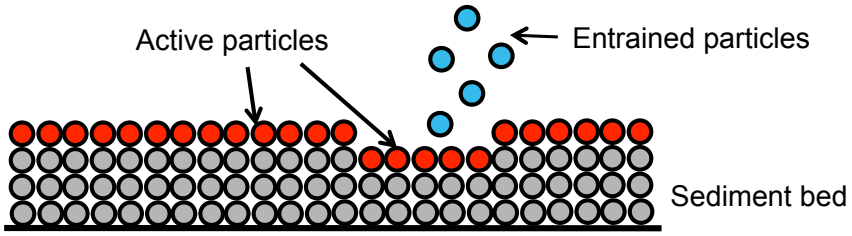

(b)

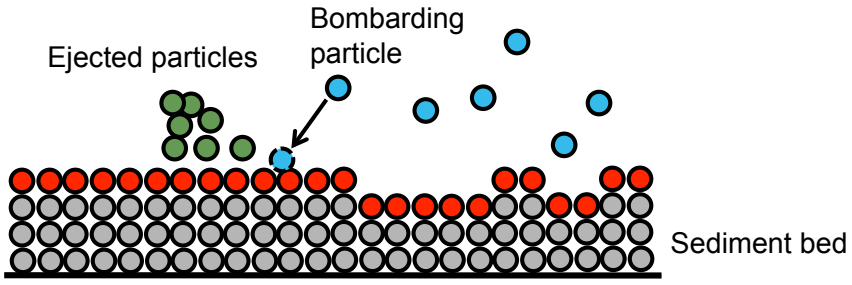

(c)

Figure 2.11: Schematic of (a) the stationary sediment bed structured in the form of layers, (b) active and entrained particles, and (c) new particles ejected through bombardment [3].

2.7 Optimization Methodology

As noted earlier, the brownout mitigation is formulated mathematically as a numerical optimization problem and cast into a nonlinear mathematical programming form. Therefore, the procedure consists of finding the value of a vector of design variables, $\mathbf{X}$, such that a scalar objective function, $B(\mathbf{X})$, is minimized, i.e.,

$$B(\mathbf{X}) \rightarrow \min \tag{2.36}$$

subject to:

behavior constraints
$$g_j(\mathbf{X}) \leq 0 \quad j = 1, ..., m \tag{2.37}$$

side constraints
$$\mathbf{X}_{min} \leq \mathbf{X} \leq \mathbf{X}_{max} \tag{2.38}$$

2.7.1 Design Vector, X

The design vector, $\mathbf{X}$, consists of three variables that describe a nominal approach profile: (i) the approach angle, α_{app}, (ii) the initial (asymptotic) velocity, v_0, and (iii) the range at which peak deceleration occurs, r_{pd} (i.e., how late into the maneuver the pilot waits to decelerate) such that

$$\mathbf{X} = \begin{Bmatrix} x_1 \\ x_2 \\ x_3 \end{Bmatrix} = \begin{Bmatrix} \alpha_{app} \\ v_0 \\ r_{pd} \end{Bmatrix} \tag{2.39}$$

These parameters can be used to generate the longitudinal deceleration and velocity, and vertical velocity profiles for a general approach maneuver applying the formulation in [43] and [2]. Representative longitudinal deceleration and velocity profiles are shown in Fig. 2.12, respectively. For the current study the same formulation used in [2] is applied here, and for consistency the same baseline condition is used. The baseline parameters used are $\mathbf{X}_1 = [\alpha_{app}\, v_0\, r_{\mathrm{pd}}]^T = [6^\circ\ 90\ \text{kts}\ 300\text{ft}]^T$.

Each design variable is subjected to side constraints, i.e. Eq.2.38. The side constraints for the present study are the same side constraints used in Ref [2] for consistency, and they are

$$1^\circ \leq \alpha_{app} \leq 12^\circ \tag{2.40}$$

$$60\ \text{kts}\ \leq v_0 \leq 120\ \text{kts} \tag{2.41}$$

$$100\ \text{ft}\ \leq r_{pd} \leq 500\ \text{ft} \tag{2.42}$$

2.7.2 Objective Function, $B(\mathbf{X})$

To evaluate the effects of the different operational strategies, a quantitative measure of brownout severity is required. The objective function formulation used in [2] has been used for the present study. This objective function is characterized by the aggragate of particle density in the FOV, which is taken to be a surrogate for the visual degradation experienced by the pilot in brownout conditions.

From a practical standpoint, the objective function, $B(\mathbf{X})$, represents the cloud density in the best region of the FOV that the pilot could potentially use to perceive

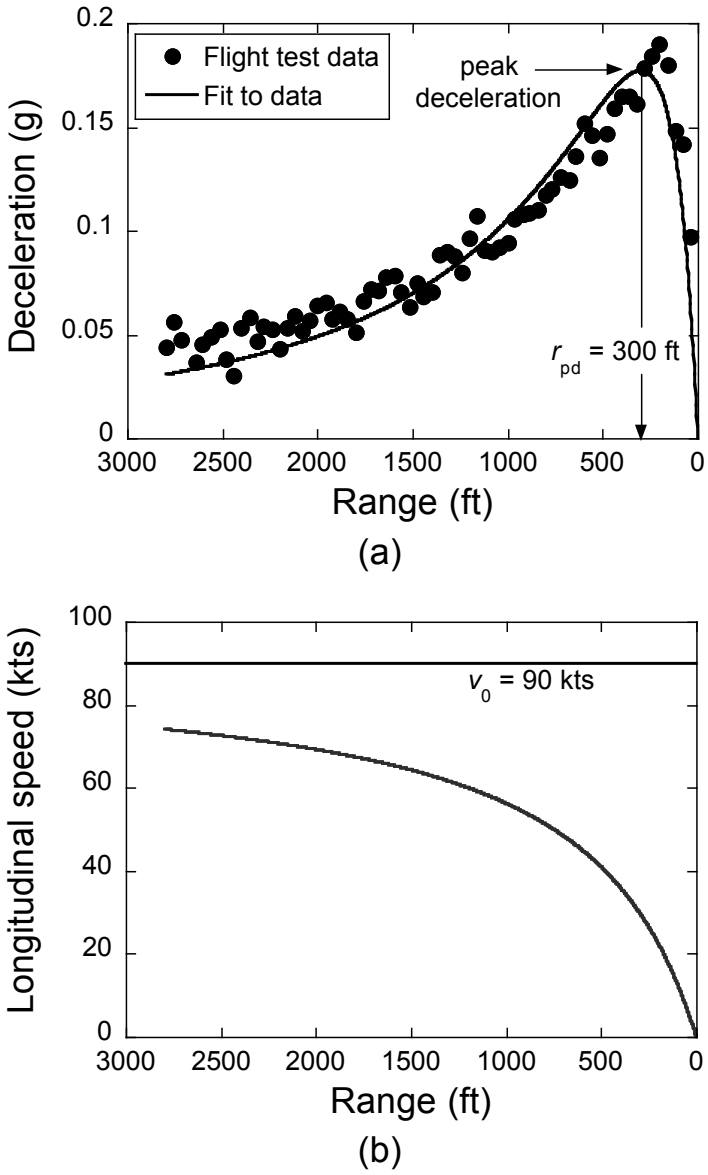

Figure 2.12: Longitudinal (a) deceleration and (b) velocity profiles for a representative approach (from Ref. j diss)

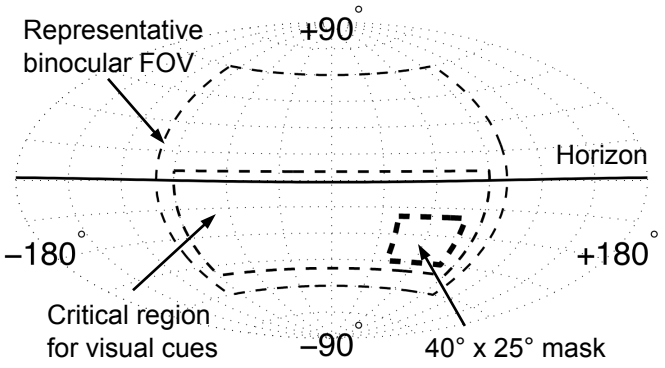

Figure 2.13: Representation of the most important regions of a pilot's field of view for calculation of the objective function [2].

visual cues. The calculation of the objective function begins by projecting the position of each particle of the cloud, at each instant in time, onto a sphere, centered at the pilot's head. The particles of the simulated brownout cloud are projected in the pilot's FOV via a series of coordinate transformations.

The pilot does not require clear visual paths in all directions during a landing maneuver. Alternately, the pilot can safely land a helicopter with a relatively small FOV, provided it is oriented towards a region that provides sufficient cueing. The regions of a pilot's FOV that are most critical during a landing maneuver are depicted in Fig. 2.13. A 200° by 120° region to the front of the aircraft is typical of a pilot's binocular FOV [44]. Within that FOV, a 180° by 55° subregion was identified as being representative of the portion of the pilot's FOV where essential visual cues are found, specifically the regions in the pilot's near-field (labeled the "critical region for visual cues" in Fig. 2.13). In the presence of sufficient microtexture cues, i.e., fine-grained detail in the visual scene, a pilot can maintain satisfactory control over the aircraft with a FOV as small as approximately 40° laterally by 25° vertically

[45]; such a region is also shown in Fig. 2.13. Assuming a pilot will scan intuitively to find the regions of his or her FOV that are the least obscured during brownout, the 40° by 25° sector with the lowest particle count may be considered to be the "best" region in which the pilot should focus attention.

At a given instant in time, the number of particles, n_p, in this "best" 40° by 25° sector of the pilot's FOV is given by

$$b(\mathbf{X}, t) = \min \left[\sum_{\phi_p=i}^{i+25^\circ} \sum_{\theta_p=j}^{j+40^\circ} n_p(\phi_p, \theta_p, t) \right] \tag{2.43}$$

$$\text{for: } -50^\circ \leq i \leq -20^\circ \; -90^\circ \leq j \leq 50^\circ$$

where $n_p(\phi_p, \theta_p, t)$ is the number of dust particles in the one-degree solid angle centered at ϕ_p and θ_p at time t, and the values selected for i and j restrict the scan area to the "critical region for visual cues" identified in Fig. 2.13. The brownout objective function, $B(\mathbf{X})$, is then defined as

$$B(\mathbf{X}) = \int_{t_1}^{t_2} b(\mathbf{X}, t) dt \tag{2.44}$$

where t_1 is the starting time and t_2 is the ending time of the maneuver.

It is important to note that this objective function formulation is highly idealized. For example, it does not consider the constraints on the FOV that are imposed by cockpit obstructions of any addition equipment (such as night vision goggles). Additionally, some fundamental human factors are not considered in the present analysis. For example, the movements of the "best" 40° by 25° sector between time

steps in the brownout simulation may be faster than typical eye has the ability to move.

2.7.3 Behavior Constraints, $g_j(\mathbf{X})$

Behavior constraints were applied to the optimization procedure to ensure that the resulting approach profiles were realistic and safe. The behavior constraints applied are the same as those used in [2] for consistency. The first behavior constraint was imposed to limit the maximum approach angle over the duration of the maneuver. In the current study, the maximum pitch angle over the duration of the maneuver was constrained to be no more than 30°, i.e.,

$$g_1(\mathbf{X}) = \theta_{max}(\mathbf{X}) - 30^\circ \leq 0 \tag{2.45}$$

Notice that a 30° pitch attitude would correspond to an aggressive deceleration, much more aggressive than would be typical of a standard approach. However, given the anecdotal reports that a common operational tactic for brownout landings is to "outrun" the cloud and rapidly decelerate just prior to landing, this constraint was purposefully constructed to allow the optimizer to select very aggressive approaches.

A second behavior constraint was imposed to prevent flight conditions that are conducive to the onset of vortex ring state (VRS). Figure 2.14 shows boundaries within which VRS maybe be expected to occur, as identified in [46]. Although the boundaries are only approximate, their explicit definition is essential for the mathematical description of a constraint function. Approach profiles for $\alpha_{app} = 1^\circ$

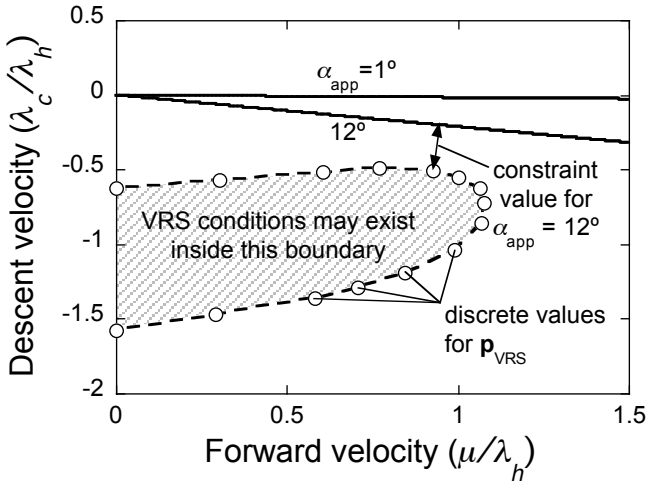

Figure 2.14: Graphical depiction of the behavior constraint for vortex ring state avoidance [2].

and 12° are plotted on the same axes in Fig. 2.14. Notice that the approach profiles are shown to be straight lines when plotted on these axes. The constraint value is simply the distance between the closest points on the approach profile and the VRS boundary, as illustrated for the $\alpha_{app} = 12°$ case in Fig. 2.14 .

While it is possible to express this constraint by utilizing analytical expressions for the approach profile and VRS boundaries, an alternate approach is to express each boundary as a series of discrete points, $\mathbf{p}_{app}(\mathbf{X})$ and $\mathbf{p}_{VRS}$. The discrete points that comprise $\mathbf{p}_{VRS}$ are depicted in Fig. 2.14 for illustrative purposes; however, there are too many points in $\mathbf{p}_{app}(\mathbf{X})$ to be shown clearly. The constraint can be expressed mathematically,

$$g_2(\mathbf{X}) = \epsilon - \mathrm{m}in \left\| \mathbf{p}^i_{app}(\mathbf{X}) - \mathbf{p}^j_{VRS} \right\| \leq 0 \text{ for all } i, j \tag{2.46}$$

where ϵ is a small number (the exact value will depend on how finely $\mathbf{p}_{app}(\mathbf{X})$ and

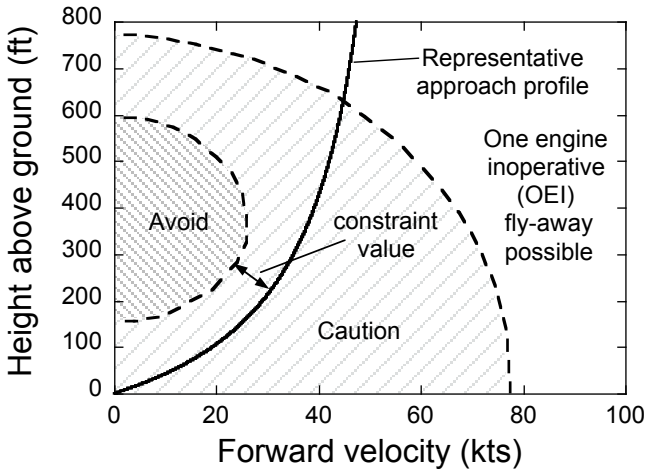

Figure 2.15: Graphical depiction of the behavior constraint for flight outside the "avoid" region on a typical H-V diagram [2].

$\mathbf{p}_{VRS}$ are discretized), $\|\cdot\|$ is the Euclidean norm, $\mathbf{p}^i_{app}(\mathbf{X})$ is the i-th point of the entire series of point, i_{all}, defining the approach profile, $\mathbf{X}$, and $\mathbf{p}^j_{VRS}$ is the j-th point of the entire series of points, j_{all}, defining the VRS boundaries.

A third behavior constraint was imposed to prevent flight in the "avoid" region of a representative multi-engine height-velocity diagram. Figure 2.15 shows the boundaries of a representative height-velocity diagram for a multi engine helicopter [47]. A representative approach profile is plotted on the same axes. Similar to the VRS-based constraint, the constraint value is the distance between the closest point on the approach profile and the boundary of the "avoid" region. The constraint is expressed

$$g_3(\mathbf{X}) = \epsilon - min \left\|\mathbf{p}^i_{app}(\mathbf{X}) - \mathbf{p}^j_{HV}\right\| \leq 0 \text{ for all } i, j \tag{2.47}$$

where ϵ is a small number (the exact value will depend on how finely $\mathbf{p}_{app}(\mathbf{X})$ and

$\mathbf{p}_{HV}$ are discretized), and $\mathbf{p}_{HV}^{j}$ is the j-th point of the entire series of points, j_{all}, defining the H-V "avoid" region boundaries.

2.7.4 Approximate Problem Formulation

Because of the high computational cost of a brownout simulation, the optimization problem cannot be solved by directly connecting the simulation and the optimizer. Instead, the baseline optimization problem is converted into a sequence of computationally inexpensive approximate optimization problems in which objective function and behavior constraints are replaced by Taylor series expansions that are updated at each step of the sequence. The general approach is to replace the objective function, $B(\mathbf{X})$, by a second-order Taylor series expansion about the current design.

This approach was implemented in modified form originally proposed by Vanderplaats [48], [49], in which the optimization begins from the *linear* expansion and the quadratic terms are built one at a time as successive approximate optimization problems are solved; the resulting approximate optima are analyzed precisely. A full quadratic expansion may never be actually built, especially for larger problems where the number of objective function evaluations needed to complete the Hessian of the expansion may never become available. Given the way in which the approximation is constructed, the gradient and the Hessian of the expansion are built from designs that may not be "finite difference close," i.e., with small increments of the design variables. As a consequence, the expansion is to be interpreted more as a

general quadratic polynomial interpolation that is valid for broad regions of the design space, rather than a rigorous, but only a locally valid, Taylor series expansion. It is important to impose move limits on the designs of approach profiles when formulating the optimization as an approximate problem. In the current study, the move limits used are the second set of limits imposed in [2], which allows each new design to traverse up to 25% of the design space in a single optimization step:

$$-0.25(\mathbf{X}_{max} - \mathbf{X}_{min}) \leq \mathbf{X}_k - \mathbf{X}_{k-1} \leq 0.25(\mathbf{X}_{max} - \mathbf{X}_{min}) \tag{2.48}$$

Additional designs can be added to the process to better explore the design space. In the context of the problem, there is a possibility of multiple local minima, and hence it is necessary to explore the design space as much as possible to reach a possible global minimum. Additional approach profiles can be generated to be as perpendicular as possible to the previous profiles (i.e. designs as different as possible). These extra designs improve the overall properties of the optimization by improving the accuracy of the Taylor series expansions used for the approximate problems. Furthermore, they give the optimization a measure of global convergence.

Trim variables (Alg. Eqns)	**States (ODEs)**
Pilot controls	
Fuselage pitch and roll	Fuselage pitch and roll
Fuselage wind-axes angles	Body-axes velocities
Dynamic inflow coefficients	Dynamic inflow coefficients
Tail rotor inflow ratio	Tail rotor inflow ratio
Rotor mode #1: constant part	Rotor blade #1: mode #1 and rate
Rotor mode #1: cos+sin 1/rev	Rotor blade #2: mode #1 and rate
Rotor mode #1: cos+sin 2/rev	...
...	Rotor blade #N_b: mode #1 and rate
Rotor mode #1: cos+sin N/rev	Rotor blade #1: mode #2 and rate
Rotor mode #2: constant part	Rotor blade #2: mode #2 and rate
Rotor mode #2: cos+sin 1/rev	...
...	...
...	...
Rotor mode #M: cos+sin N/rev	Rotor blade #N_b: mode #M and rate

Table 2.1: Differences between trim variables and states.

Chapter 3

Results

The following chapter desribes the results of the present study. First, the results of the trim validation for the modeling coupling is presented. Second, the results of the approach profile following are shown. Lastly, the results of the brownout mitigation study are presented.

3.1 Model Coupling Results

This section describes the results of the model coupling trim validation. The rotorcraft model is based on a exemplar single rotor, medium lift rotorcraft configuration and the main parameters are given in Table 3.1. For the present study five blade modes were used, with each blade being discretized into four finite elements. The blade modes and their natural frequencies are given in Table 3.2.

The coupled model simulations are performed on a 2.8 GHz Intel Core i5 processor Apple iMac with four cores and 12 GB of RAM. The multiple cores were utilized to parallelize both the flight dynamics model and the FVM model using OpenMP. Because the blades are assumed to be independent of each other, the flight dynamics model has been parallelized around the blade loop (in the loop structure discussed in the previous chapter). The FVM model has also been parallelized in its calculation of the induced velocity field. Because the induced velocity at each

MAIN ROTOR	
Number of blades	4
Radius R, ft	26.83
Blade chord c, ft	1.75
Rotational speed Ω, rad/sec	27
Longitudinal mast tilt i_θ, deg	-3.0
Airfoil section	SC 1095
First airfoil section, ft	5.08
Blade precone β_p, deg	0.0
Lock number γ	5.11
FUSELAGE	
Roll inertia I_{xx}, lbs-ft^2	4659.0
Pitch inertia I_{yy}, lbs-ft^2	38,512.0
Yaw inertia I_{zz}, lbs-ft^2	36,796.0
I_{xz}, lbs-ft^2	1,882.0
Horizontal tail surface area, ft^2	45.0
TAIL ROTOR	
Number of blades	4
Radius R_{tr}, ft	5.5
Blade chord c_{tr}, ft	0.81
Rotational speed Ω_{tr}	124.62
Rotor shaft cant angle, deg	20.0

Table 3.1: Main parameters of the exemplar single rotor helicopter configuration.

Mode Number	**Mode Type**	Frequency (/rev) 4 FEM
1	1st flap	1.0352
2	1st lag	0.2680
3	pure torsion	5.0515
4	flap-torsion	4.6364
5	2nd flap	2.8224

Table 3.2: Blade natural frequencies

point only depends on the geometry of the wake and the tip vortex strength, it is not dependent on induced velocity at any other points in the field and can easily be parallelized. The parallelization increases the computational efficiency of the simulation and reduces run times on the order of four times. For example, for a trim solution to be reached, total run time per flight speed is between five and ten minutes of wall-clock time. An approach profile requires on the order of 12 hours per approach profile. Simulation can differ based on the specific aggressiveness of the required approach profile, and can reach as long as 15 hours for the most aggressive landings.

3.1.1 Flight Dynamics and FVM Model Coupling Validation

This section discusses the trim results from a variety of altitudes and gross weights which are given in Table 3.3. The trim results have been compared to flight test data from [50] which was obtained for the corresponding weights and altitudes. It should be noted that the airspeeds tested start from 1 kts, as 0 kts creates a singularity in the model.

The required rotor power in trim results are presented in Figs. 3.1–3.5 and

Altitude (ft)	**Gross weight (lb)**
3,777	16,348
7,780	16,440
10,440	16,960
13,230	17,020
16,770	16,660

Table 3.3: Trim test density altitudes and corresponding aircraft gross weights.

are plotted against the flight test data for a range of speeds. At low altitudes below 13,230 ft, there is very good agreement between the flight test data and the model, especially in the intermediate range of speeds. Consistently at all altitudes at speeds below 40 knots, the power is under predicted. While there is a lack of flight test data at the lower speeds, one factor in the lower prediction of power is that the flight dynamics model does not include the effect of the downwash of the rotor on the fuselage and empennage. At higher speeds, the rotor wake is convected quickly behind the rotor and the influence of the downwash on the airframe is much less pronounced. At lower speeds, the wake remains closer to the rotor, and so there is more interference between the wake and the fuselage, increasing drag on the fuselage and so increasing the power required. Without this interference in the model, the power required that results is much smaller.

At intermediate altitudes, as shown in Figs. 3.2 and 3.3, the agreement over the range of air speeds from 40 kts and higher is quite good. However, the required power at higher altitudes of 13,230 feet and 16,660 feet for speeds greater than 40 kts is over predicted, especially at the highest speeds, as shown in Figs. 3.4 and 3.5 respectively. The over-prediction of power is much more significant at 16,660 feet. Factors that may cause this are the difficulties in modeling stall and fuselage aerodynamics; the fuselage aerodynamics represented by empirical data. In addition, the flight dynamics model does not take tip sweep into account, and models an equivalent straight blade. Ribera [28] demonstrated that power predictions were lowered by the presence of a swept tip because of the lower induced inflow over the rotor that is produced by the swept tip.

Additionally, in Figs. 3.6–3.8, the three trim pilot stick inputs are plotted against the airspeed for the flight condition at a density altitude of 3,777 ft. The stick inputs are presented as a percentage of the control excursions, with 0% and 100% being full throw in either direction. Overall, the results of the trim stick inputs are consistent with the findings in both [28] and [19]. Figure 3.6 shows the pilot's collective input, and it can be seen that at speeds above 40 kts there is good agreement between the trim solution and the test data. At lower speeds the power is under predicted, as previously seen with the power calculation. The pilot longitudinal cyclic input, shown in Fig. 3.7, shows good agreement at intermediate speeds, but at lower speeds displays an opposite trend to that of the flight test data. This effect can also be explained by the fact that the effect of the downwash on the fuselage and empenage is not modeled. The pilot lateral cyclic input, shown in Fig. 3.8, shows decent agreement over the full range of airspeeds, except for two points near 30 kts. This result is consistent with the trim lateral stick inputs found by Ribera [28].

It is important to note that the trim convergence is sensitive to the initial solution used in the simulation, which was also seen by Ribera [28] in the initial coupling of the wake model. The new trim organization has helped partially to alleviate this issue by calculating trim with dynamic inflow first, which is slightly less affected by differences in the initial solution. However the convergence is still sensitive to the initial solution. A poor initial condition has the potential to lead to a failure to converge. It has been found that speeds below 80 kts are particularly sensitive with speeds below 30 kts being the most sensitive. To ensure that this problem

does not effect the optimization process (which begins from trim), a database of trim solutions was calculated from the dynamic inflow trim solutions for a range of airspeeds from 1 kts to 150 kts. At the beginning of each optimization step before trim begins, the proper solution corresponding to the initial flight condition is input as the initial trim solution.

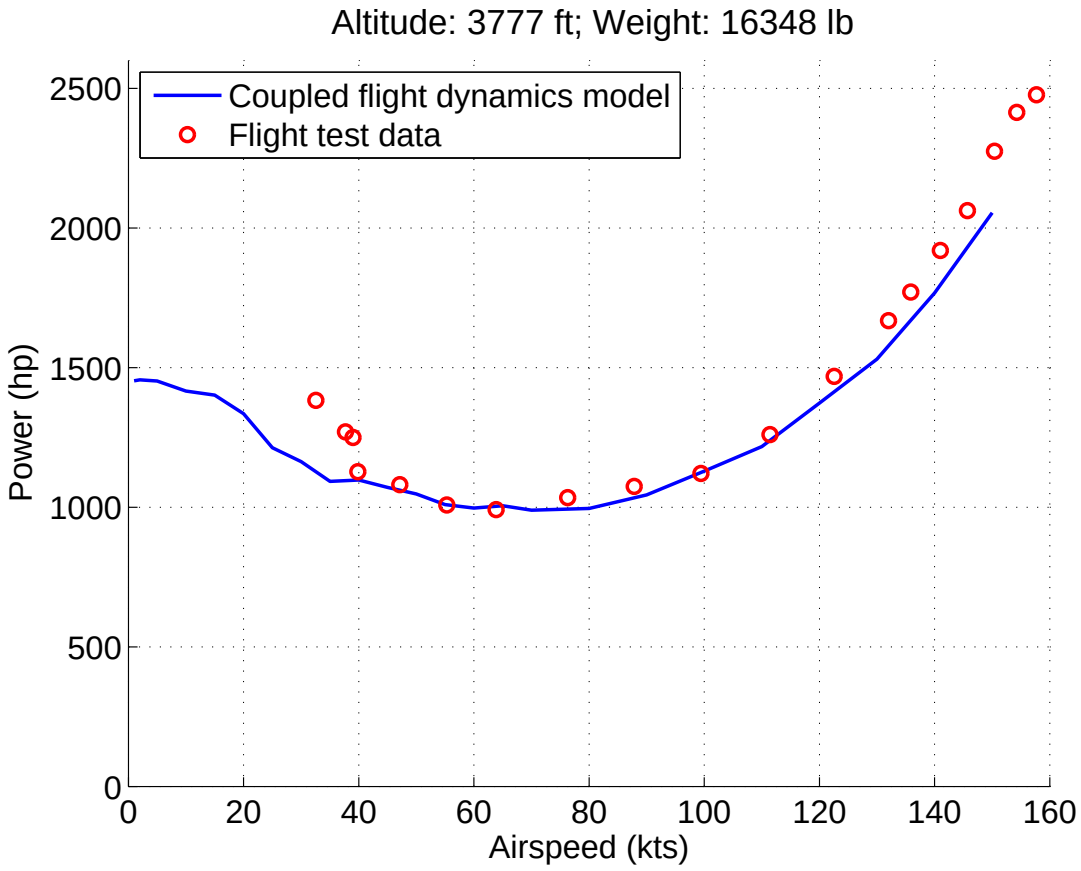

Figure 3.1: Main rotor power required vs. airspeed for an altitude of 3,777 ft.

3.2 Approach Profile Following Results

This section details the results of the approach profile following. Because there are three sets of controllers based on flight path descent angles of 0°, 6°, and 12°,

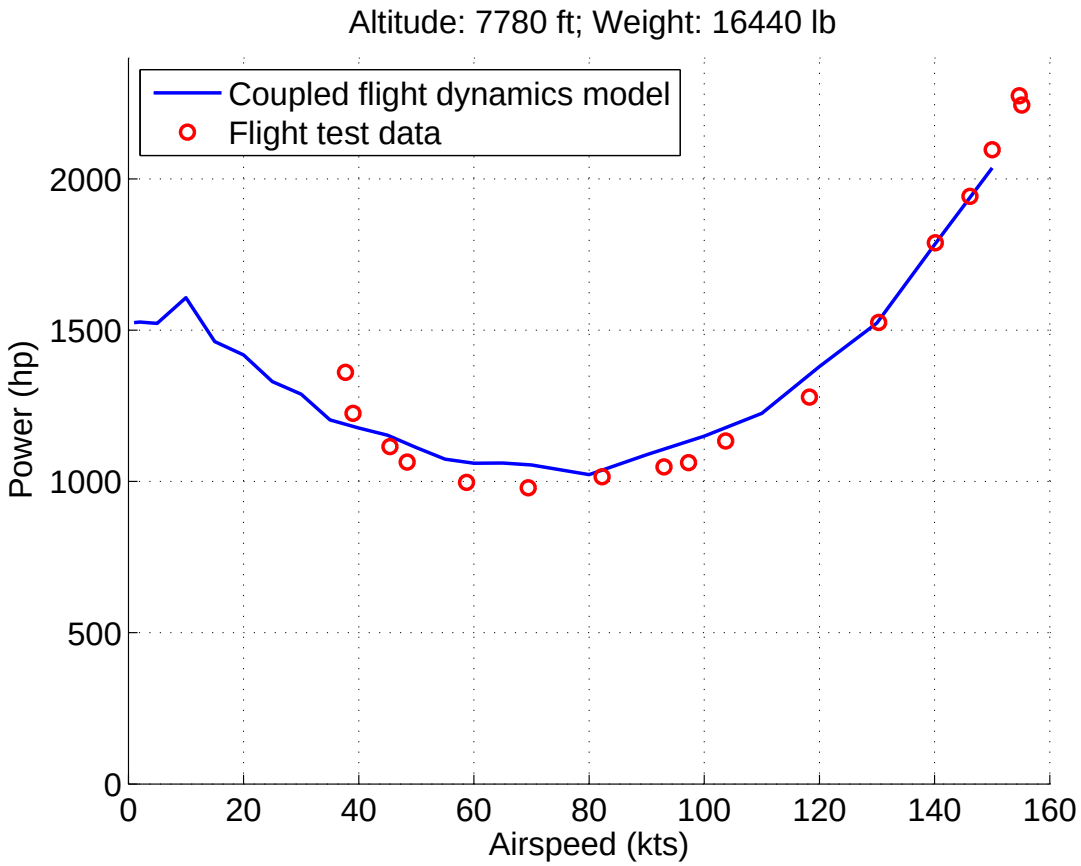

Figure 3.2: Main rotor power required vs. airspeed for an altitude of 7,780 ft.

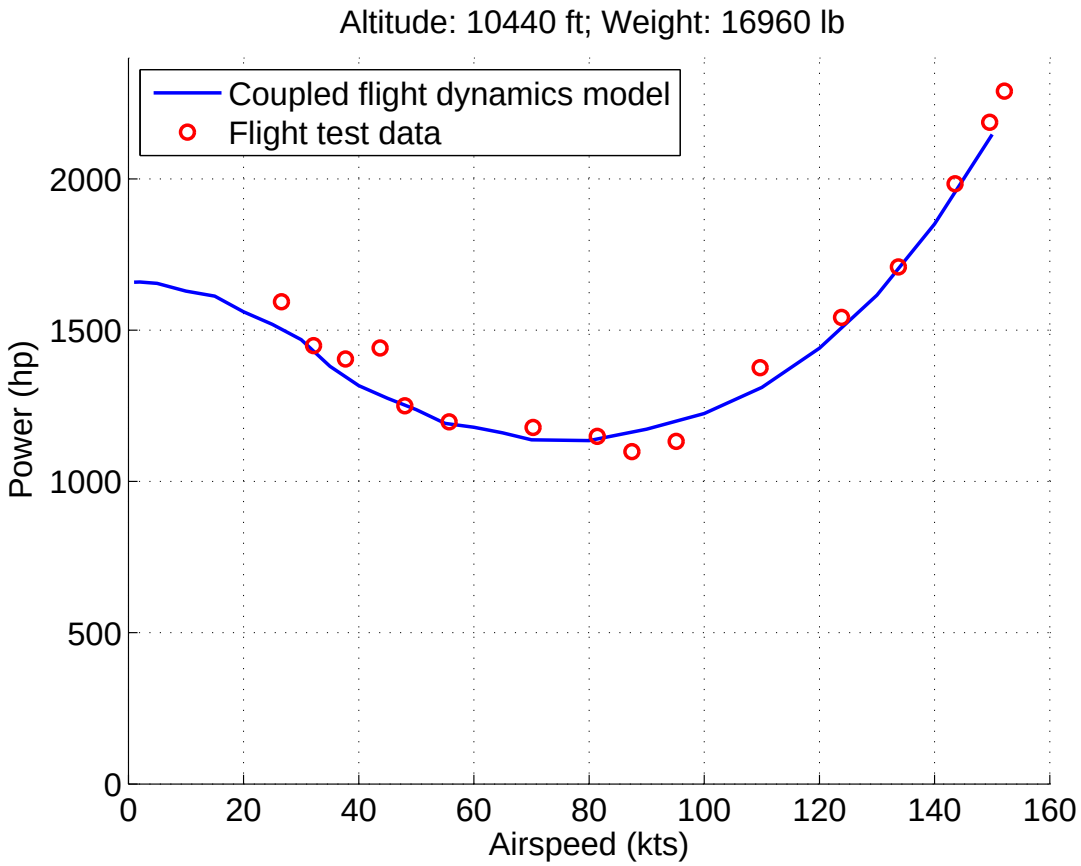

Figure 3.3: Main rotor power required vs. airspeed for an altitude of 10,440 ft.

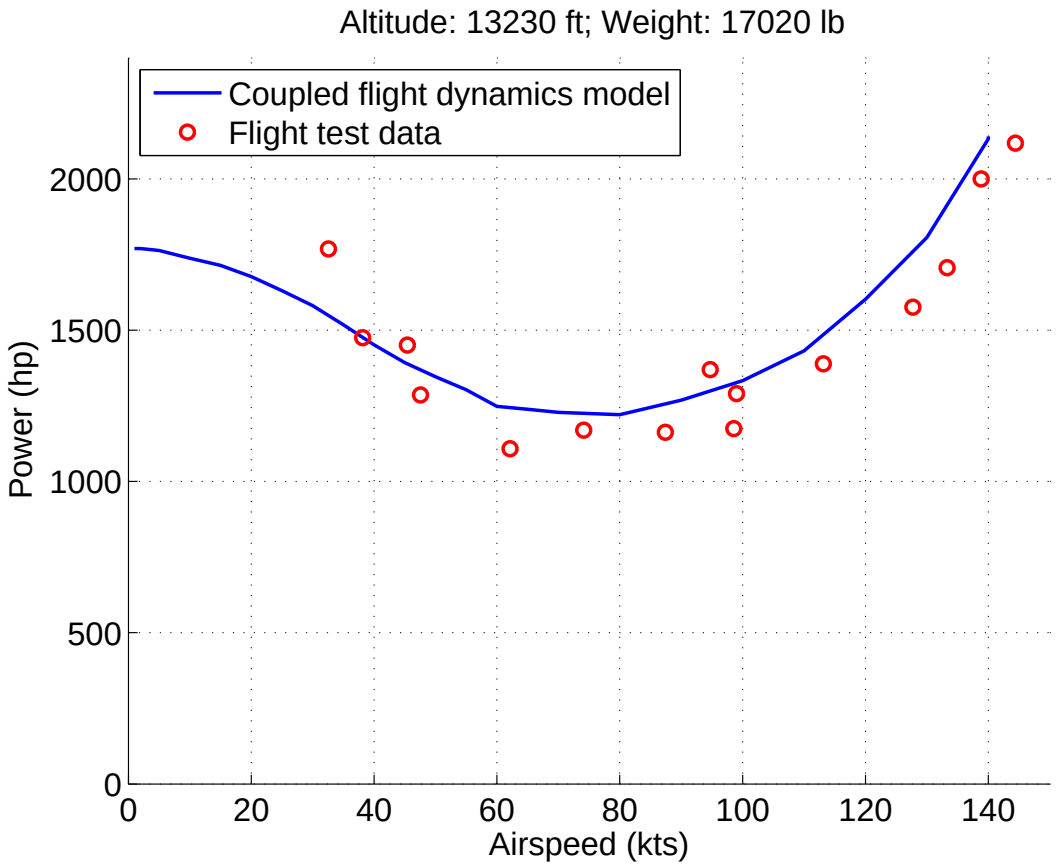

Figure 3.4: Main rotor power required vs. airspeed for an altitude of 13,230 ft.

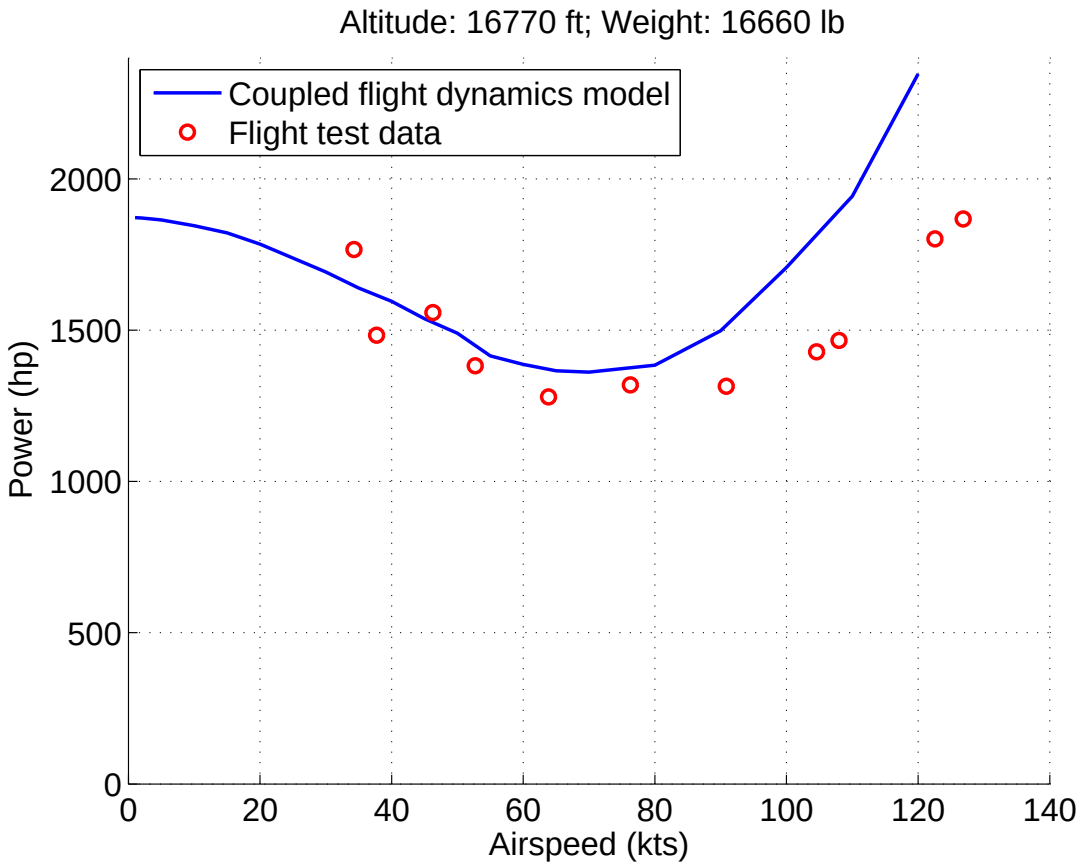

Figure 3.5: Main rotor power required vs. airspeed for an altitude of 16,770 ft.

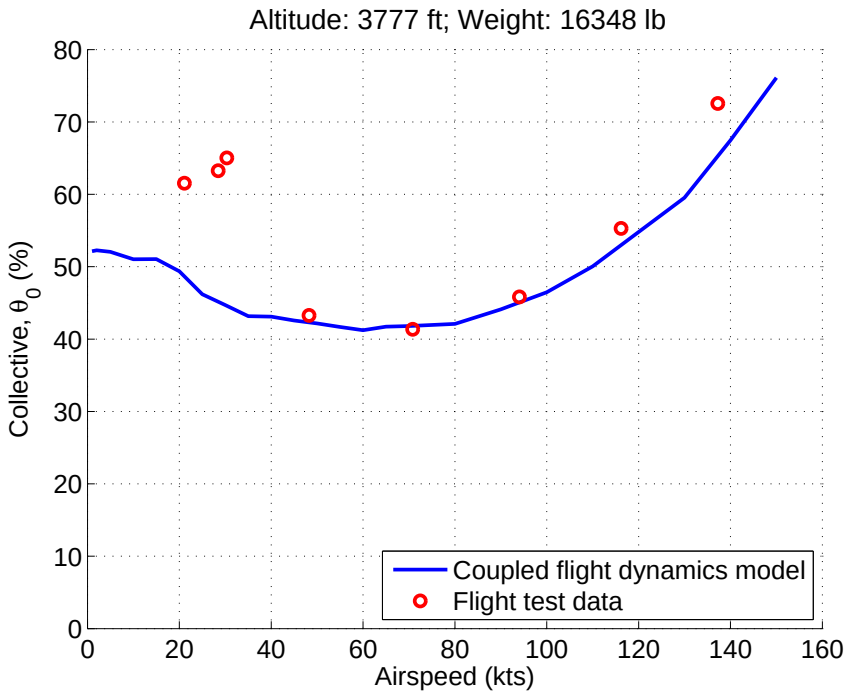

Figure 3.6: Pilot collective input θ_0 vs. airspeed for an altitude of 3,777 ft.

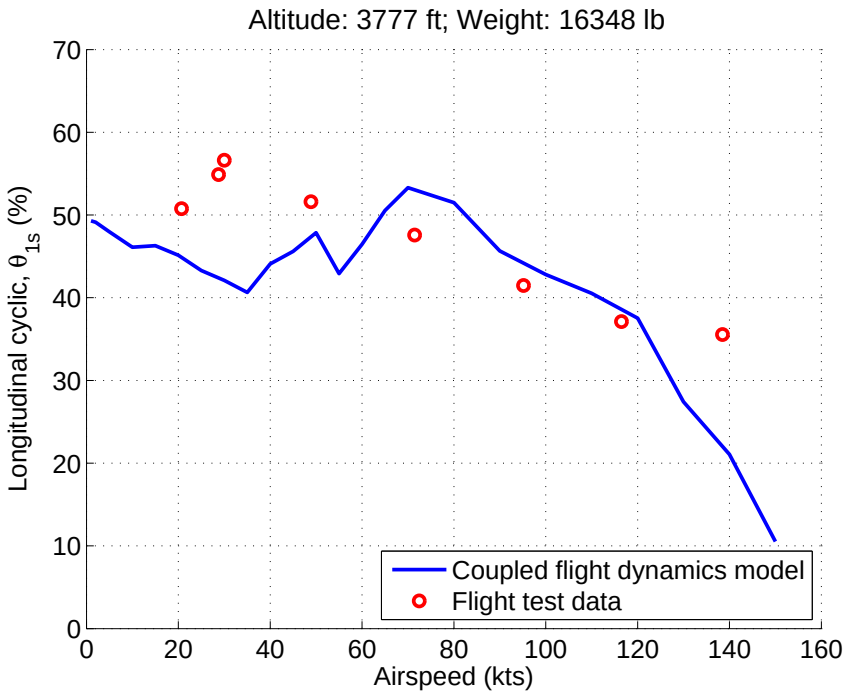

Figure 3.7: Pilot longitudinal cyclic input vs. airspeed for an altitude of 3,777 ft.

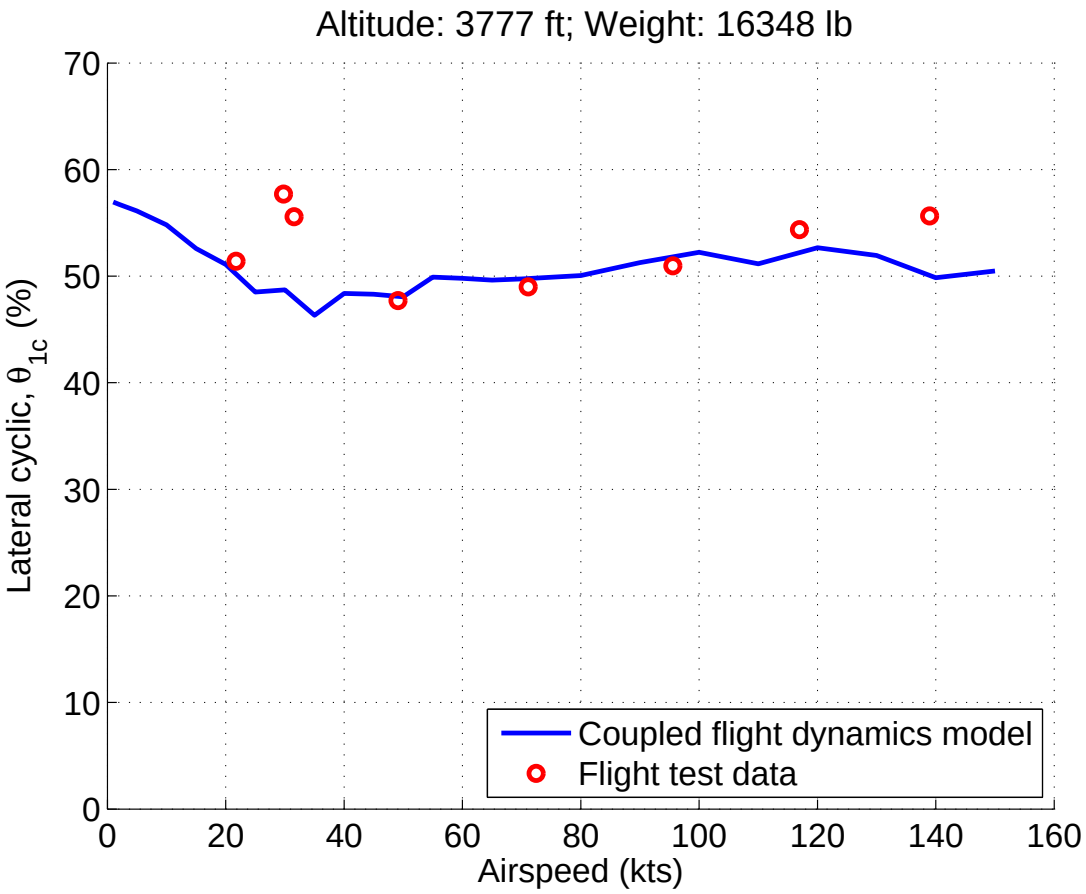

Figure 3.8: Pilot lateral cyclic input vs. airspeed for an altitude of 3,777 ft.

three approach profile (one from each set) simulations are presented here. Each profile begins at a intermediate range speed, and hence a good range of speeds are covered demonstrating the broad effectiveness of the controller. Because of the similarity between the different sets of controllers and so as to not be repetitive, full results are given for the 6° set, which represents a median of the two extremes, and only the trajectory results will be presented for the other two sets. The data for the 6° and 12° approach profiles are from the flights used during the optimization process, while the data for the 0° set is from a test case performed earlier. Each of the cases were performed at a weight of 16,000 lb with density $\rho = \rho_0$ (MSL, ISA).

The first approach profile is for the case $\mathbf{X} = [6^\circ \;\; 110 \text{ kts} \;\; 300 \text{ ft}]^T$, which is near to the baseline case. The results for this case are given in Figs. 3.9–3.14. Fig. 3.9 shows the side, top, and rear views of the actual profile compared with the desired profile. The time steps that correspond to the current position are also shown. It can be seen that there is good agreement between the actual and desired profiles. Position tracking is the most important states to track in the present simulation, because dust cloud simulation defines a distinct bed of particles as the landing area, as it can become computationally inefficient to model a large area of particles. As shown in Fig. 3.9, the 6° controller set is tracking position well. The error of the actual trajectory versus the desired profile for all three body positions is less than one percent.

The time-histories of the body positions, body velocities, Euler body angles, and pilot stick inputs of the actual profile are shown in Figs. 3.10–3.13, respectively. In each figure, the landing zone is marked at the time that it is reached. For the

present study, the approach profile is formulated so that all approach profiles have the same duration (about 48 seconds), and hence in some cases there is extended time at the end of the simulation where the helicopter remains in hover in the landing zone. The body positions and velocities in Figs. 3.10 and 3.11 have also been plotted against their desired profiles. As was shown for the trajectories, the time-histories for both the position and velocity demonstrate very good tracking of the desired profiles. There is a very slight offset of the u velocity seen in the top panel of Fig. 3.11, but overall the tracking is good.

Figure 3.12 shows the resulting Euler body angles during the maneuver. The pulling-up motion of the helicopter as it lands can be clearly seen in the pitch angle θ response. The peak of the pitch response corresponds directly to the maximum deceleration seen during the approach profile, which can be seen in the u plot in Fig. 3.11. Once the landing zone is reached, the pitch angle settles to a lower non-zero angle pitching up. The slight tilt of the fuselage is a response primarily because of the fact that fuselage center of gravity (CG) is slightly behind the main rotor CG. For the helicopter to have zero airspeed the thrust vector from the main rotor must be in line with gravity vector and have no moments created. Because there is a 3° forward shaft tilt angle, the fuselage must tilt nose-up to line the fuselage CG underneath the rotor CG, resulting in a downwards tip-path-plane tilt, and a fuselage pitch up. The other Euler angles, roll and yaw, both change during the maneuver, but settle near to zero once the landing zone is reached. The time-history of the pilot stick inputs is shown in Fig. 3.13. The inputs seem to oscillate around a certain value and stay within reasonable bounds. It is important to note

that because there is no pilot model implemented, the control inputs are very fast, with no delay. A human pilot moves the controls much more smoothly, and these extremely fast oscillations would not be produced in practice. However, because the only goal to model the approach profile as closely as possible, the pilot stick inputs are responding to produce the correct profile.

A time-history of the wake geometry at different points in the approach profile is shown in Fig. 3.14. In the first panel, the wake is shown at 17.5 seconds while the helicopter is still in level flight. At 23.3 seconds the wake begins to impinge on the ground and the initial effects of the wake in ground-effect can be seen. In the bottom panel at 33.5 seconds, the helicopter is hovering inside the landing zone, and the wake spreads out as a consequence of ground-effect. The slight pitch down of the tip-path-plane of the main rotor can be seen in the bottom panel when the helicopter is in hover, and corresponds to the fuselage/main rotor CG balance discussed previously.

The approach profile in the 0° set consisted of $\mathbf{X} = [2.8^\circ \;\; 120 \text{ kts} \;\; 300 \text{ ft}]^T$ and its trajectory results are presented in Fig. 3.15. This is a fairly aggressive approach profile because of the higher speed of the landing. As was shown previously, the tracking of the states is very good; the overall error for this set of controllers is about 2 %. The results for the 12° set were very similar. The approach profile for this set is $\mathbf{X} = [12^\circ \;\; 72 \text{ kts} \;\; 180 \text{ ft}]^T$, and are shown in Fig. 3.16. This case also demonstrated extremely good tracking of the position states. Overall, the performance of the approach profile following implementation is very good and tracks specific approach profiles with little error, necessary for the dust cloud simulation.

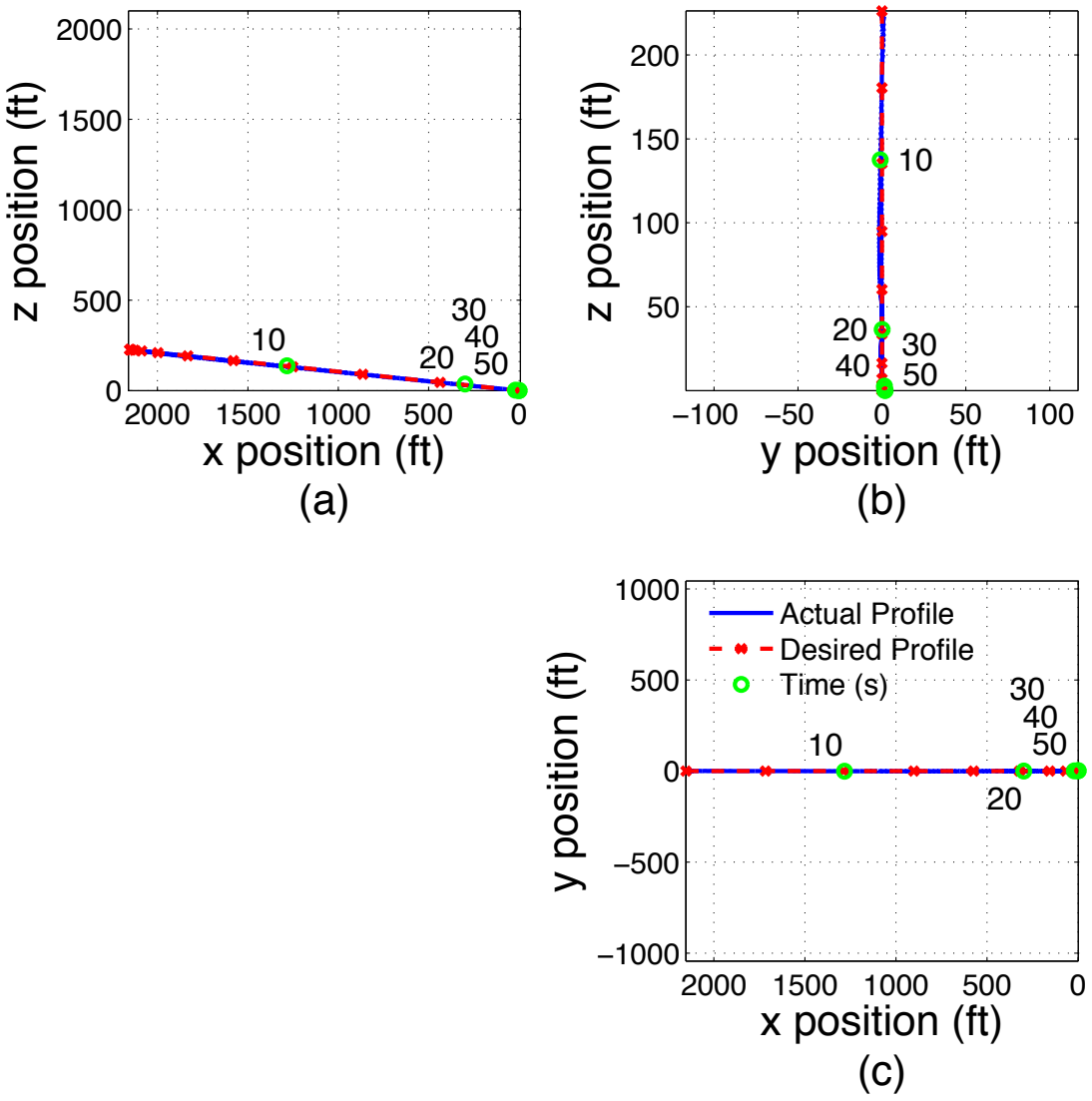

Figure 3.9: (a) Side, (b) rear, and (c) top views of the actual flight trajectory compared to the desired approach profile for $\mathbf{X} = [6^\circ \;\; 110 \text{ kts} \;\; 300 \text{ ft}]^T$.

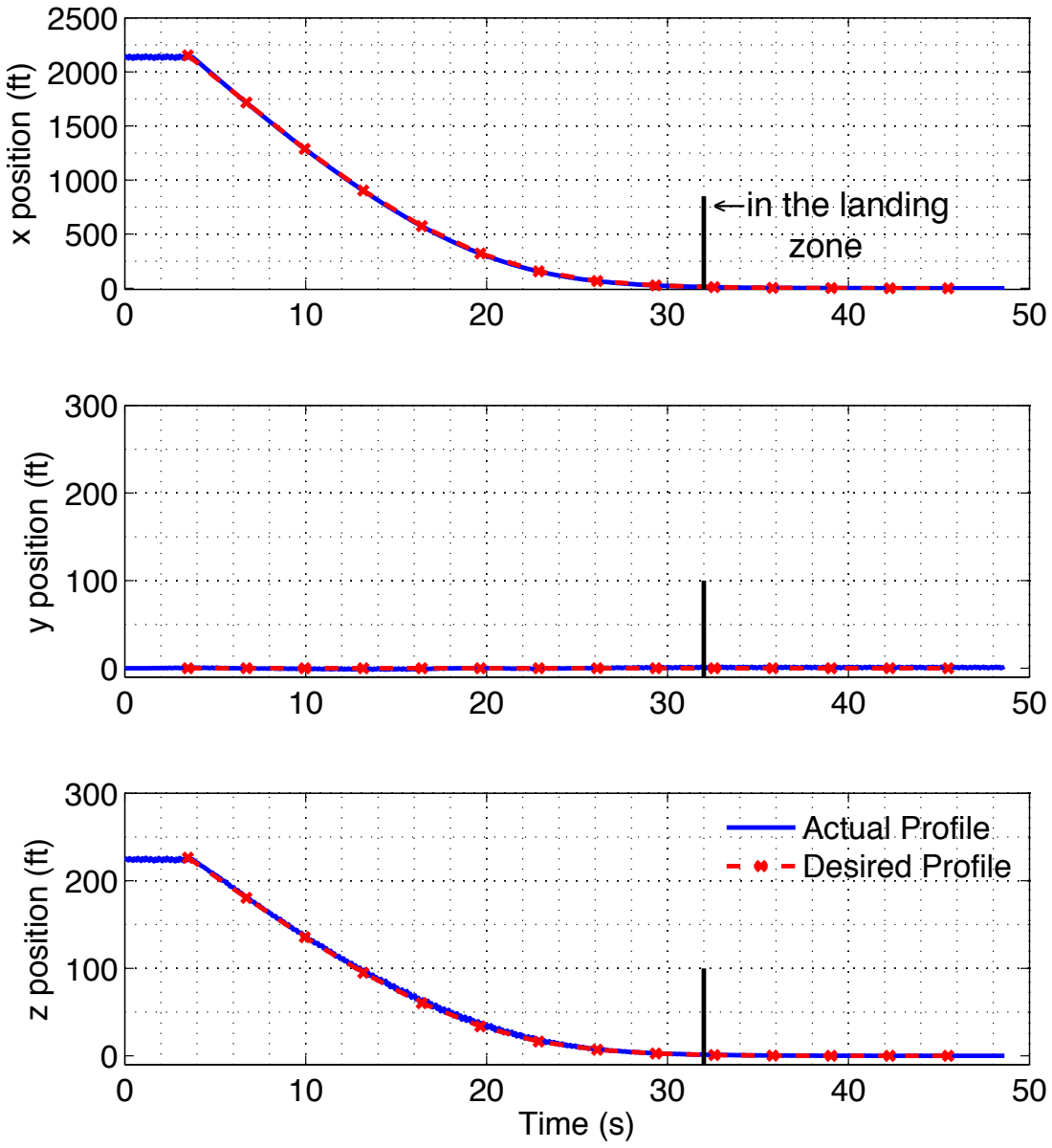

Figure 3.10: Time history of body positions of the actual flight trajectory compared to the desired approach profile for $\mathbf{X} = [6^\circ \;\; 110 \text{ kts} \;\; 300 \text{ ft}]^T$.

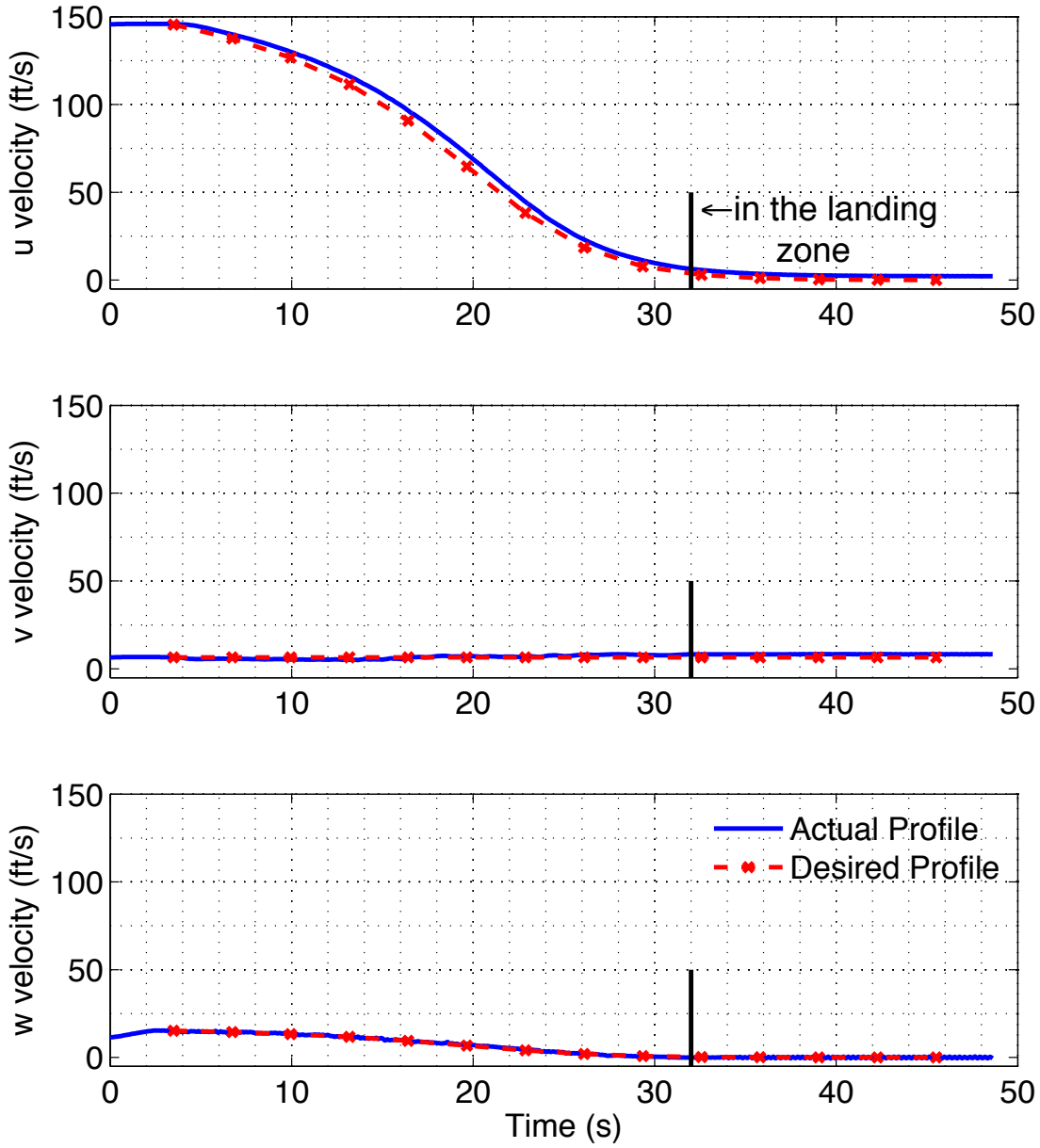

Figure 3.11: Time history of body velocities of the actual flight trajectory compared to the desired approach profile for $\mathbf{X} = [6^\circ \;\; 110 \text{ kts} \;\; 300 \text{ ft}]^T$.

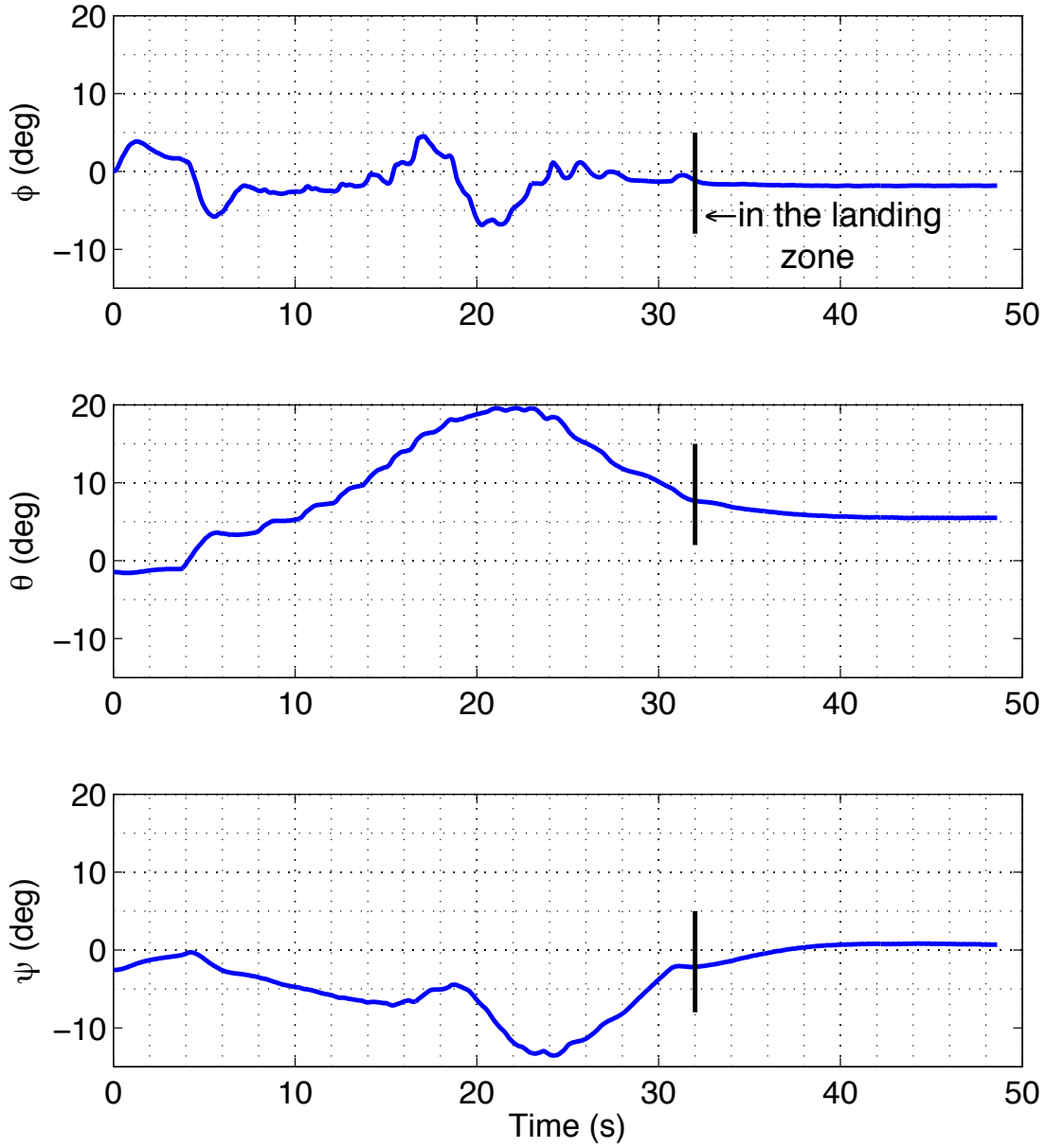

Figure 3.12: Time history of Euler body angles of the actual flight trajectory compared to the desired approach profile for $\mathbf{X} = [6^\circ \;\; 110 \text{ kts} \;\; 300 \text{ ft}]^T$.

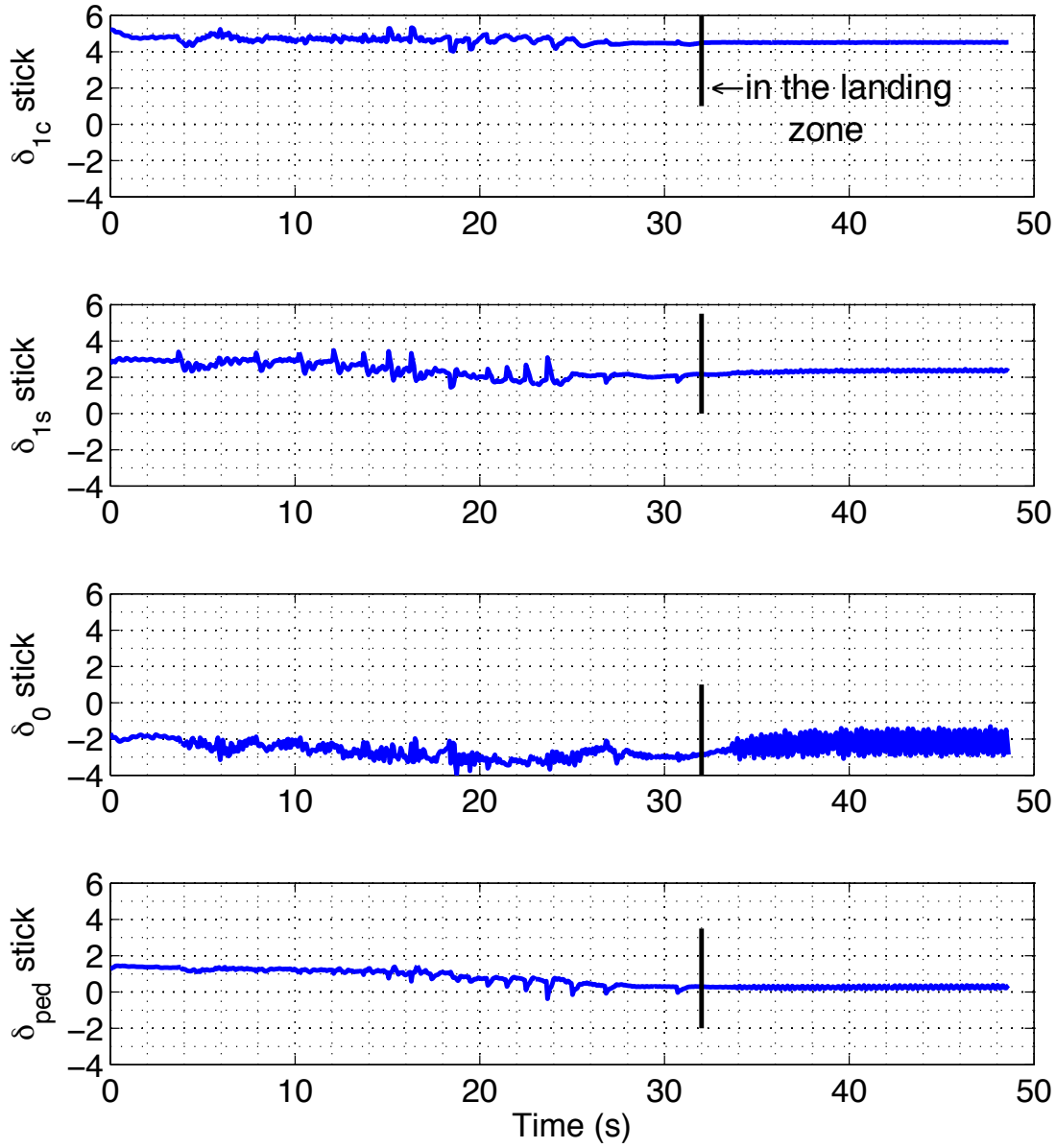

Figure 3.13: Time history of pilot stick inputs of the actual flight trajectory compared to the desired approach profile for $\mathbf{X} = [6^\circ \;\; 110 \text{ kts} \;\; 300 \text{ ft}]^T$.

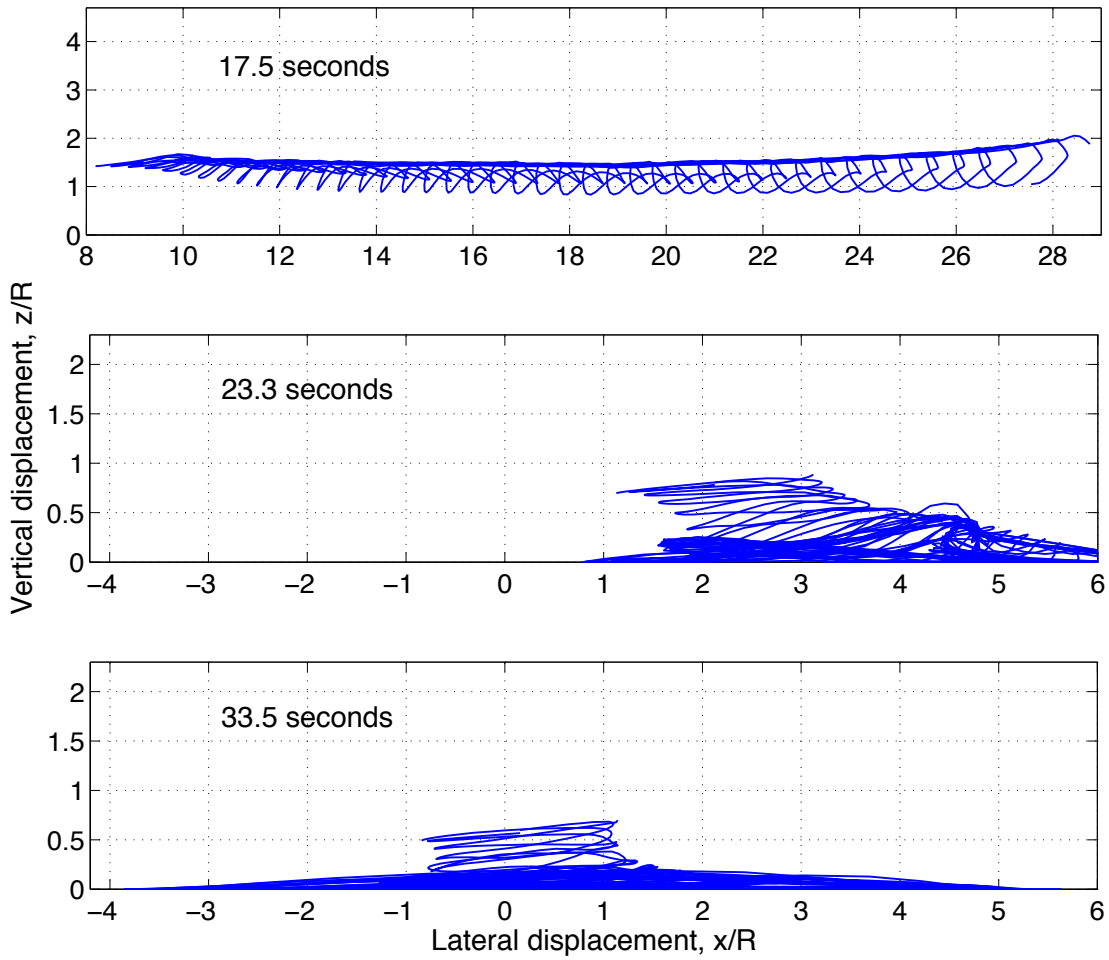

Figure 3.14: Side view of wake geometries at different time during the approach profile simulation for $\mathbf{X} = [6^\circ \;\; 110 \text{ kts} \;\; 300 \text{ ft}]^T$.

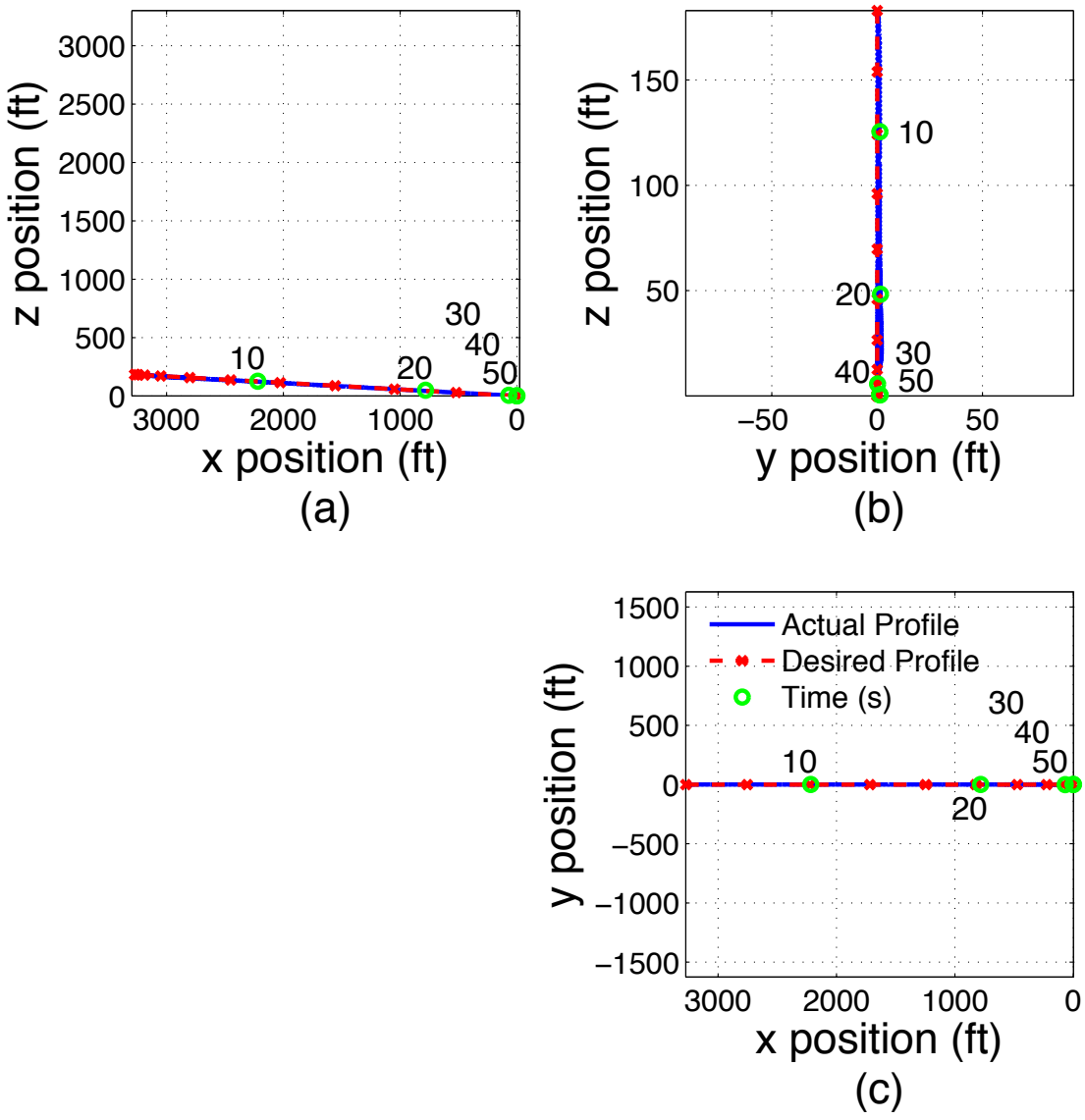

Figure 3.15: (a) Side, (b) rear, and (c) top views of the actual flight trajectory compared to the desired approach profile for $\mathbf{X} = [2.8^\circ \;\; 120 \text{ kts} \;\; 300 \text{ ft}]^T$.

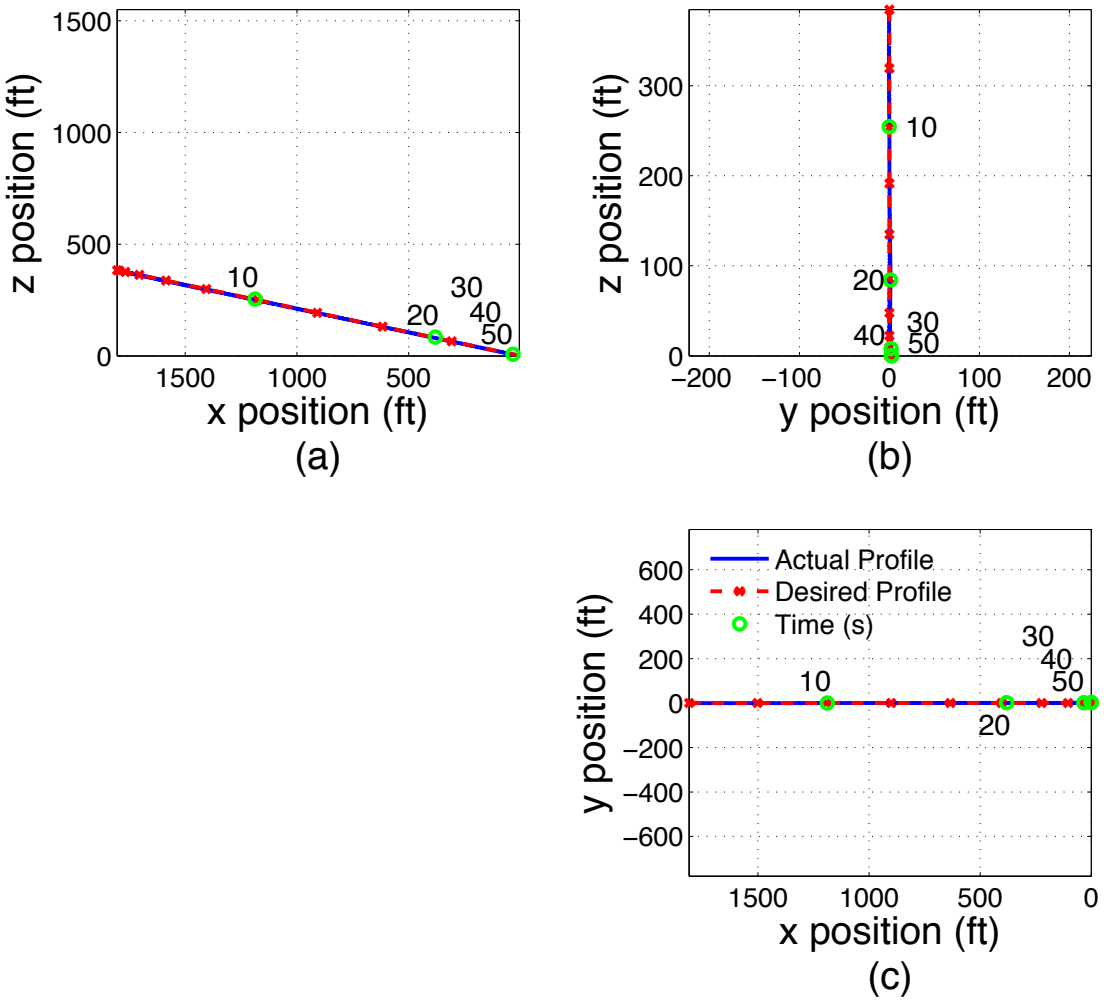

Figure 3.16: (a) Side, (b) rear, and (c) top views of the actual flight trajectory compared to the desired approach profile for $\mathbf{X} = [12^\circ \;\; 72 \text{ kts} \;\; 180 \text{ ft}]^T$.

3.3 Brownout Flight Path Optimization Results and Discussion

This section presents the results of the brownout mitigation through flight path optimization study. The results of the study, the physical interpretation of the results, and a comparison to the Tritschler [2] study are detailed. As mentioned earlier, it is important to note that this optimization is for a specific formulation of the approach profile, namely a formulation based on approach angle, initial velocity, and peak deceleration range. Other possible approaches such as a curved paths or approaches with extended higher hovers before landing cannot be modeled cusing the current methodology.

A brownout simulation run time can be anywhere between 12 and 15 hours of wall clock time, depending on the aggressiveness on the approach profile and takes between 4 and 20 GB of computer memory, depending on how many particles are uplifted. All results have been presented in a similar manner to that of the optimization study by Tritschler to enable direct comparisons.

3.3.1 Optimization Results

A summary of the optimization steps is presented in Fig. 3.17 as well as in two-dimensional contour plots of the approximate objective function, $B(\mathbf{X})$ in Figs. 3.18 through 3.32. Additionally, Table 3.4 details the step number, design vector $\mathbf{X}$, and corresponding objective function for each step. The contour plots show each of the approaches that have already been evaluated have been marked with circle, and the next approach profile to be evaluated and its estimated objective function

with diamond ($\mathbf{X}^*$). To visualize the three dimensional space, the peak range of deceleration r_{pd} is shown as five slices of the design space, and approaches are shown in the slice that their respective r_{pd} is the closest to. It is important to note that regions that do not have a contour are where $B_{app}(\mathbf{X}) < 0$, which in the current formulation of the objective function is impossible (it is impossible to have negative particles in the pilot's FOV). The move limits for each case, specified by the dashed lines, were consistent throughout the optimization process and are defined earlier. For the purposes of the optimization, the use of additional designs was minimized to see where the optimizer would naturally move to.

Figure 3.18 shows the first four function evaluations, with $\mathbf{X}_1$ being the baseline approach profile, then $\mathbf{X}_2$–$\mathbf{X}_4$ are the four perturbation approaches necessary to build the gradients of the approximate objective function and constraint functions. At the second step (Fig. 3.19), an additional design was added to the optimization, namely $\mathbf{X}_5$, which was not used to create $\mathbf{X}_4$. This design was evaluated as a test for the approach profile following, and its addition only serves to explore the design space more. The additional design also aids to increase the accuracy of the Taylor series approximation.

Steps $\mathbf{X}_7$–$\mathbf{X}_{13}$ (optimization steps 2–8 shown in Figs. 3.20–3.25) indicate a dramatic decrease in the objective function. These steps demonstrate that the optimizer was moving towards a more shallow approach angle. Because several designs had been chosen in a similar area of the design space, an additional design $\mathbf{X}_{14}$ was evaluated to better explore more of the design space, and resulted in a smaller objective function. As the succeeding approaches moved to a different area

Optimization Step	**Approach, $\mathbf{X} = [\alpha_{app} \;\; v_0 \;\; r_{pd}]^T$**	**Function Value, $B(\mathbf{X})$**
0	$\mathbf{X}_1 = [6.0^\circ \;\; 90.0 \text{ kts} \;\; 300.0 \text{ ft}]^T$	424.9
0	$\mathbf{X}_2 = [6.0^\circ \;\; 110.0 \text{ kts} \;\; 300.0 \text{ ft}]^T$	187.4
0	$\mathbf{X}_3 = [6.0^\circ \;\; 90.0 \text{ kts} \;\; 400.0 \text{ ft}]^T$	815.4
0	$\mathbf{X}_4 = [3.0^\circ \;\; 90.0 \text{ kts} \;\; 300.0 \text{ ft}]^T$	266.3
1	$\mathbf{X}_6 = [3.8^\circ \;\; 120.0 \text{ kts} \;\; 283.5 \text{ ft}]^T$	94.2
additional design	$\mathbf{X}_5 = [4.0^\circ \;\; 90.0 \text{ kts} \;\; 400.0 \text{ ft}]^T$	538.3
2	$\mathbf{X}_7 = [4.2^\circ \;\; 108.2 \text{ kts} \;\; 259.8 \text{ ft}]^T$	107.1
3	$\mathbf{X}_8 = [4.2^\circ \;\; 113.0 \text{ kts} \;\; 305.4 \text{ ft}]^T$	140.3
4	$\mathbf{X}_9 = [5.4^\circ \;\; 120.0 \text{ kts} \;\; 265.1 \text{ ft}]^T$	68.3
5	$\mathbf{X}_{10} = [7.6^\circ \;\; 116.8 \text{ kts} \;\; 261.9 \text{ ft}]^T$	118.0
6	$\mathbf{X}_{11} = [3.2^\circ \;\; 117.4 \text{ kts} \;\; 262.5 \text{ ft}]^T$	117.6
7	$\mathbf{X}_{12} = [5.9^\circ \;\; 120.0 \text{ kts} \;\; 265.1 \text{ ft}]^T$	199.6
8	$\mathbf{X}_{13} = [3.3^\circ \;\; 109.5 \text{ kts} \;\; 287.6 \text{ ft}]^T$	79.5
additional design	$\mathbf{X}_{14} = [12.0^\circ \;\; 60.0 \text{ kts} \;\; 100.0 \text{ ft}]^T$	65.6
9	$\mathbf{X}_{15} = [12.0^\circ \;\; 72.0 \text{ kts} \;\; 180.0 \text{ ft}]^T$	297.9
10	$\mathbf{X}_{16} = [9.8^\circ \;\; 60.0 \text{ kts} \;\; 151.2 \text{ ft}]^T$	343.9
11	$\mathbf{X}_{17} = [9.8^\circ \;\; 72.0 \text{ kts} \;\; 100.0 \text{ ft}]^T$	37.1
12	$\mathbf{X}_{18} = [12.0^\circ \;\; 84.0 \text{ kts} \;\; 100.0 \text{ ft}]^T$	17.3
13	$\mathbf{X}_{19} = [12.0^\circ \;\; 96.0 \text{ kts} \;\; 100.0 \text{ ft}]^T$	13.9
14	$\mathbf{X}_{20} = [9.8^\circ \;\; 105.2 \text{ kts} \;\; 100.0 \text{ ft}]^T$	8.0

Table 3.4: Optimization function evaluations

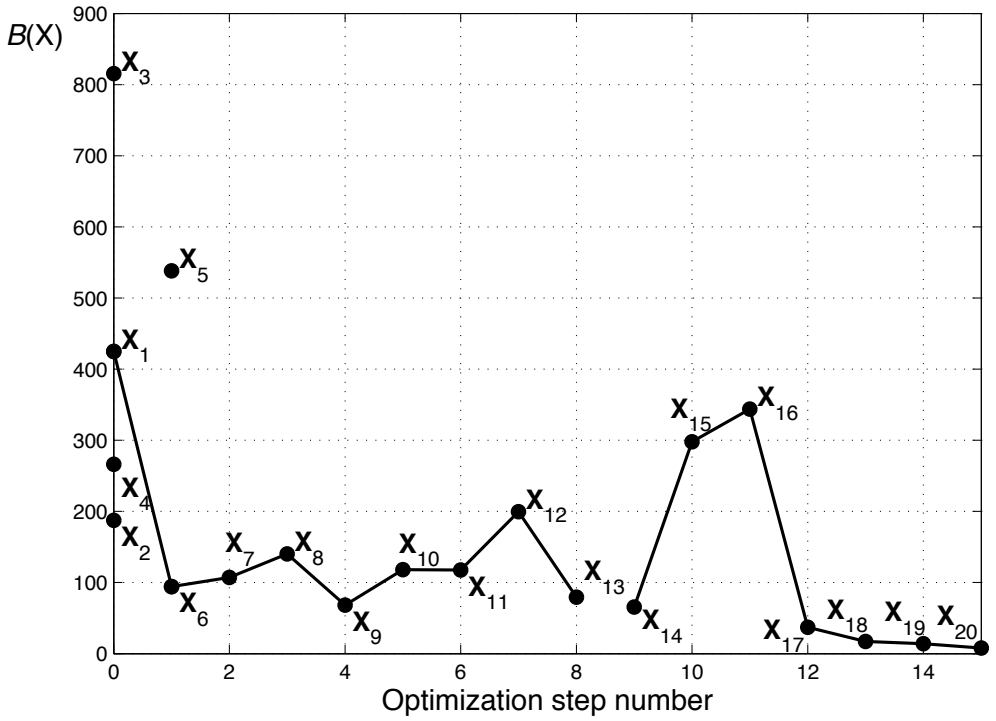

Figure 3.17: Step-history of the optimization objective function.

of the design space near $\mathbf{X}_{14}$, it is clear that a local minimum exists near $\mathbf{X}_9$.

A new optimization path in steps $\mathbf{X}_{14}$–$\mathbf{X}_{20}$ (optimization steps 9–14 shown in Figs. 3.26–3.32) tended towards much steeper and aggressive approach angles and very short periods of deceleration. From $\mathbf{X}_{14}$ the objective function did increase initially as the design space was expanded, however as the approach profile reached the bounds of the design space, the objective function decreased significantly. Steps $\mathbf{X}_{17}$–$\mathbf{X}_{20}$ gave very small objective functions with small improvements between each successive iteration. At this point, the objective function was considered to be converged because the dramatic reduction from the baseline approach and so the optimization was terminated.

As was seen in the study by Tritschler [2], the approximated objective func-

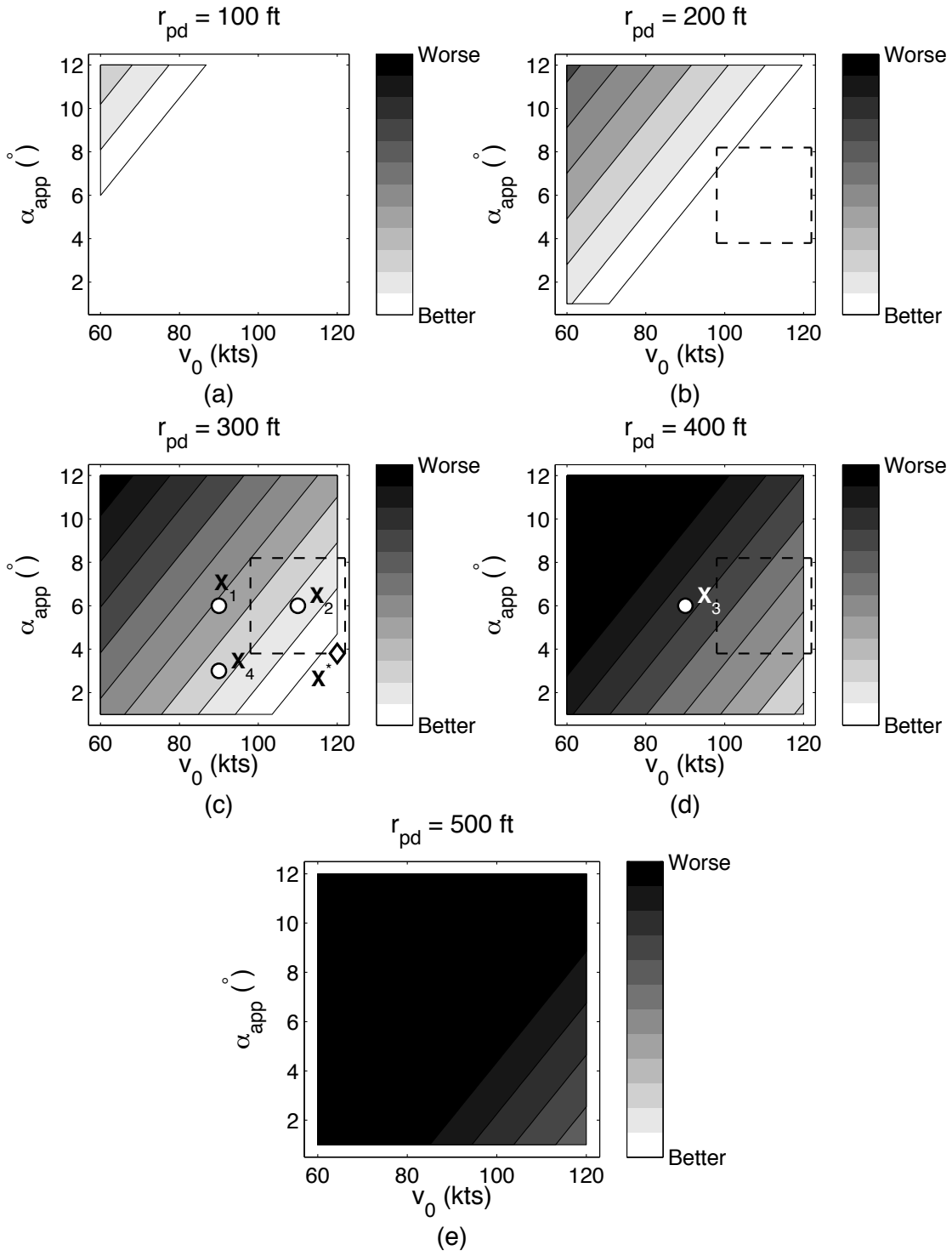

Figure 3.18: Two-dimensional contour maps through the three-dimensional approximate objective function, $B_{app}(\mathbf{X})$, for the first optimization step. Move limits are shown as dashed lines.

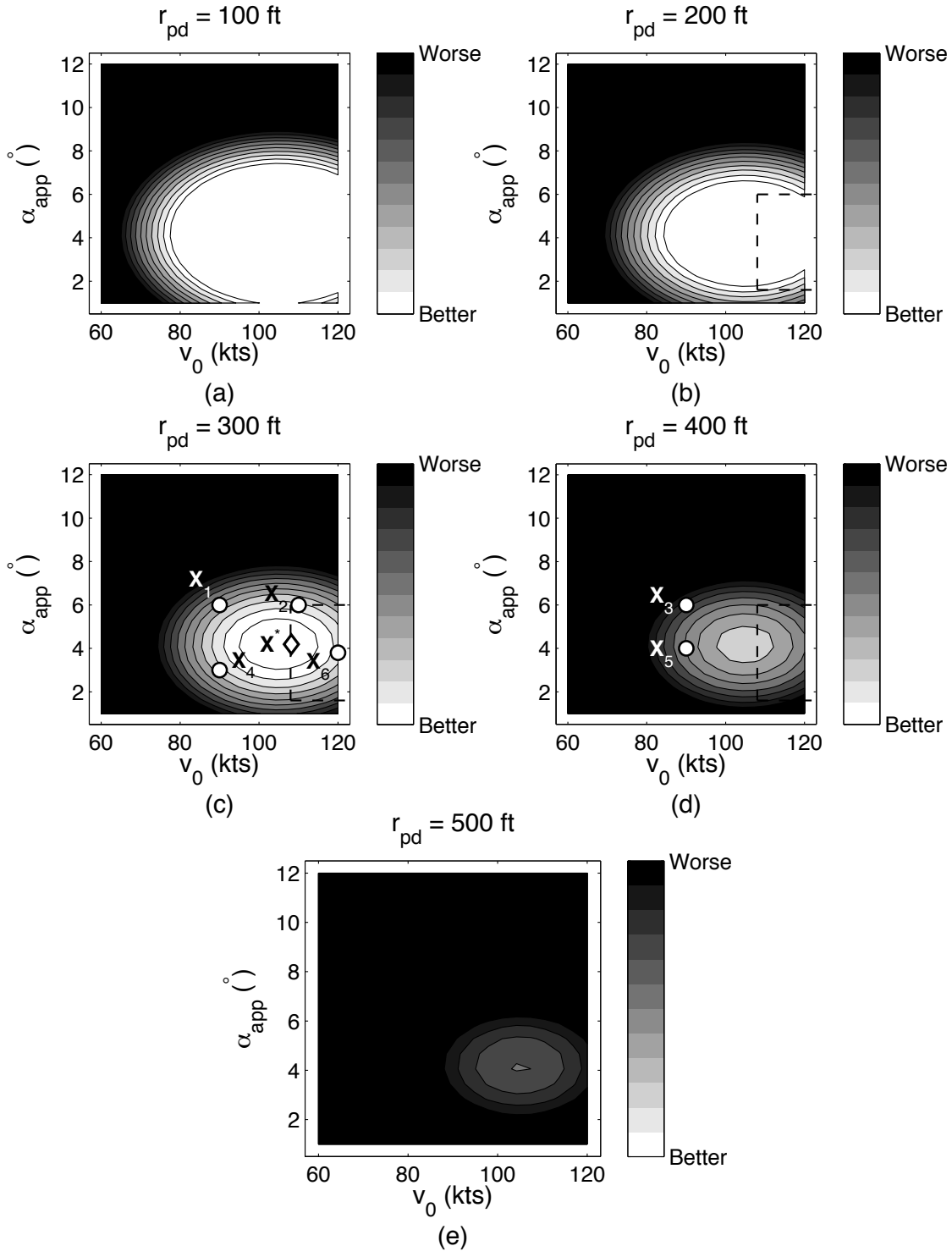

Figure 3.19: Two-dimensional contour maps through the three-dimensional approximate objective function, $B_{app}(\mathbf{X})$, for the second optimization step. Move limits are shown as dashed lines.

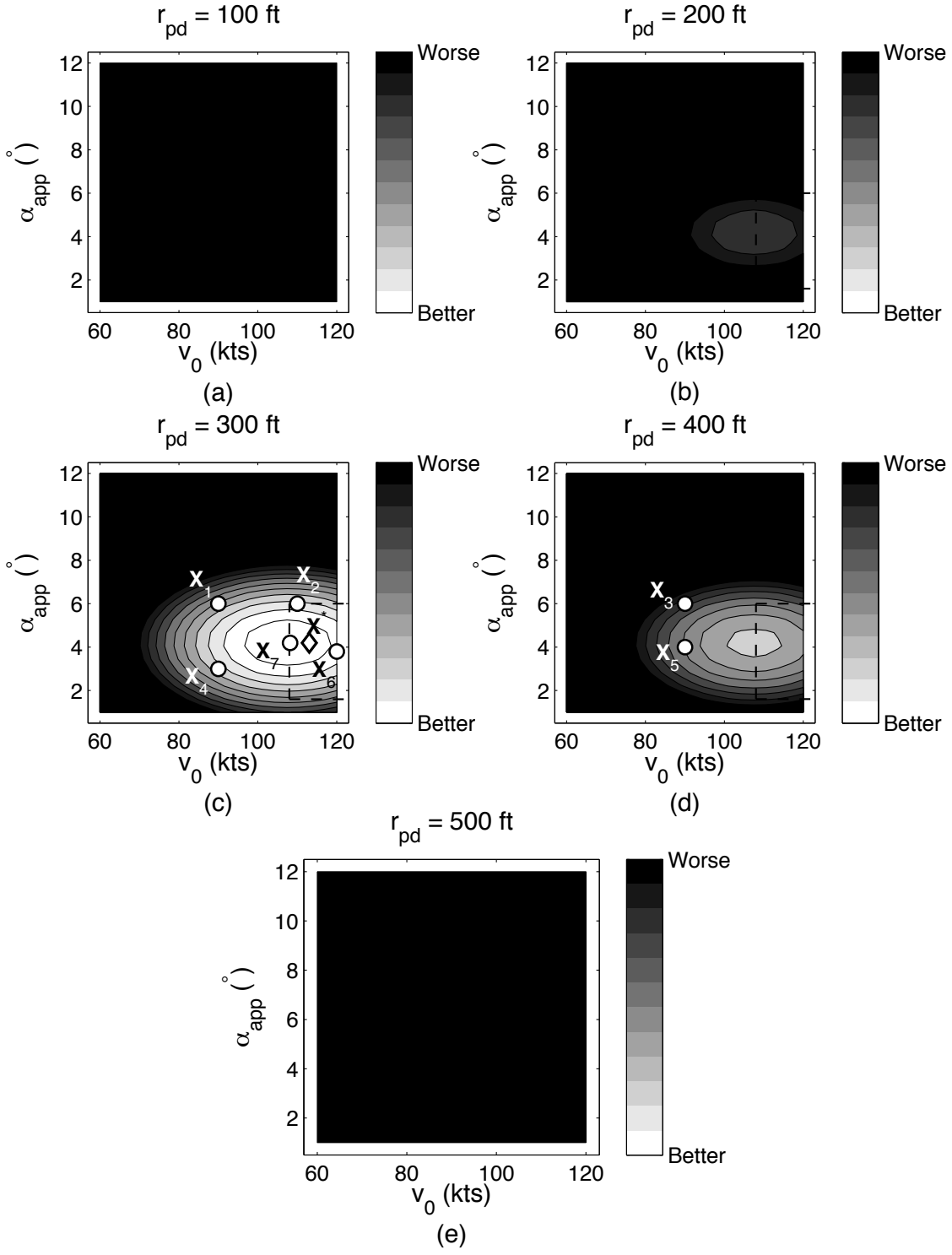

Figure 3.20: Two-dimensional contour maps through the three-dimensional approximate objective function, $B_{app}(\mathbf{X})$, for the third optimization step. Move limits are shown as dashed lines.

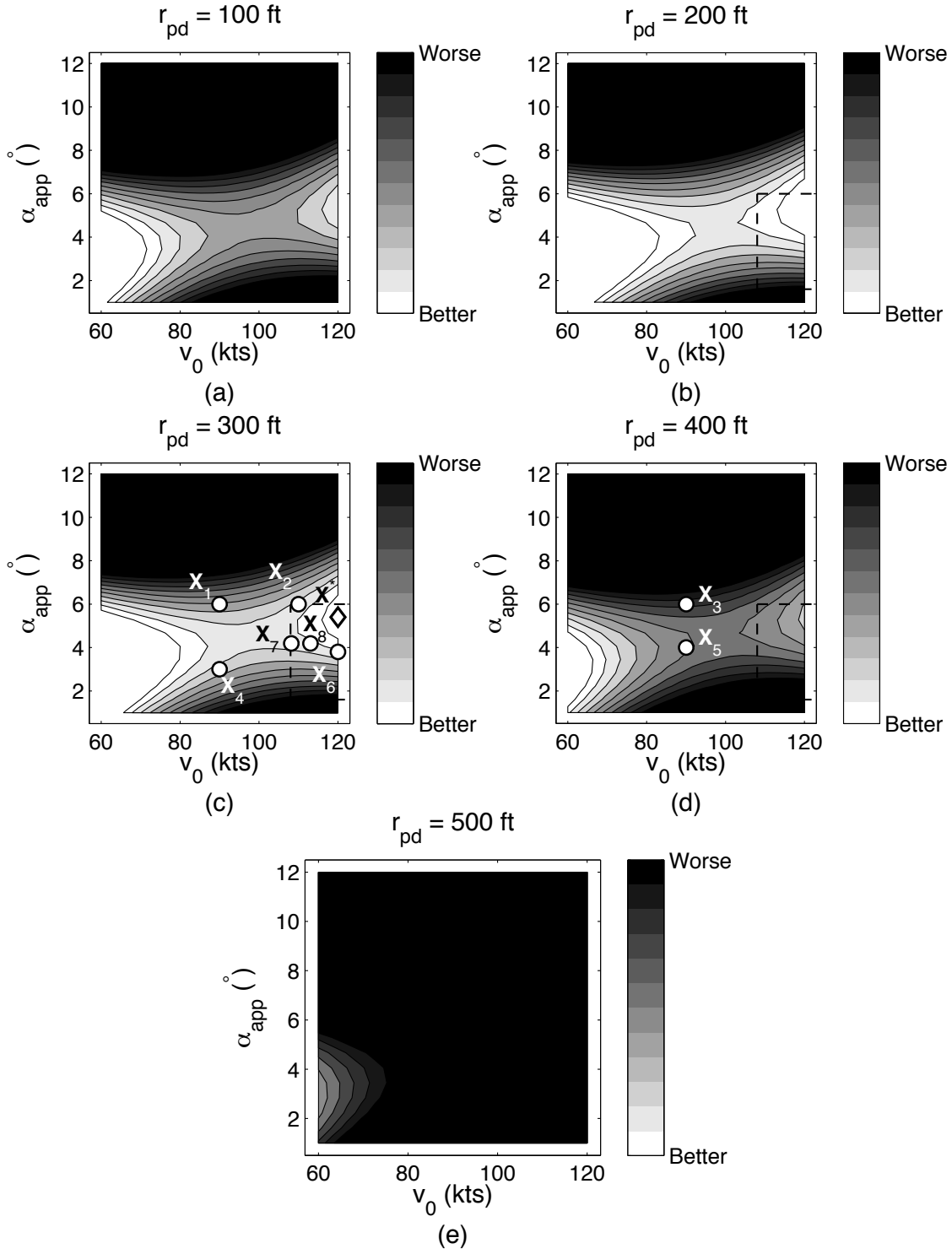

Figure 3.21: Two-dimensional contour maps through the three-dimensional approximate objective function, $B_{app}(\mathbf{X})$, for the fourth optimization step. Move limits are shown as dashed lines.

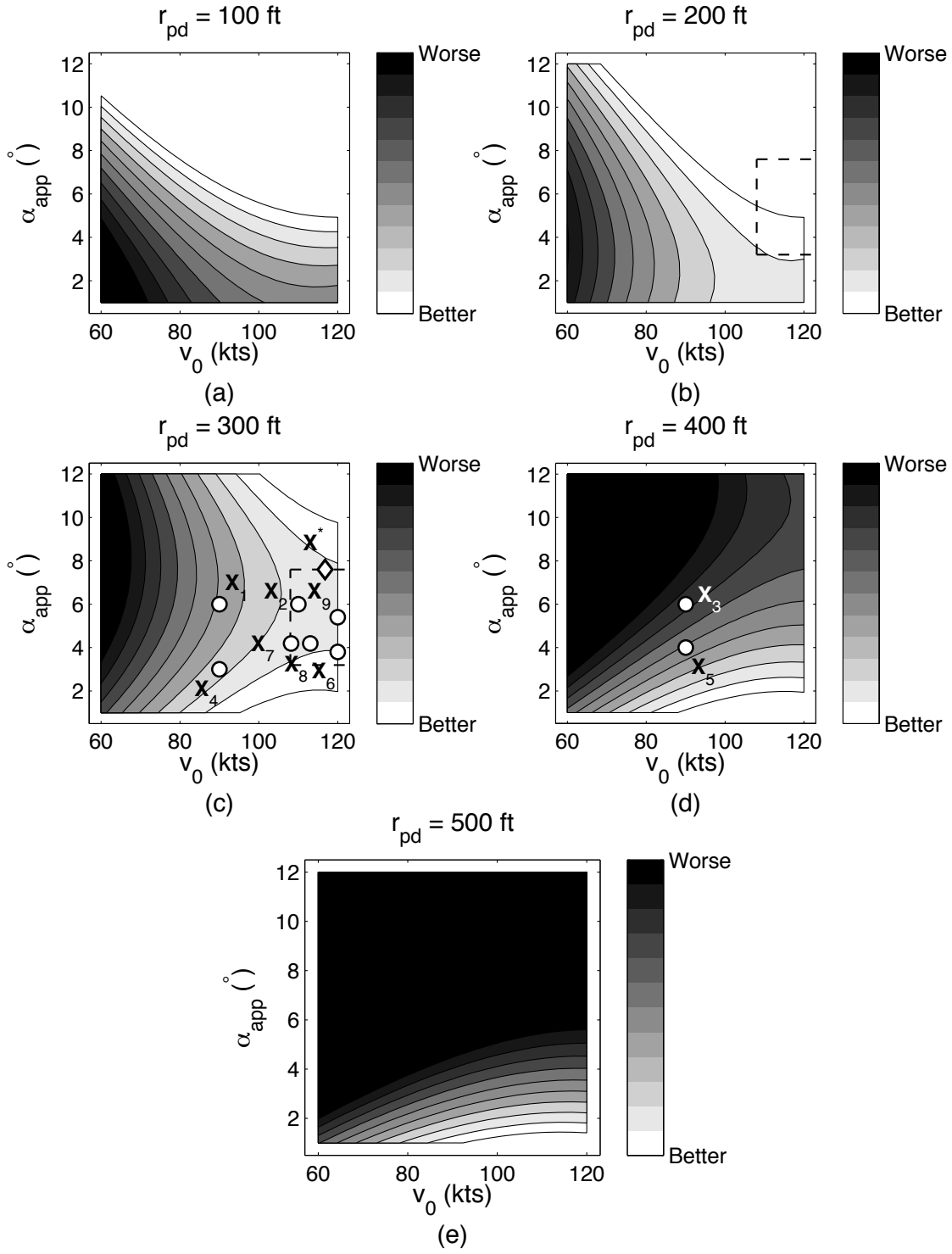

Figure 3.22: Two-dimensional contour maps through the three-dimensional approximate objective function, $B_{app}(\mathbf{X})$, for the fifth optimization step. Move limits are shown as dashed lines.

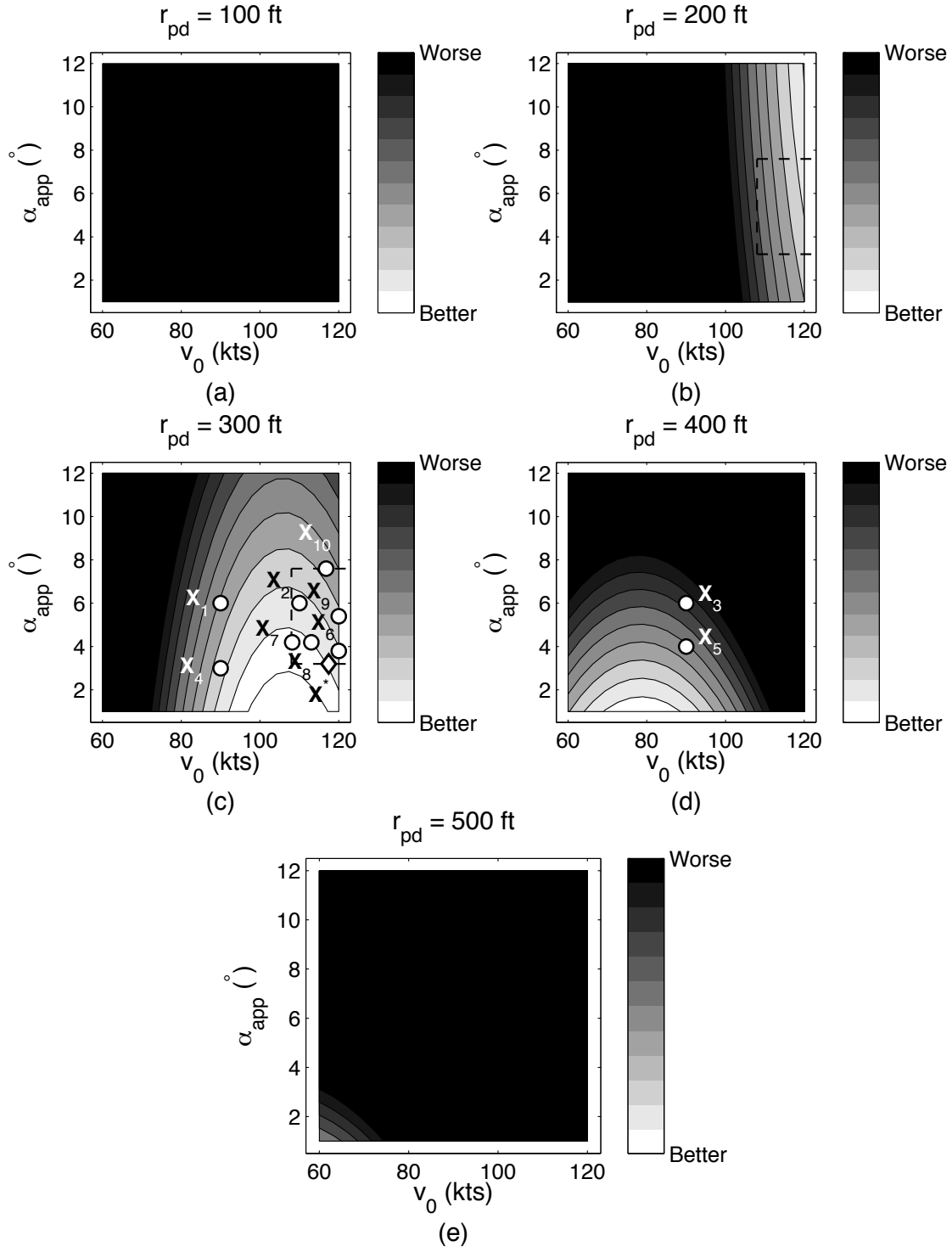

Figure 3.23: Two-dimensional contour maps through the three-dimensional approximate objective function, $B_{app}(\mathbf{X})$, for the sixth optimization step. Move limits are shown as dashed lines.

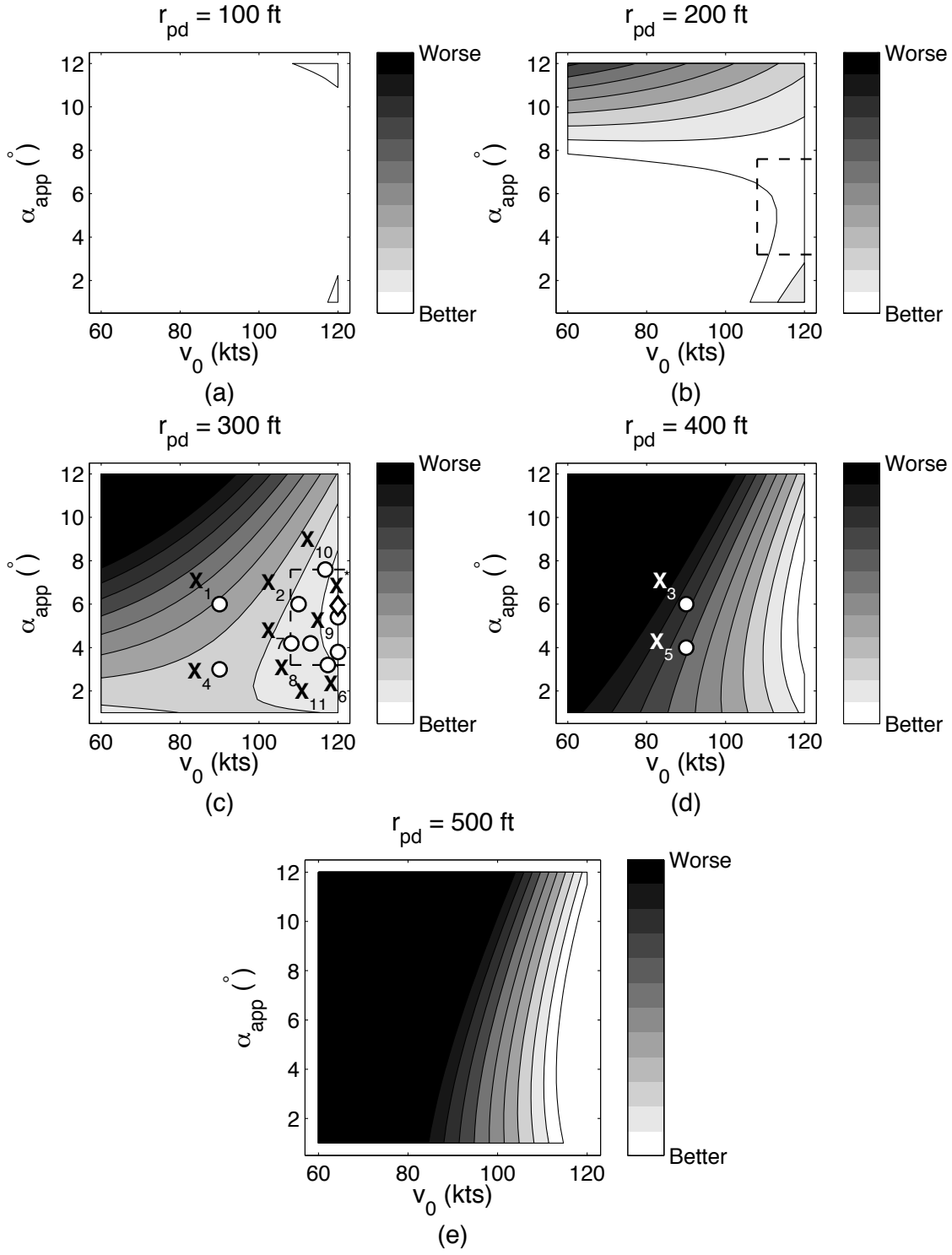

Figure 3.24: Two-dimensional contour maps through the three-dimensional approximate objective function, $B_{app}(\mathbf{X})$, for the seventh optimization step. Move limits are shown as dashed lines.

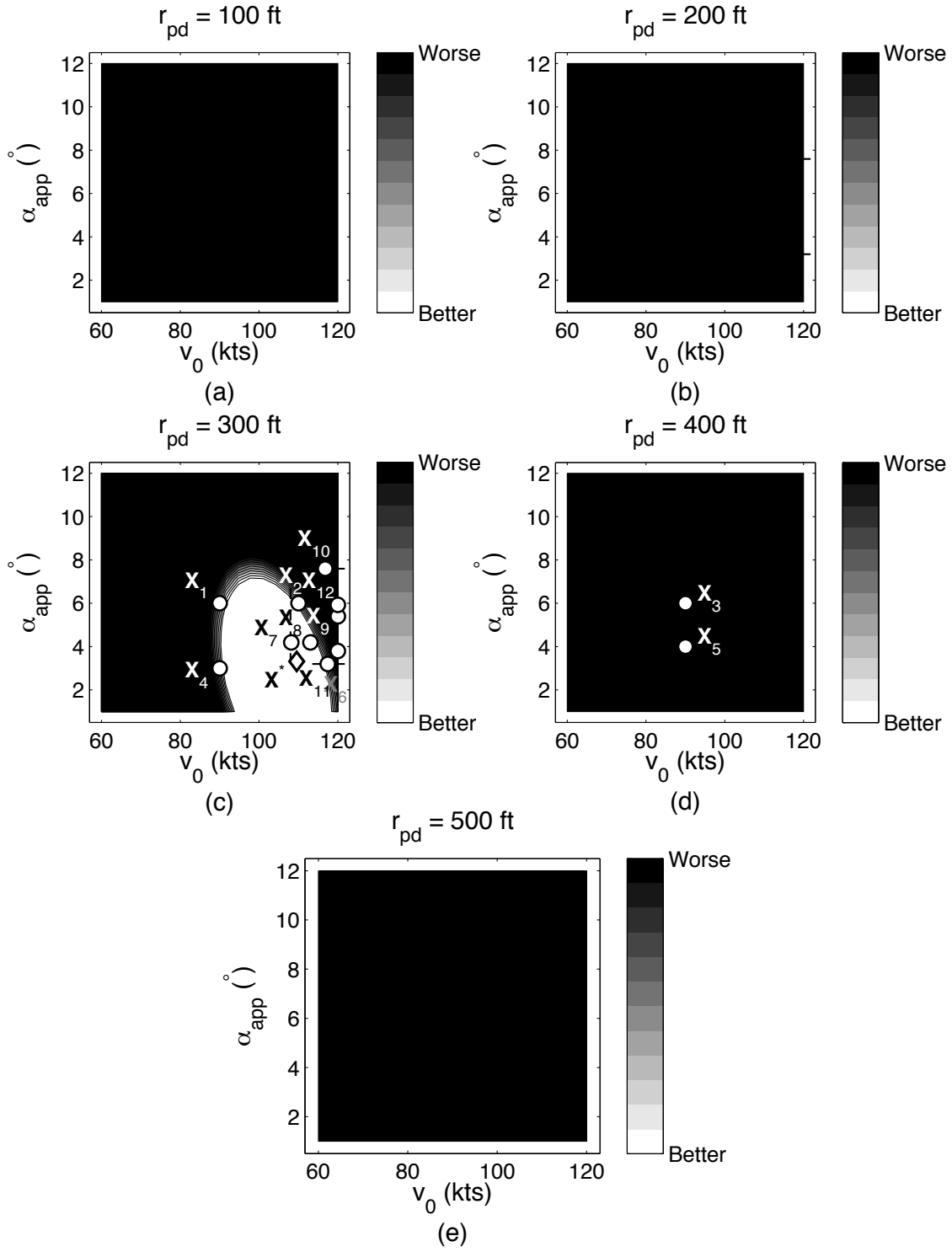

Figure 3.25: Two-dimensional contour maps through the three-dimensional approximate objective function, $B_{app}(\mathbf{X})$, for the eighth optimization step. Move limits are shown as dashed lines.

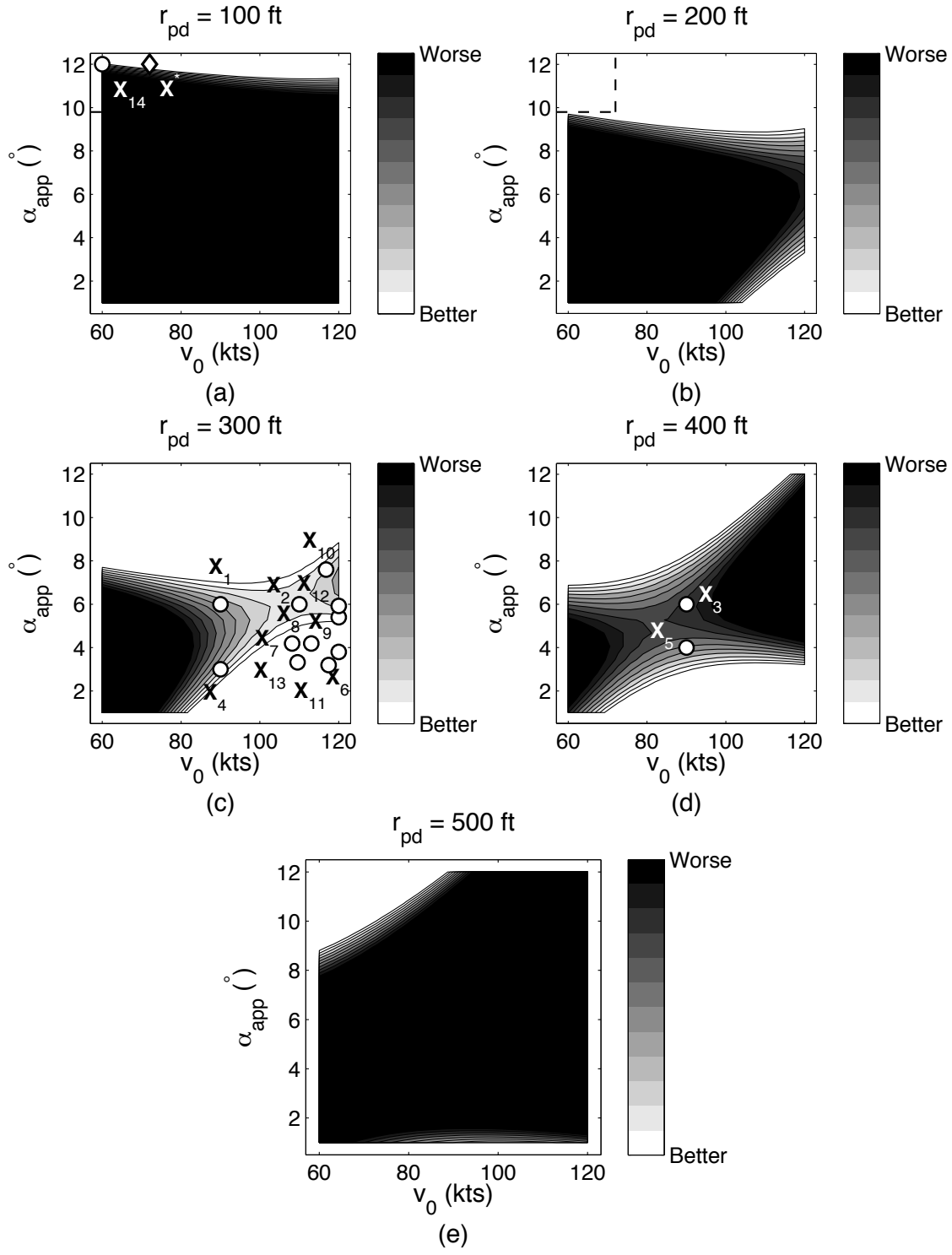

Figure 3.26: Two-dimensional contour maps through the three-dimensional approximate objective function, $B_{app}(\mathbf{X})$, for the nineth optimization step. Move limits are shown as dashed lines.

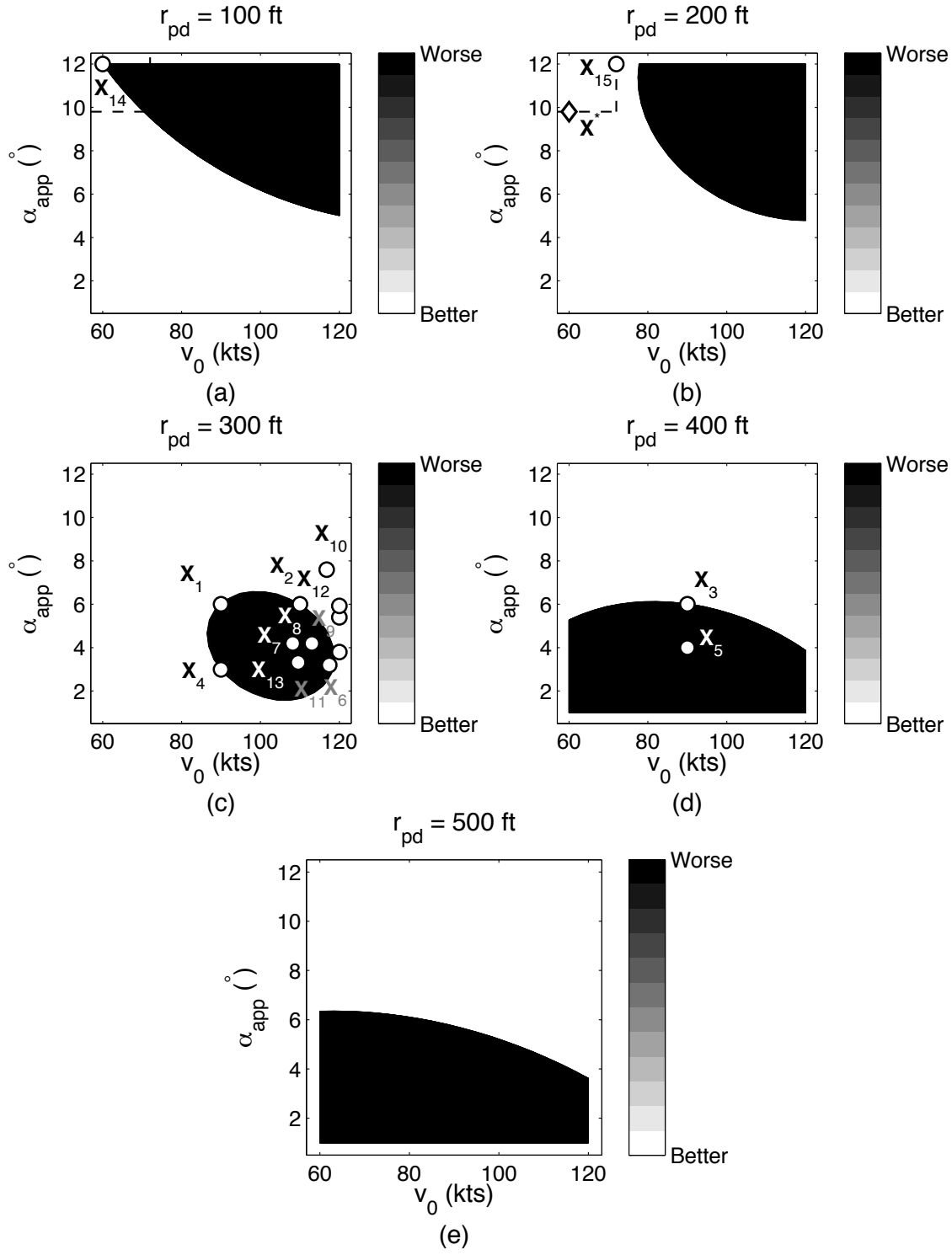

Figure 3.27: Two-dimensional contour maps through the three-dimensional approximate objective function, $B_{app}(\mathbf{X})$, for the tenth optimization step. Move limits are shown as dashed lines.

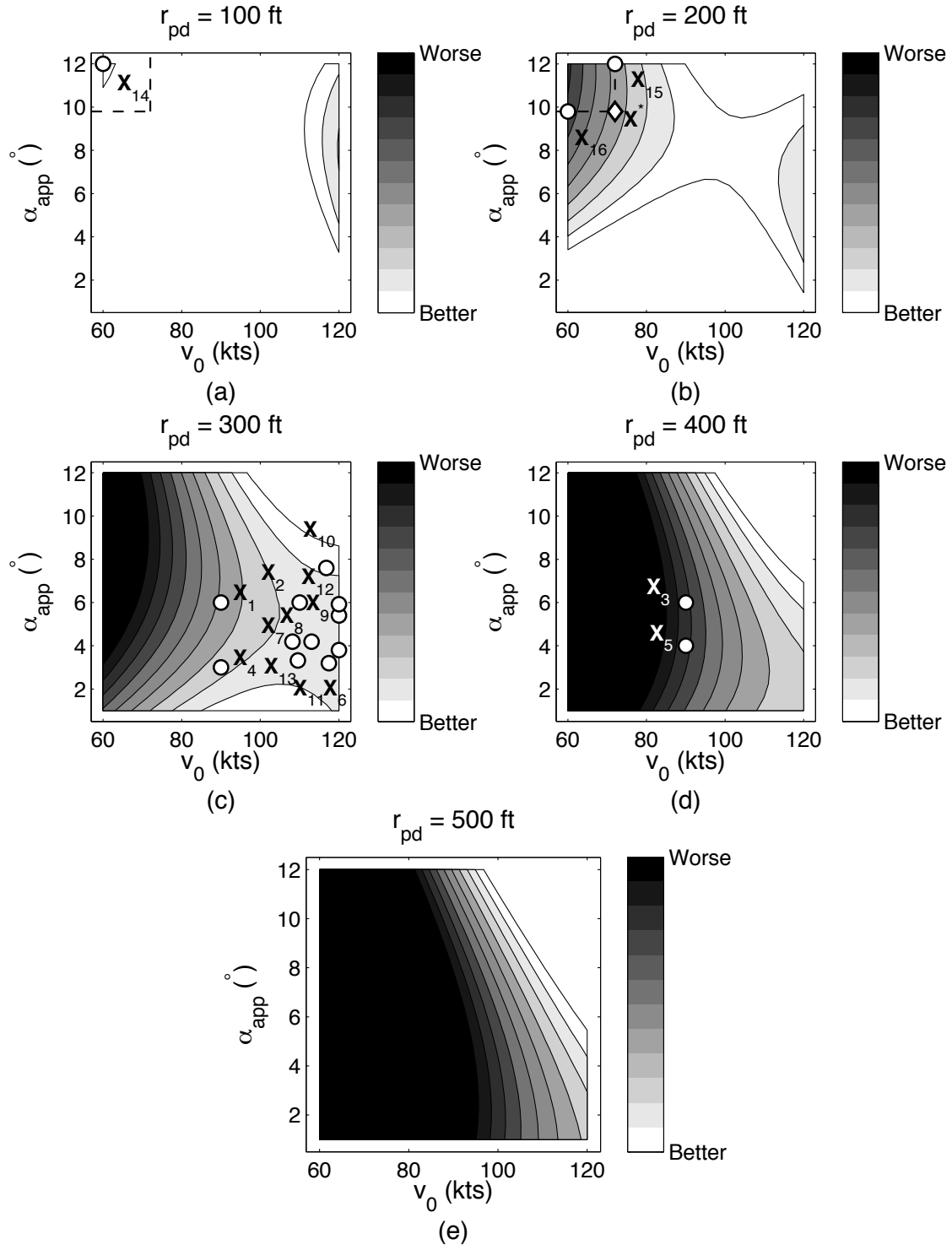

Figure 3.28: Two-dimensional contour maps through the three-dimensional approximate objective function, $B_{app}(\mathbf{X})$, for the eleventh optimization step. Move limits are shown as dashed lines.

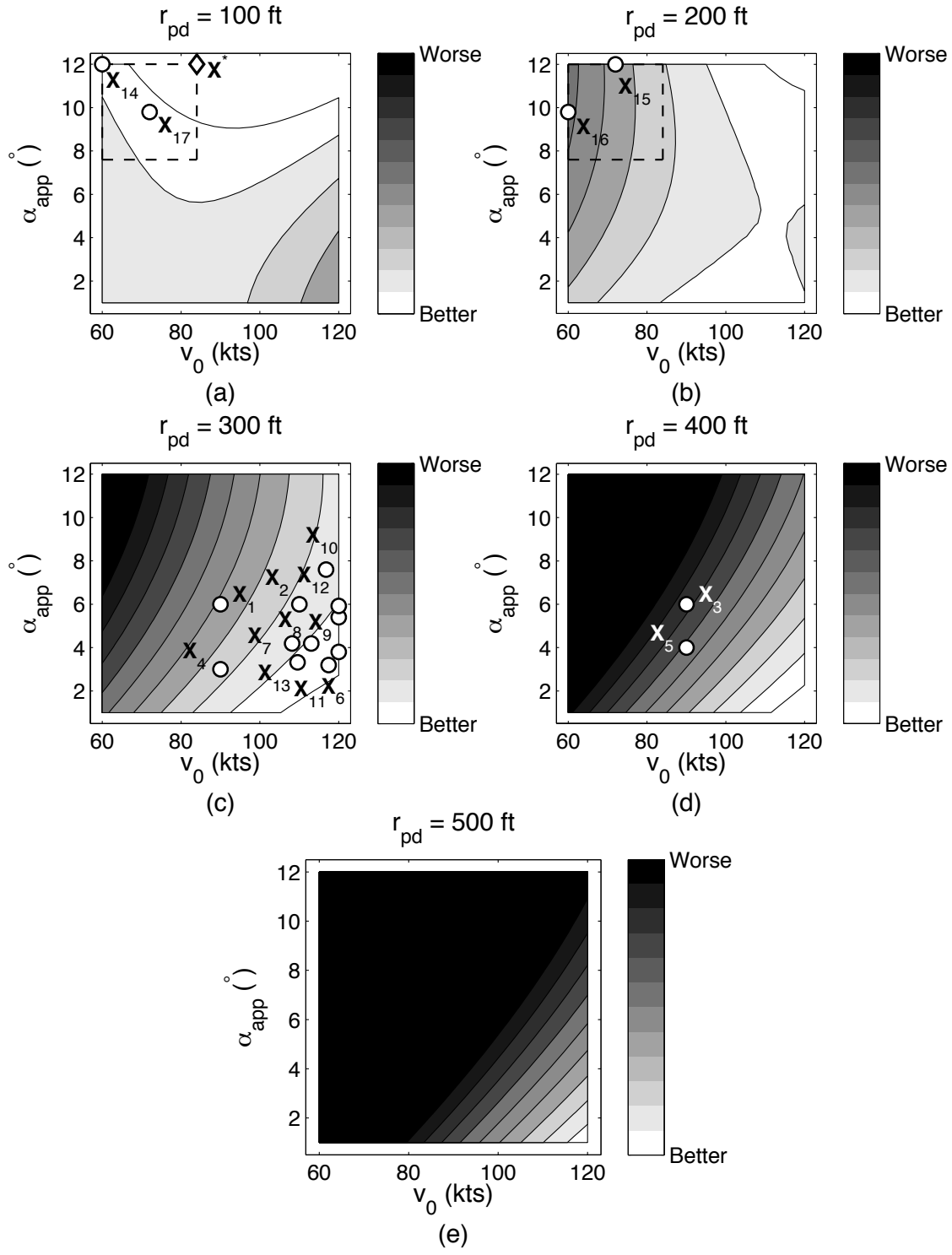

Figure 3.29: Two-dimensional contour maps through the three-dimensional approximate objective function, $B_{app}(\mathbf{X})$, for the twelfth optimization step. Move limits are shown as dashed lines.

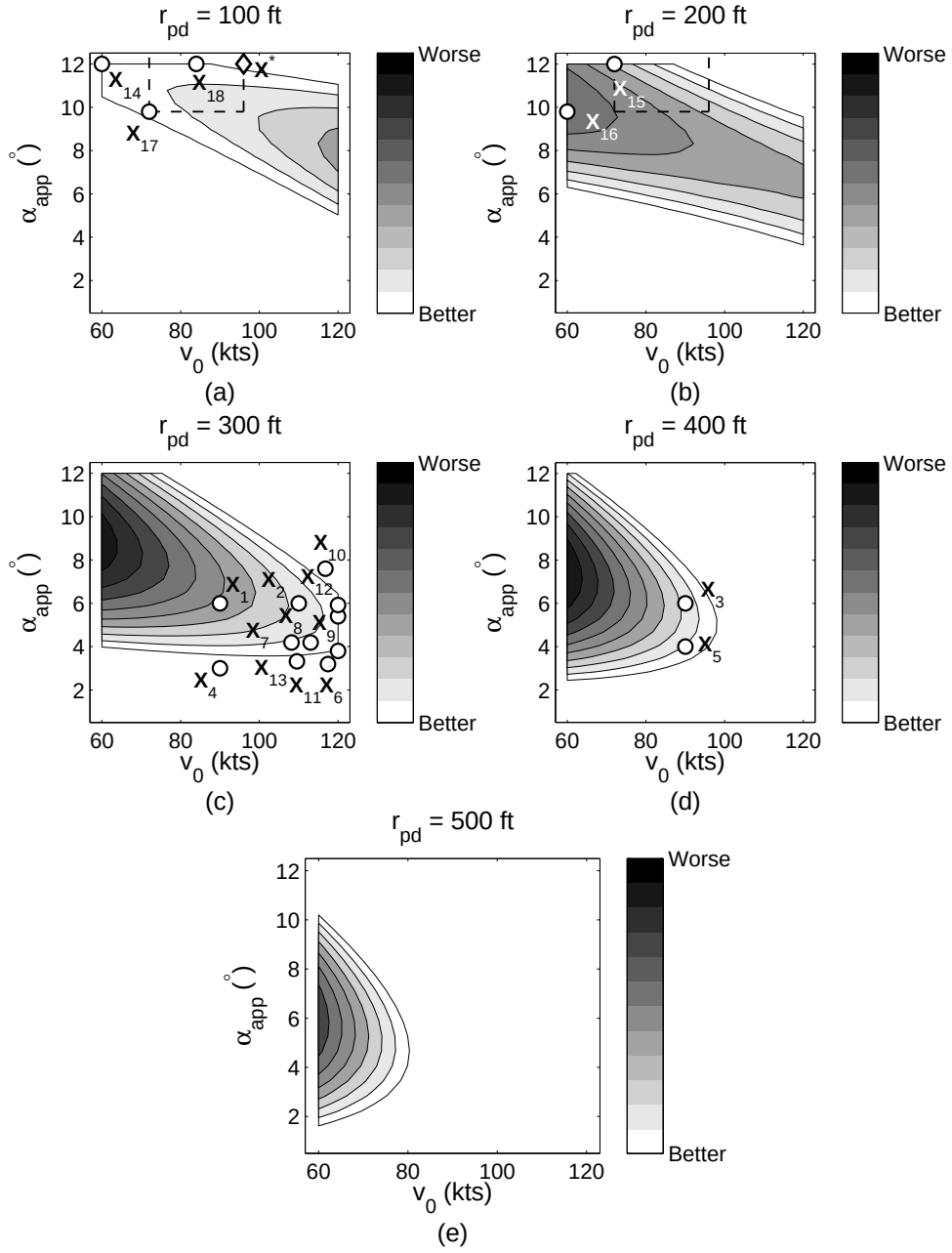

Figure 3.30: Two-dimensional contour maps through the three-dimensional approximate objective function, $B_{app}(\mathbf{X})$, for the thirteenth optimization step. Move limits are shown as dashed lines.

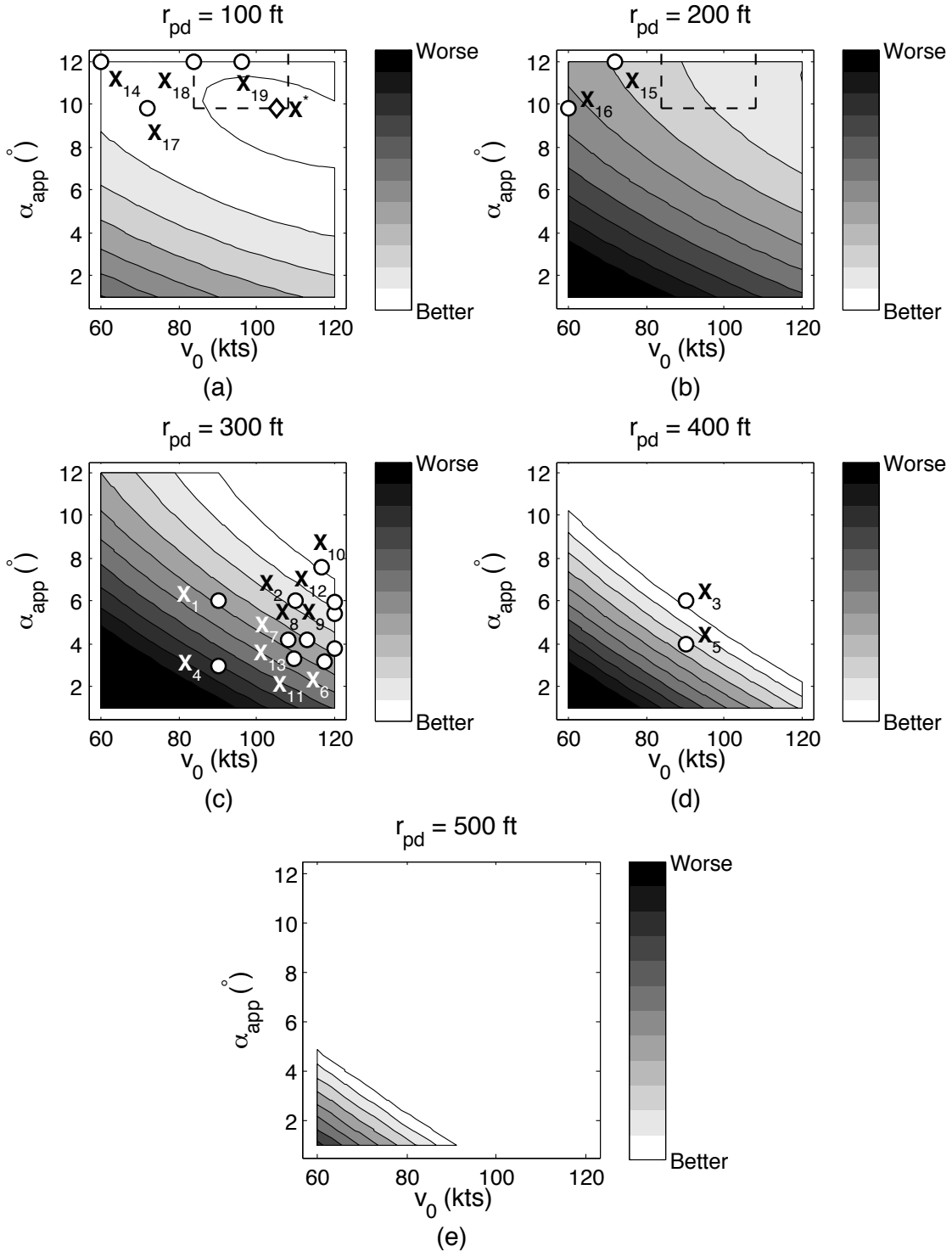

Figure 3.31: Two-dimensional contour maps through the three-dimensional approximate objective function, $B_{app}(\mathbf{X})$, for the fourteenth optimization step. Move limits are shown as dashed lines.

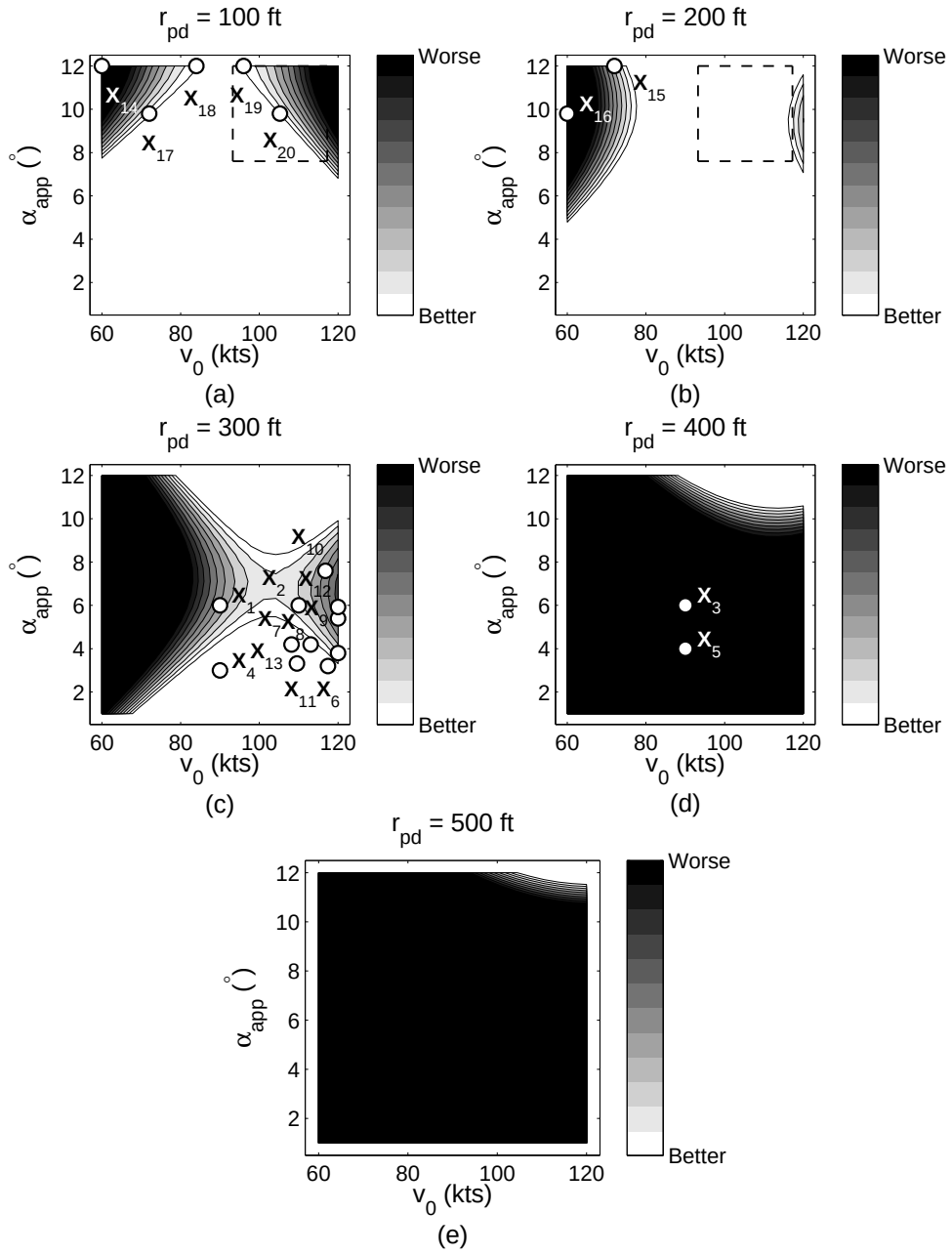

Figure 3.32: Two-dimensional contour maps through the three-dimensional approximate objective function, $B_{app}(\mathbf{X})$, for the final results. Move limits are shown as dashed lines.

tions change significantly between each optimization step. In addition, like the previous study, the two minima that were still found by the optimization scheme represent vast differences in the objective function from the baseline case. The initial progress towards a shallow local optimum at $\mathbf{X}_9 = [5.4^\circ \quad 120.0 \text{ kts} \quad 265.1 \text{ ft}]^T$ is consistent with Tritschler's initial results as well as with the traditional operational approach of "out running" the brownout cloud. The global minimum of $\mathbf{X}_{20} = [9.8^\circ \quad 105.2 \text{ kts} \quad 100.0 \text{ ft}]^T$ is also consistent with the previous optimization study in finding that a very aggressive steep approach further diminishes the objective function. It should be noted, however, that it can be seen, especially in Fig. 3.32, that the full design space has not been explored. For the present study, only two local minimums have been found, but it is possible that further minimums exist.

3.3.2 Physical Interpretation of the Results

There are many physical mechanisms at work that can determine the intensity of the brownout dust cloud. In this section, a comparison of some of the mechanisms of the baseline, local shallow minimum, and global steep minimum are presented here to explain of how changing the characteristics of the landing maneuver effects the dust cloud. Figures 3.33 and 3.34 show a comparison of some instantaneous realizations of the velocity fields and the developing cloud of the baseline approach versus the shallow and steep minima respectively. Because during each approach profile the timescale of events such as the waking impinging on the ground, recirculation

of particles, etc., an effort was made to match the events and not the time step. In addition, the dust particles have been enlarged to make the results legible.

As noted by Tritschler [2], the flow field evolves in a very specific way when it interacts with the ground. Using the baseline case (see Figs. 3.33(a)–(e)) as a reference, in the first phase seen in Fig. 3.33(a) occurs as the blade tip vortices impinge on the ground, interacting with each other, and creating a so-called ground vortex. The ground vortex forms underneath the main rotor as it hovers (Fig. 3.33(a)) and then convects up and forwards (Figs. 3.33(b)–(c)). As the ground vortex convects and restructures itself (Fig. 3.33(d)), the flow field becomes more representative of a canonical in-ground effect (IGE) flow (Fig. 3.33(e)), where the blade tip vortices convect along the slipstream boundary, impinge upon the ground, and splay outward.

A comparison between the baseline approach profile and the local (shallow) optimum approach is shown in Fig. 3.33. Figures 3.33(a)–(e) describe the baseline profile and Figs. 3.33(f)–(j) the shallow profile. The brownout onset for the shallow case is delayed about 12 seconds relative to the baseline case, suggesting that the wake is impinging on the ground at a much later time than for the baseline case. In Figs. 3.33(a) and (f), the blade tip vortices can be seen to begin to impinge on the ground. The ground vortex for the baseline case appears to be much larger, as well as to have a much larger region of circulation than that of the shallow case. In both cases, however, the ground vortex is mostly responsible for the initial uplift of the sediment particles. When the ground vortex convects forward and restructures it remains larger in the baseline case (Fig. 3.33(b)–(c)), uplifting more particles as

it convects, whereas in the shallow approach (Fig. 3.33(g)–(h) the ground vortex decreases in size and intensity and fewer particles are uplifted.

Notice also that in the baseline approach (Figs. 3.33(c)–(d)) that the ground vortex does not convect very far from underneath the rotor, creating more circulation directly under the rotor, and hence reingesting more particles through the rotor disk as a consequence. In contrast, the ground vortex obtained with the the shallow approach (Figs. 3.33(h)–(ii)) convects forwards of the rotor around 50 ft., uplifting particles farther away and fewer particles being reingested into the rotor disk. As the flow field evolves to a more representative IGE flow, the dust particles in the baseline case (Fig. 3.33(e)) are uplifted and reingested through the rotor, while in the shallow optimum case (Fig. 3.33(j)) the uplifted particles are much farther from the rotor and are less likely to be recirculated. Overall, for the more shallow approach the particles are uplifted farther from the rotor, creating a "better", i.e. a less intense dust cloud, landing environment.

The results of the baseline approach versus the global (steep) optimum approach shown in Fig. 3.34, with the baseline approach being defined in Figs. 3.34(a)–(e) and the steep approach defined Figs. 3.34(f)–(j), and the results are very similar to those Fig. 3.33. The brownout onset of steep approach has close to a 20 second delay from the onset seen in the baseline case. In Fig. 3.34(f), the blade tip vortices do not interact much with each other and, therefore, the ground vortex is much smaller and of lesser intensity than the baseline case (Fig. 3.34(a)). This outcome results in the uplift of fewer particles. Once again, the ground vortex convects farther forward from the rotor (Figs. 3.34(g)-(i)) for the steep approach, uplifting particles about

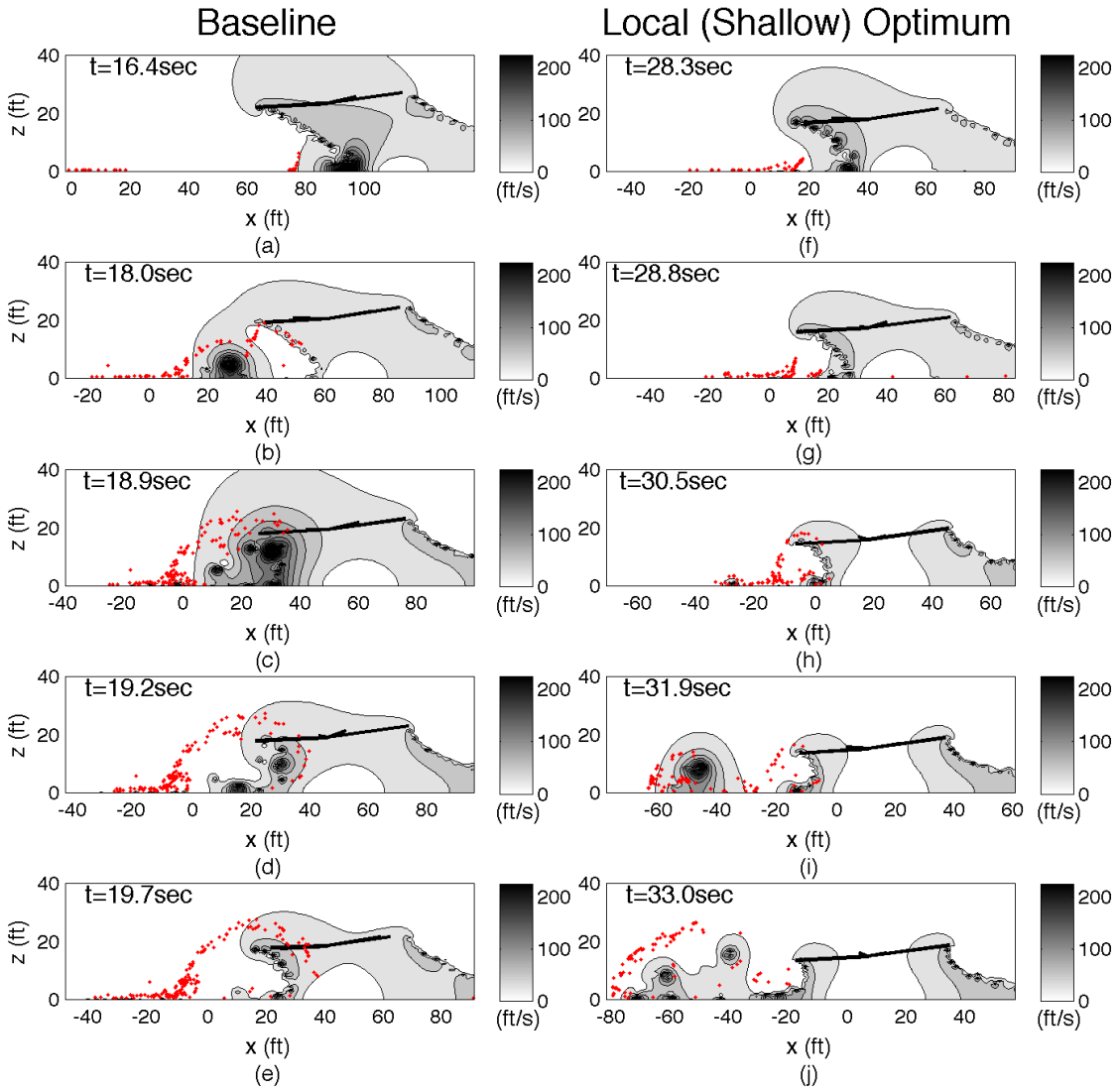

Figure 3.33: Realizations of the velocity magnitudes and developing cloud in a longitudinal plane through the flow field for (a)–(e) the baseline, $\mathbf{X}_1$, and (f)–(j) the local (shallow) optimum, $\mathbf{X}_9$, approach profiles. The motion of the rotor over the ground is from right to left. Particles are enlarged for illustrative purposes.

60 ft. forward of the rotor. In this case, there is very little reingestion compared to the baseline case, and this produces a much less intense dust cloud.

These comparisons of both the steep and shallow optima prove that the characteristics of the dust cloud can be dramatically changed based on the type of approach profile. For the standard (typical) baseline landing, the ground vortex lingers underneath the rotor, uplifting particles that are then reingested into the rotor flow. Additionally, the tip vortices impinge on the ground much earlier in the landing, producing a longer period of time for the sediment particles to be mobilized and uplifted during the maneuver. The more aggressive flight profiles such as the shallow and steep approaches, take advantage of the outcome that tip vortices impinge on the ground much later than the baseline case. Furthermore, the ground vortices found with these profiles appear to be smaller and convect farther away from the rotor, uplifting fewer particles and producing less reingestion.

To compare the quantity of particles that are uplifted in the flow field, the dust cloud geometries in the $X - Z$ plane and the $Y - X$ plane are shown in Figs. 3.35–3.38. These figures detail the resulting clouds at the last time step of the simulation. The position of the rotor blades have also been plotted to reference the location of the helicopter with respect to the cloud. Like earlier figure, the dust particles have been enlarged for clarity.

The longitudinal versus vertical plane dust cloud geometries, in addition to the lateral versus longitudinal cloud geometries for both the baseline approach and the shallow optimum approach are shown in Figs. 3.35 and 3.36, respectively. The baseline dust cloud (Fig. 3.35(a)) can be seen to be extremely dense in the region

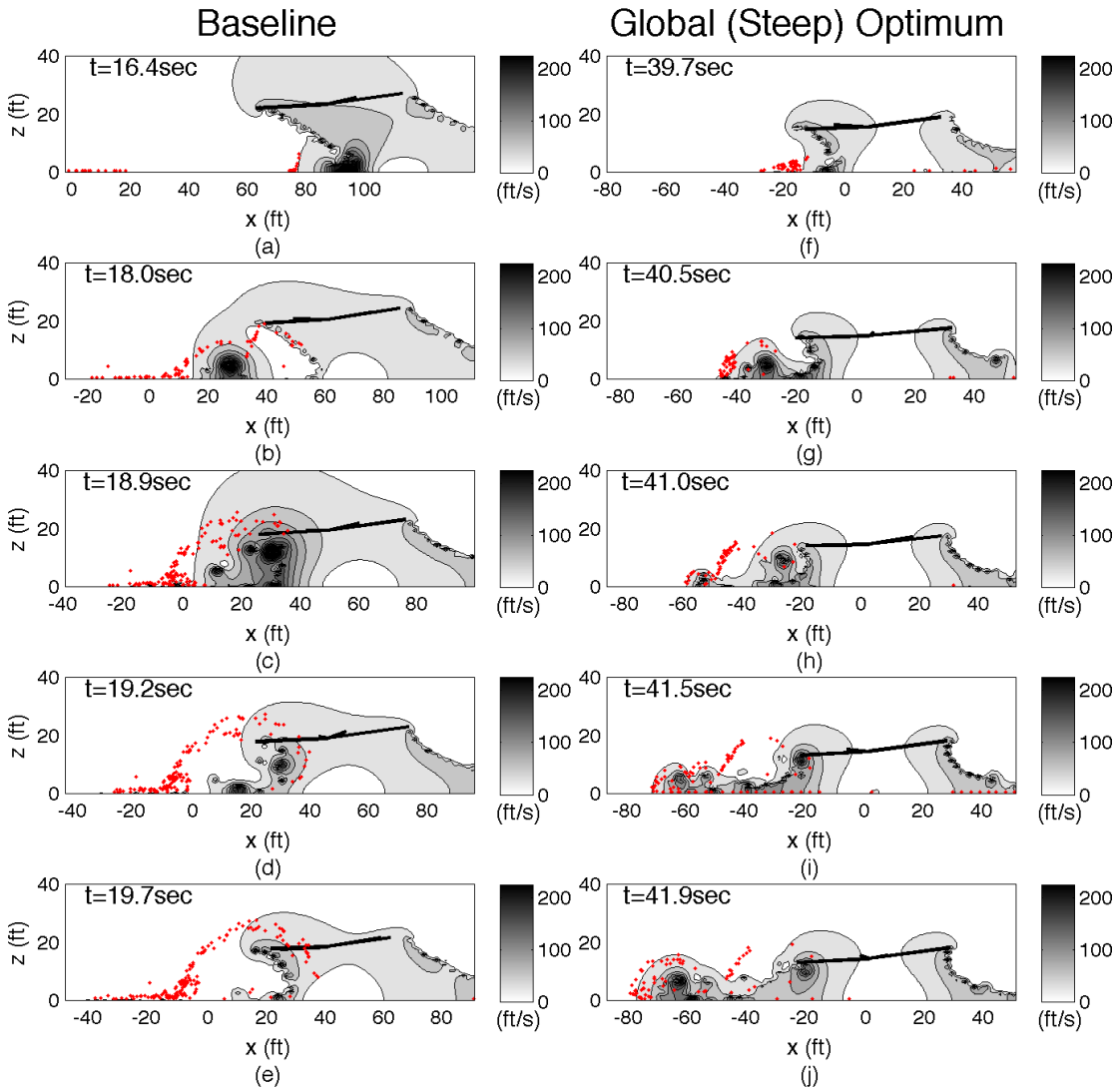

Figure 3.34: Realizations of the velocity magnitudes and developing cloud in a longitudinal plane through the flow field for (a)–(e) the baseline, $\mathbf{X}_1$, and (f)–(j) the global (steep) optimum, $\mathbf{X}_{20}$, approach profiles. The motion of the rotor over the ground is from right to left. Particles are enlarged for illustrative purposes.

directly surrounding the rotor, and up to 50 ft in front of the rotor. This cloud shows a typical brownout cloud behavior, where there is a less dense outer region of particles that have been initially uplifted by the ground vortex as it was convected away from from the rotor, and also an inner region closer to the rotor where dust particles are being uplifted, reingested by the rotor, and bombarded back onto the bed. The cloud that results from the shallow approach profile (Fig. 3.35(b)) gives a slightly less dense distribution of uplifted particles. While the shape of the cloud is fairly similar to that of the baseline case, the fewer uplifted particles is because of the wake impinges on the ground at a later time, and so fewer particles uplifted.

A top view of the predicted clouds (Fig. 3.36) more clearly shows the difference in the cloud densities. Notice that helicopter landing is proceeding from the bottom to the top of the window. The baseline approach (Fig. 3.35(a)) is much more densely packed, especially in the region of the cloud surrounding the rotor. Furthermore, notice that there are fewer particles that are produced by the shallow approach profile (Fig. 3.36(b), and a less dense region around the rotor. Also visible are the "ring" like structures that form as the ground vortices mobilize and uplift particles as they convect outwards from the rotor, also convecting those particles outwards.

The cloud produced by the steep optimum approach profile develops in a similar fashion to that for the shallow approach, but with more dramatic results (Fig. 3.37). From the longitudinal view (Fig. 3.37(b)) the dust cloud can be seen to be much less dense and uniformly distributed than the cloud produced by the baseline case. In addition to there being fewer dust particles in the steep approach case, the particles are also not uplifted as high or as far from the rotor. The dramatic

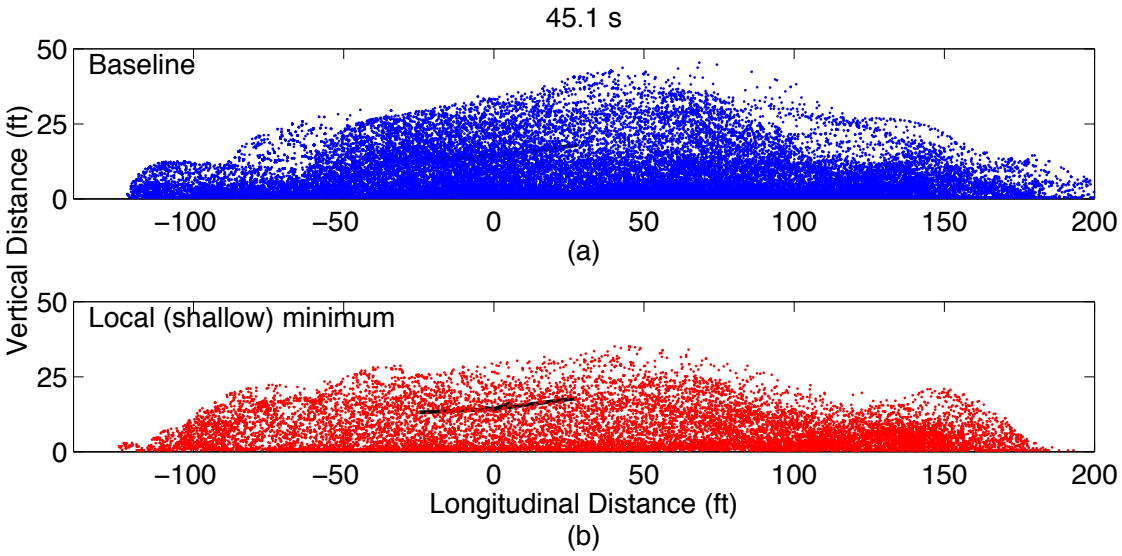

Figure 3.35: Dust cloud geometries side view for (a) the baseline approach profile and (b) the shallow optimum approach.

decrease in particles from the baseline approach can be further seen in Fig. 3.38. In the region directly surrounding the rotor there are very few particles. In fact, there is nearly a whole ring of empty space surrounding the rotor that is unpopulated by particles. This type of cloud development is indicative that there is little particle reingestion taking place during the steep optimum approach profile, and much of the dust cloud results from the initial ground vortex uplifting particles further away from the rotor.

3.3.3 Comparison to the Previous Study

The previous flight path optimization by Tritschler [2] presented a framework in which to conduct a brownout mitigation study. Tritschler's study found that the optimization design space is non-convex and there is a possibility for several local minima. Specifically, a shallow local optima was found at $\mathbf{X}_1$ =

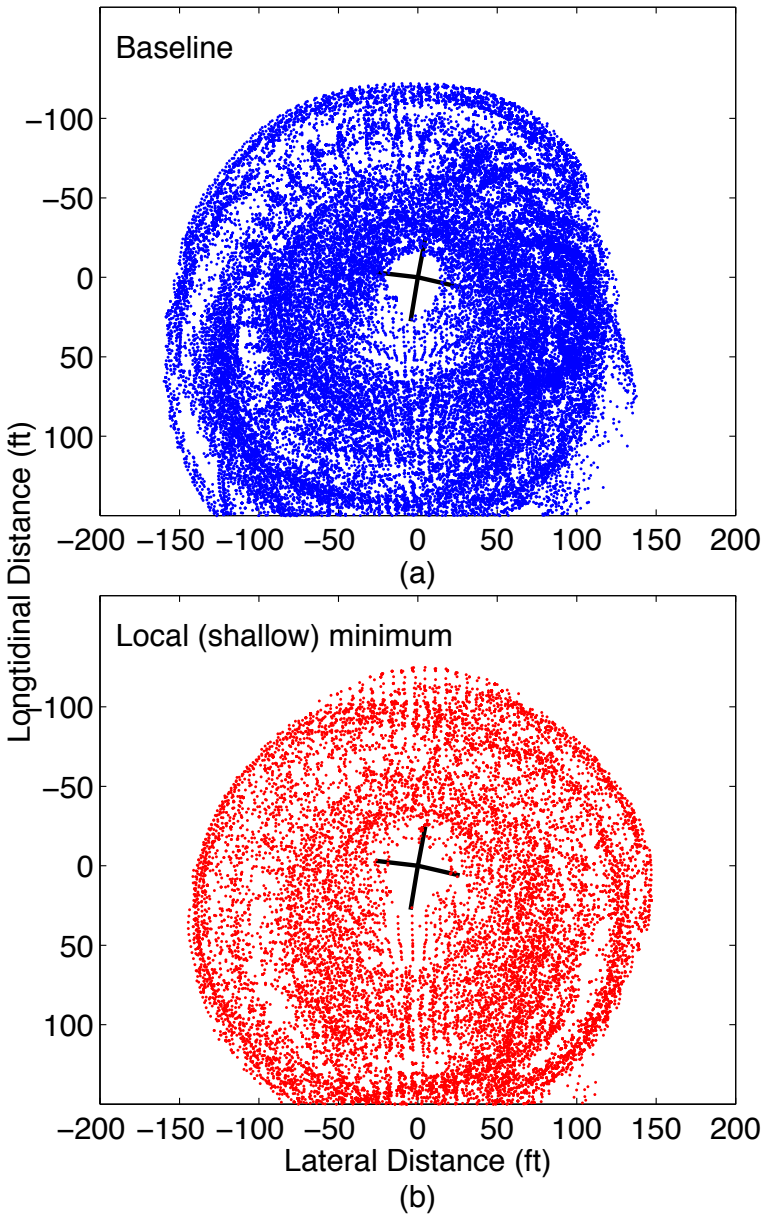

Figure 3.36: Dust cloud geometries top view for (a) the baseline approach profile and (b) the shallow optimum approach.

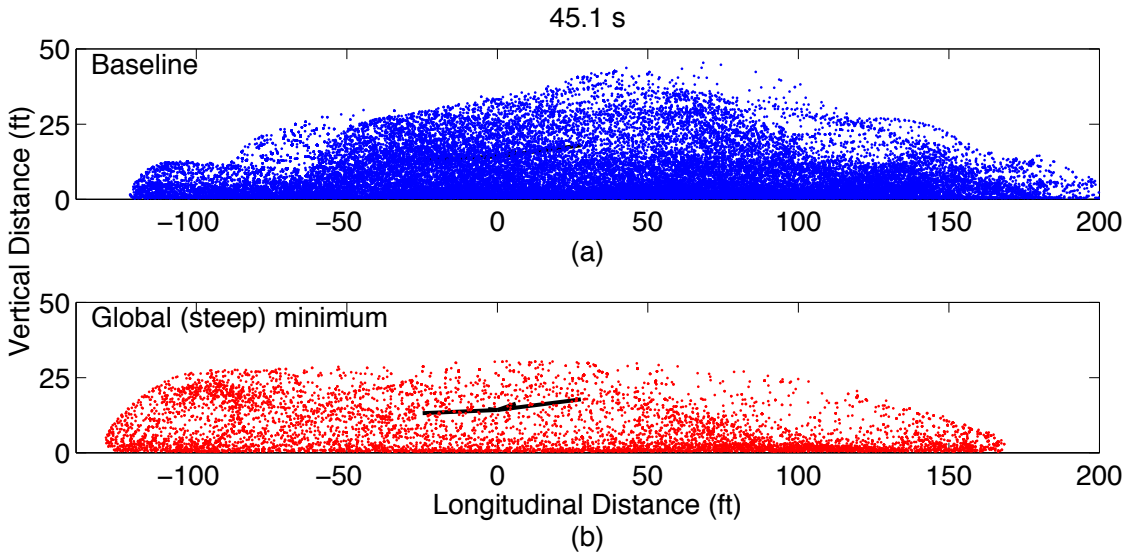

Figure 3.37: Dust cloud geometries side view for (a) the baseline approach profile and (b) the shallow optimum approach.

$[1.0^\circ \;\; 81.5 \text{ kts} \;\; 170.0 \text{ ft}]^T$ which mirrored the operational method of "out running" the brownout cloud. On further investigation, a global minimum with a very aggressive, steep approach angle was found to be reached at $\mathbf{X}_1 = [10.4^\circ \;\; 91.0 \text{ kts} \;\; 100.0 \text{ ft}]^T$. Both optima tended to reduce the amount of time that the helicopter spent in the brownout condition, and therefore delayed the time at which the blade tip vortices impinged on the ground. These results have shown that by changing the approach profile, and hence the flow field at the ground, the characteristics of the brownout cloud can indeed be significantly changed.

The results of the current study also point to a non-convex design space with a local minimum at a shallow approach angle at $\mathbf{X}_9 = [5.4^\circ \;\; 120.0 \text{ kts} \;\; 265.1 \text{ ft}]^T$ and a global minimum at a steep approach angle at $\mathbf{X}_{20} = [9.8^\circ \;\; 105.2 \text{ kts} \;\; 100.0 \text{ ft}]^T$. While the shallow approach was not quite as shallow an angle, the nature of the both the local and global optimum approaches is similar to the previous study.

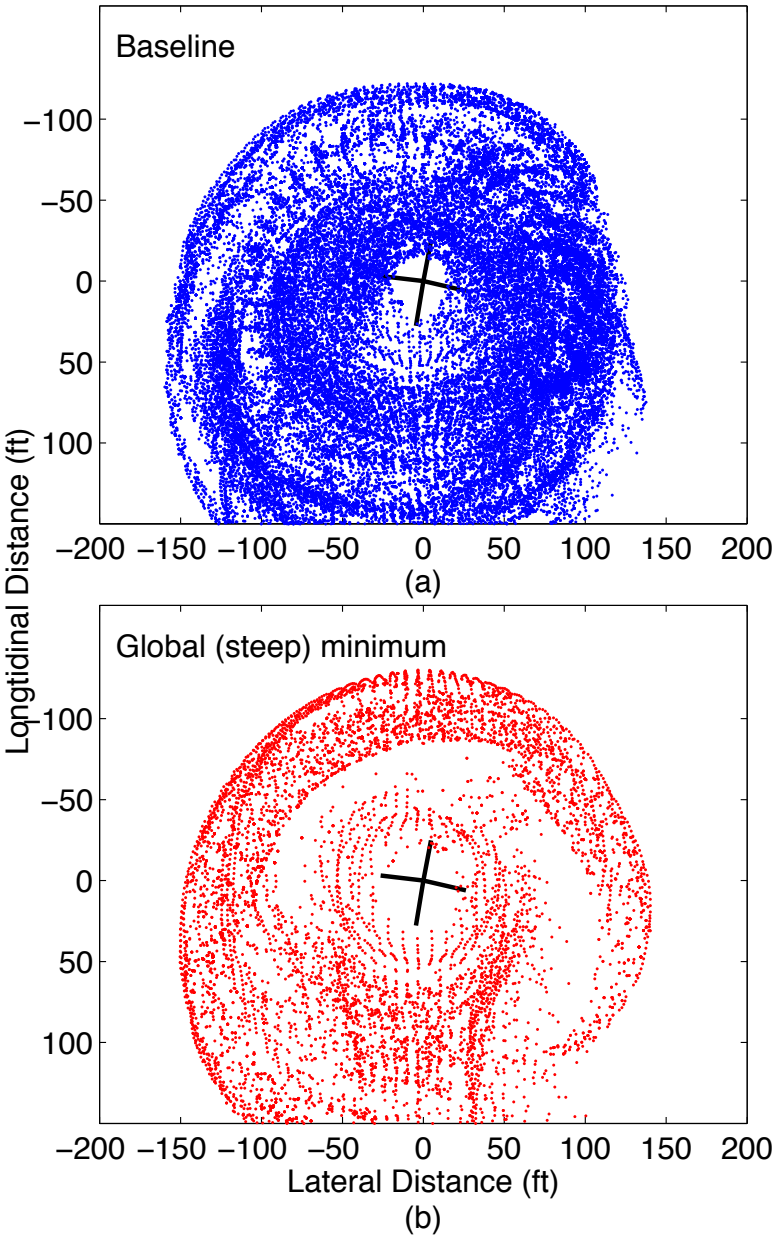

Figure 3.38: Dust cloud geometries top view for (a) the baseline approach profile and (b) the shallow optimum approach.

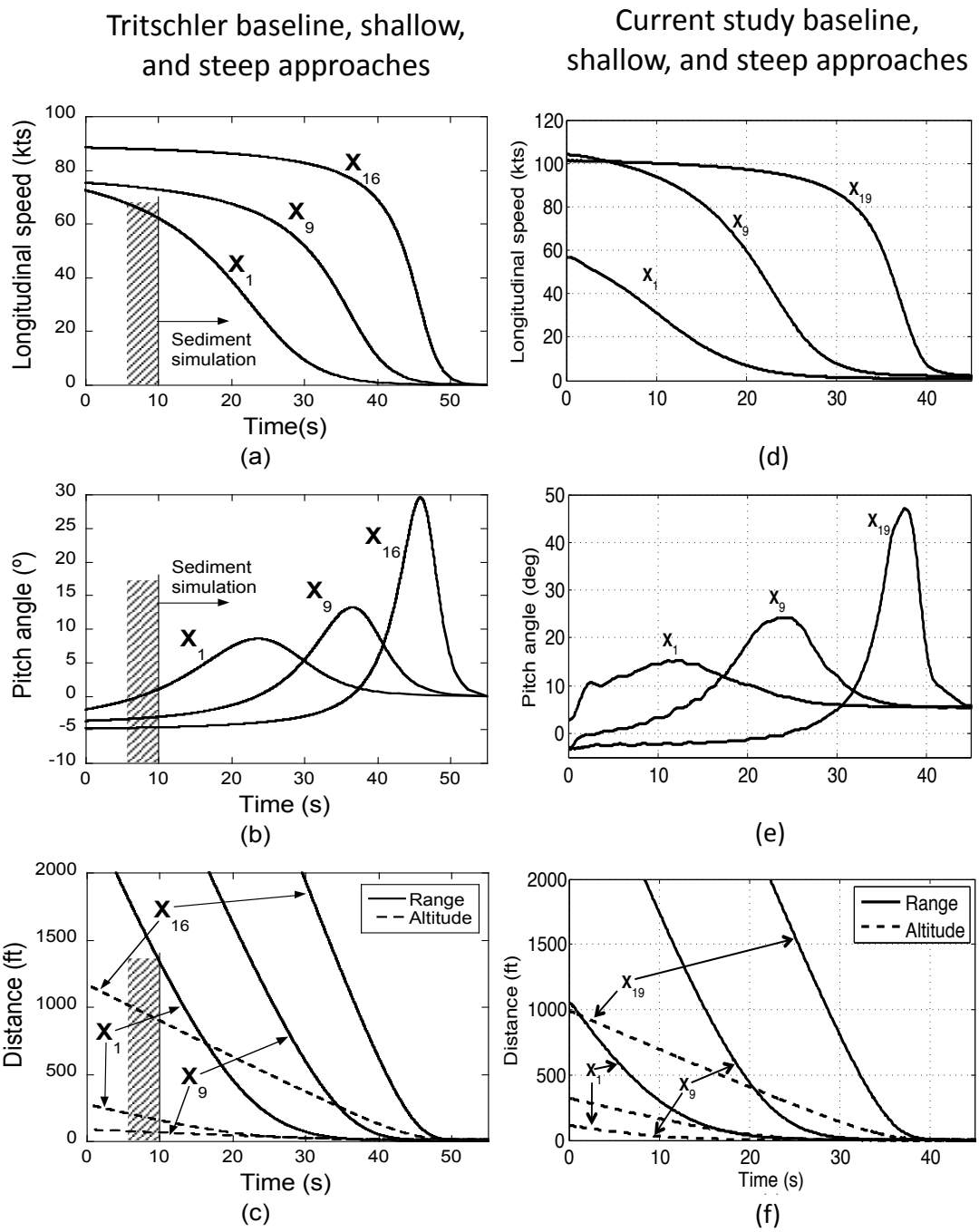

Figure 3.39: Velocity, pitch, range and altitude profiles comparison of (a)–(c) Tritschler [2] study and the (d)–(f) current study.

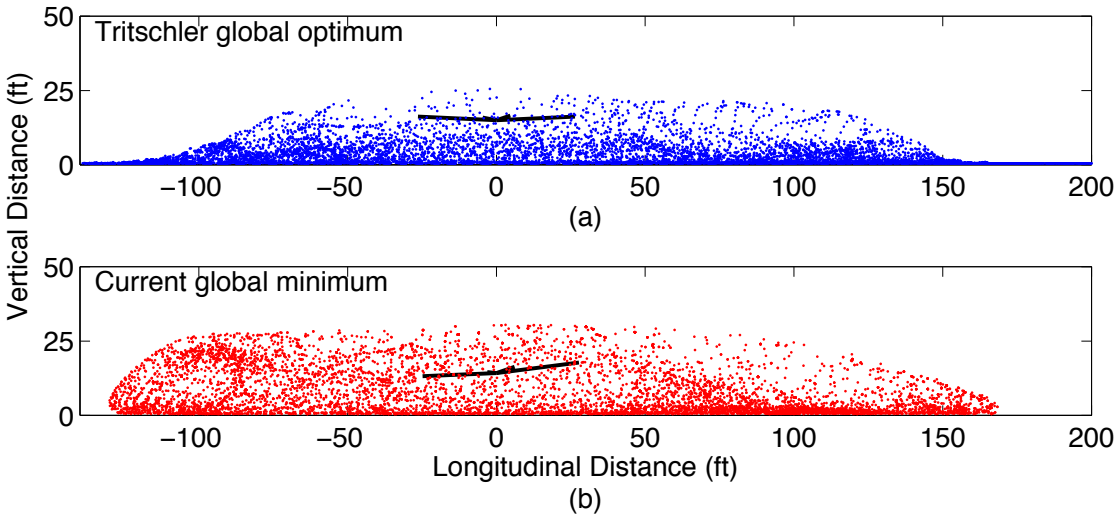

Figure 3.40: Dust cloud geometries side view for the (a) Tritschler global optimum approach [2] and (b) the current study global optimum approach.

A comparison of the Tritschler profiles with those from the current study profiles is presented in Fig. 3.39. Notice that the initial longitudinal velocities for the two optimum cases found in the current study (Fig. 3.39(d)) are higher than those found in Tritschler's study. However, the approaches in the current study are similar in that they minimize the time the helicopter spends in brownout conditions, by landing much later than in the baseline case. In Fig. 3.39(e) the fuselage pitch angle appears to oscillate because the rotor disk plane was no longer prescribed, as it was in the Tritschler study, but moves in the way that the physics of the full helicopter model require. This oscillation is a consequence of the controller process. The maximum fuselage pitch angle during the steep approach optimum in the current study is also much larger than in Tritschler's study, and will be discussed in more detail later in this section.

Because the global steep optimum for both the Tritschler study and the current study are in very similar regions of the design space, comparisons of their resulting

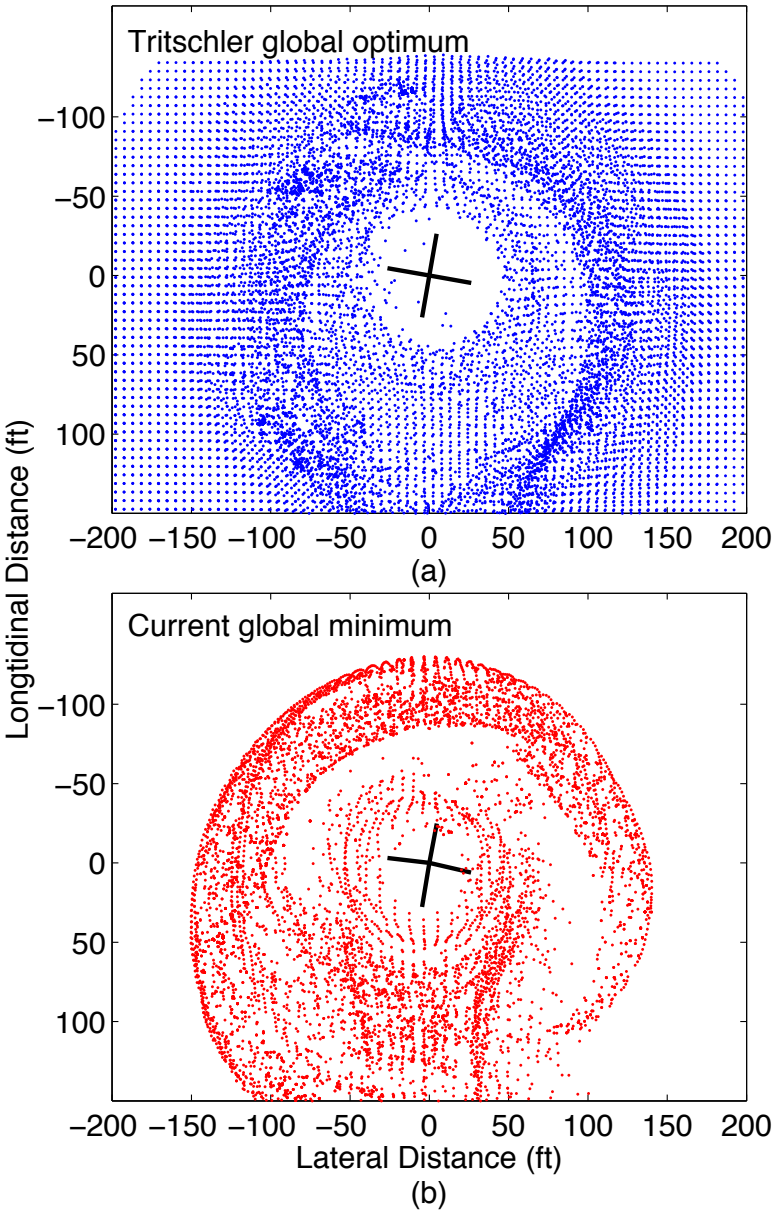

Figure 3.41: Dust cloud geometries top view for the (a) Tritschler global optimum approach [2] and (b) the current study global optimum approach.

dust clouds and flow fields are presented in Figs. 3.40–3.43. Views of the side and top cloud geometries indicate a similar structure between the two global optimum cases. In the side view (Fig. 3.40), it is interesting to note that the particles seem to be convected higher above the rotor with the current optimum (Fig. 3.40(b)), which in turn tends to produce more particle reingestion through the rotor. Both global optima show similar cloud density and quantity of particles uplifted when observed from the top (Fig. 3.41). Even though a larger particle bed was used for the Tritschler simulation, the radii from the rotor that the particles tend to cluster in, is certainly similar for both studies.

It should be noted that while the same number of particles were used for each simulation, a smaller bed size geometrically was used in the current study. Both simulations included particles counts of 100 particles in both the x and y directions in 17 layers. In the Tritschler study, the particles were then layed into a 20 ft by 20 ft bed, whereas in the current study the particles were layed into a 15 ft by 24 ft bed. A different bed geometry was chosen for the current study to accomadate the less symmetric nature of the wake that was being produced by the flight dynamics model. A comparison of the number of particles entrained during each simulation is shown in Fig. 3.42. Note that the time scales of the simulations are slightly different due to the time in the Tritschler simulation that is dedicated to achieving a steady state flight condition. Additionally, as the particle counts were the same, the actual quantity of particles is plotted, and not a normalized quantity.

The total number of particles for each simulation is shown in Fig. 3.42(a); interestingly, it can be seen that about seven times the amount of particles are

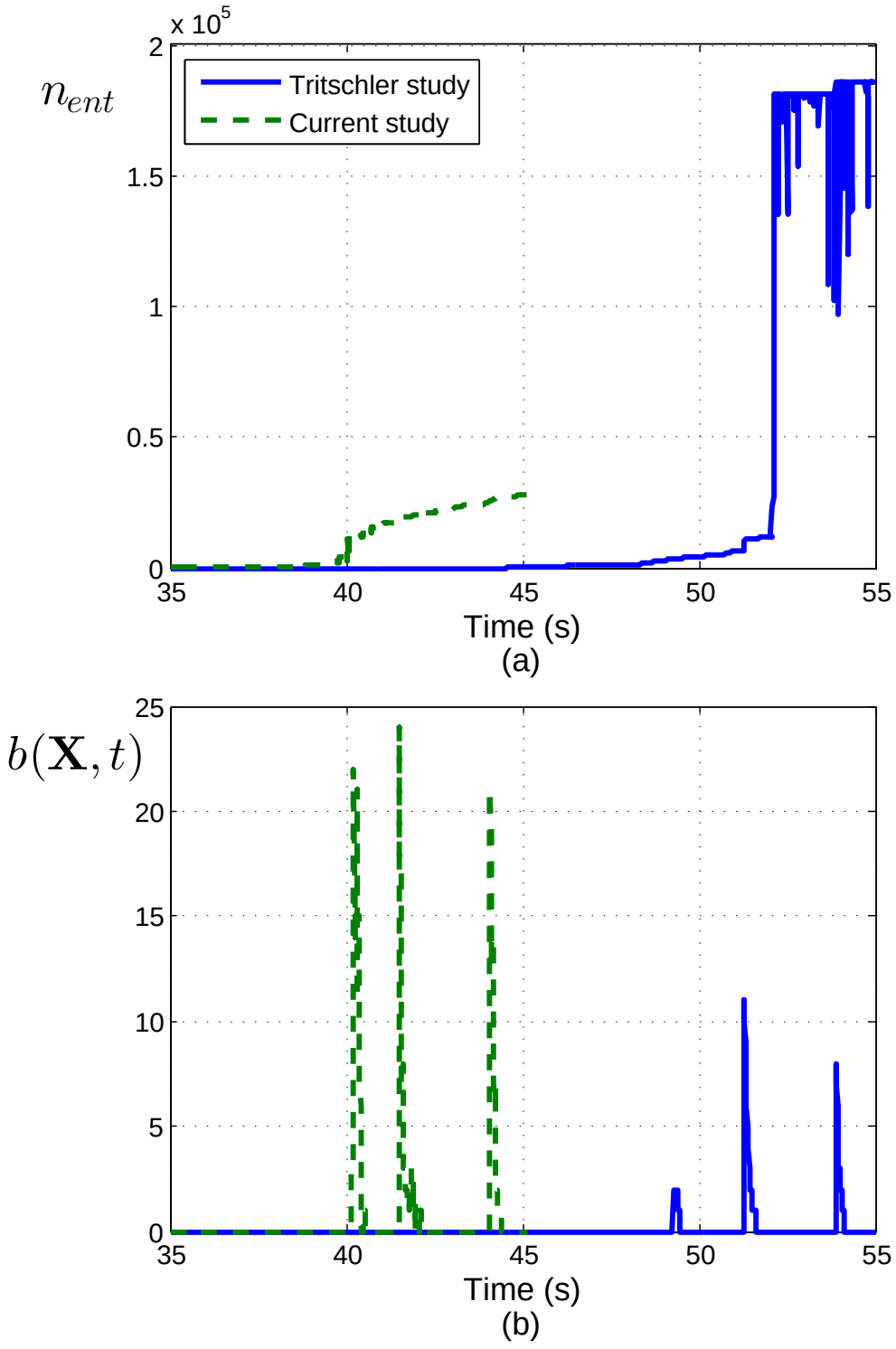

Figure 3.42: Particle counts comparison during the simulations for the Tritschler study [2] and the current study for (a) the total number of particles entrained in the field and (b) the number of particles in the best region of the FOV ($b(\mathbf{X}, t)$.

entrained into the flow field than in the current study. However, when viewing the cloud geometry in Fig. 3.40(a), the majority of these uplifted particles are lining the ground and are barely in the flow field. To further look into the differences of particle counts the number of particles in the best region of the FOV $b(\mathbf{X}, t)$ was plotted against time in Fig. 3.42(b). From this it can be seen that about 1.5 times more particles are in the best region of the FOV for the current study than there were in Tritschler's study. This small difference in particles leads to the conclusion that even though the total number particles entrained overall in the Tritschler study is greater, that the current study is still comparable, as the quantity of particles in the best region of the FOV do not differ by huge quanties.

Differences in the dust cloud geometries between the two studies can be explained by investigating the velocity field, which is detailed in Fig. 3.43, with Fig. 3.43(a)–(e) showing the velocity fields in time for the Tritschler global optimum and Fig. 3.43(f)–(j) showing the results for the global optimum of the current study. The time scales between the two cases are different, and the time noted at each stage is relative only to itself and cannot be compared. As shown in Figs. 3.43(a) and (f), when the blade tip vortices initially impinge on the ground the position of the ground vortex differs. The ground vortex in Tritschler's study (see Fig. 3.43(a)) begins to form relatively close to the rotor tip at about 20 ft. forward of the rotor, however, in the current study (see Fig. 3.43(f)) the ground vortex forms more inboard, around 5 ft forward of the rotor. This difference in initial ground vortex position is a consequence of the tilt of each rotor, respectively. The rotor is tilted backwards (nose-up) in Tritschler's case, which allows the blade tip vortices to con-

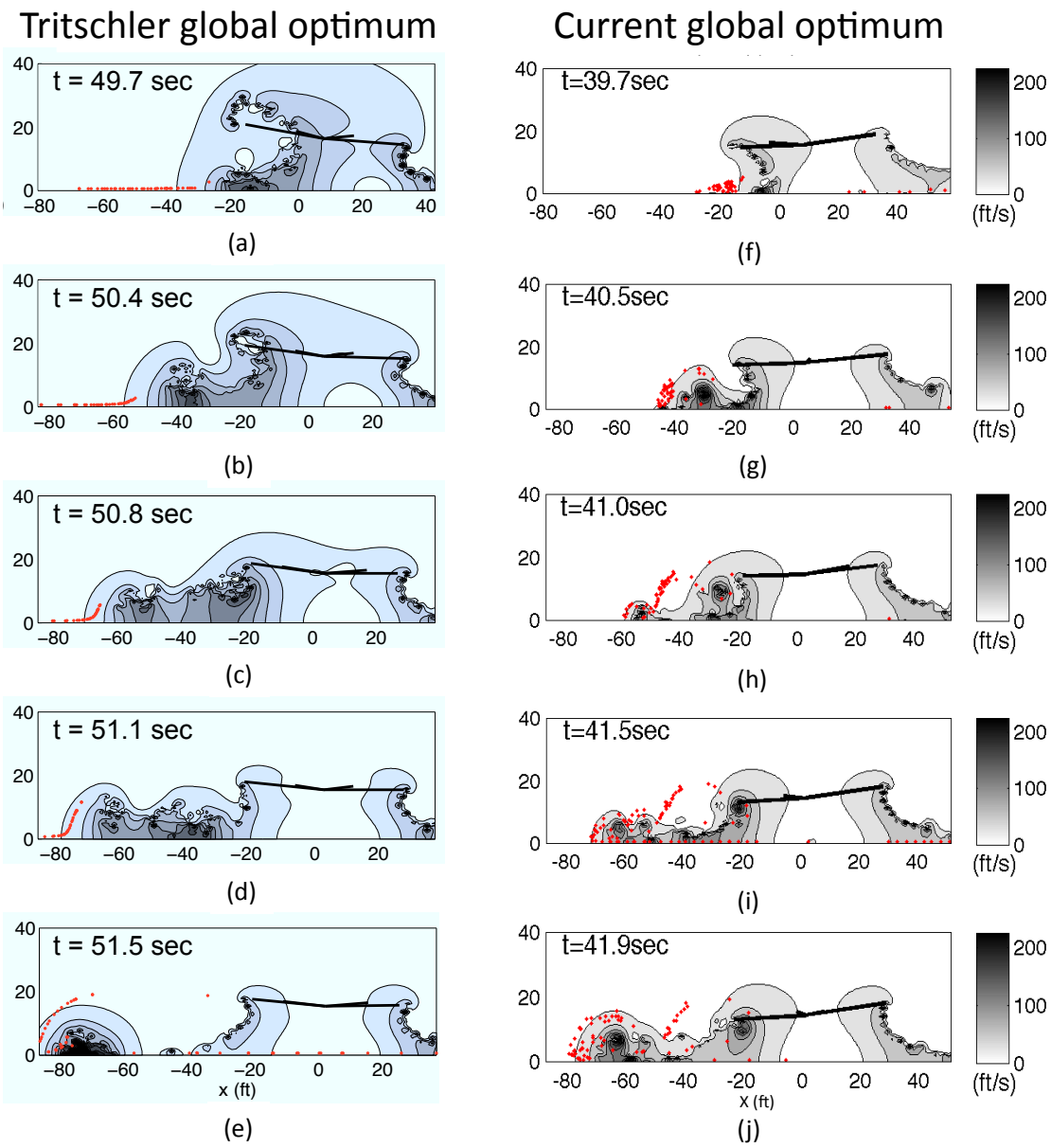

Figure 3.43: Realizations of the velocity magnitudes and developing cloud in a longitudinal plane through the flow field for (a)–(e) the Tritschler global optimum, and (f)–(j) the current study's global optimum. The motion of the rotor over the ground is from right to left. Particles are enlarged for illustrative purposes.

vect down and away from the rotor. In the current study, the rotor is tilted forwards (nose-down) so the blade tip vortices convect down and inwards initially.

The location of the initial ground vortex is important in determining how close to the rotor the dust particles are when they are uplifted by the flow. The ground vortex with in the Trischler global optimum convects outwards faster (Figs. 3.43(b)–(d), than is seen in the current global optimum (Fig.s 3.43(g)–(i) because it is formed further from the rotor. As the ground vortex restructures, the uplifted particles in the Tritschler study (Fig. 3.43(e)) are about 70 ft forward of the rotor where they are less likely to be recirculated in the rotor flow. In the current study (Fig. 3.43(j)), particles had previously been recirculated before the ground vortex had restructured farther away, and so more particles are uplifted closer to the rotor and could be reingested.

Most of these flow field differences, and hence the differences in the dust clouds, can be attributed to the forward tilt of the rotor. As briefly discussed in an earlier chapter, the forward tilt in landing is required to satisfy the moment balance needed to reduce airspeed to zero. The rotor model used in the Tritschler study was an isolated rotor and did not include a fuselage. Moreover, this simplified trim model did not balance the moments. The pitch profile provided in the Tritschler study was based on a formulation that took into account body acceleration and velocity, but not any forces or moments, and thereby was able to land in hover with only a slight pitch up. In the current set up of the helicopter, the fuselage center of gravity (CG) is behind the main rotor CG. To balance the pitch moment the rotor tip-path-plane will be tipped forwards. Additionally, the model has a 3° pre-tilt

angle that increases the tip path plane forward tilt.

It is this separation of the fuselage and rotor CG's that leads back to Fig. 3.39(b) and the differences that can be seen pitch angle maximums and final values of the pitch. Tritschler's optimization study defines pitch angle as the shaft tilt angle. Because the model has no fuselage model, this is also considered the pitch of the rotorcraft body. In comparison, the flight dynamics model has a fixed shaft tilt angle, and the pitch angle is defined as the pitching of the fuselage. The larger maximum pitch angles that are seen in the current study can be associated again with the fuselage CG being behind the rotor CG. To slow the rotorcraft to a hover it is required that the rotor thrust is directed so that all moments are zero. For the moments to be zero the fuselage must orient itself such that its CG is directly underneath the rotor CG. Because the fuselage CG is behind the rotor CG the fuselage must pitch backwards (nose-up) an additional amount to obtain zero the pitching moment, hence creating the higher pitching angles seen in the current study. Furthermore, instead of returning to zero once the helicopter has reached hover, the fuselage must remain slightly nose-up to keep the fuselage CG beneath that of the rotor, accounting for the non-zero fuselage pitch angles seen at the end of the simulation.

The CG of the main rotor for this exemplar single rotor helicopter in the current study is at 341 inches. The longitudinal fuselage CG position for the global optimum (and the rest of the optimization simulation) had been placed at 361 inches, which is also the farthest aft CG position recommended in [16]. To delve further into the effect that the longitudinal CG position has on the resulting brownout cloud an additional case with the CG was placed at the most fore recommended

longitudinal position, 345 inches [16]. The velocity flow field and the dust cloud that it produces are shown in Fig. 3.44(f)–(j), and are compared to the velocity flow field and dust cloud of the case with the CG in the most aft position in Fig. 3.44(a)–(e). Notice that the most fore recommened CG position is still slightly behind the main rotor CG. The extra case was simulated using the same approach profile as the CG aft position case, with all parameters being the same except for the CG position. Because the approach profiles are the same for both cases, the times used for comparison are the same.

The flow fields develop for both cases similarly. The most pronounced difference between the cases is a slight difference in rotor tilt throughout the manuever. When the blade tip vorticies begin to impinge on the ground in Figs. 3.44(a) and (f) both rotors in both cases have a forward tilt, and the resulting flow fields are similar. However, as time moves forwards the rotor in the CG fore position case can be seen to move back into a more neutral (with no tilt) position (see Figs. 3.44(g)-(j)). This difference in rotor tilt is no more than three degrees. As the flow fields develop, the ground vortex in the CG fore case appear to break into two smaller vortices (see Fig. 3.44(g)), while in the CG aft case the ground vortex remains as one vortex (see Fig. 3.44(b)). From this separation of the initial ground vortex in the CG fore case, the particles are uplifted about 10 ft farther away from the main rotor than in the CG aft case (see Figs. 3.44(h), (i) and (c), (d) respectively). Even though it appears that there is more reingestion of the particles through the rotor in the CG fore case, the space between the rotor and the "ring" structure created by the dust is larger by about 20 ft (see Figs. 3.44(j) and (e)). This larger space results in a less dense

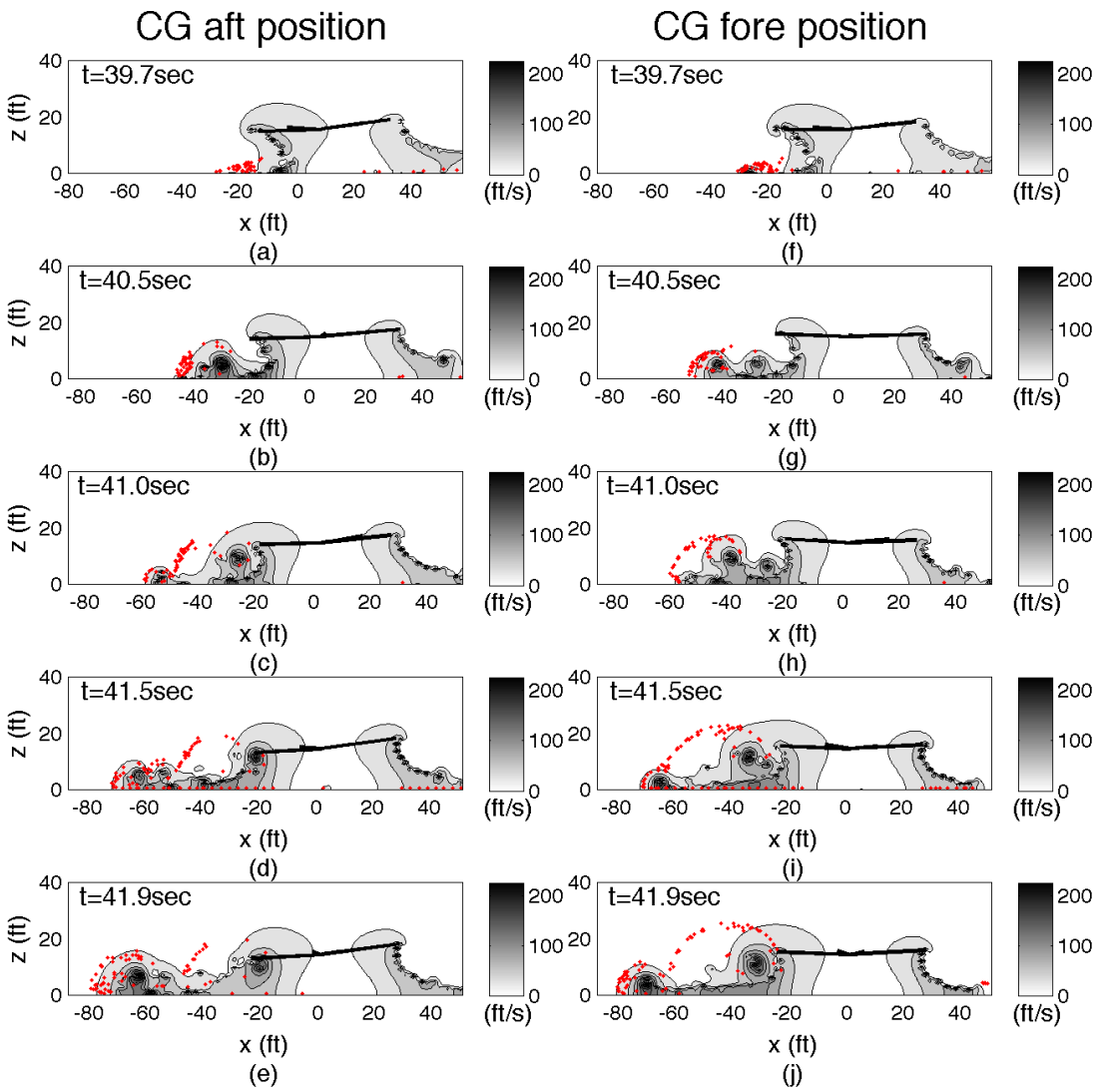

Figure 3.44: Realizations of the velocity magnitudes and developing cloud in a longitudinal plane through the flow field for (a)–(e) the CG aft position case, and (f)–(j) the CG fore position case. The motion of the rotor over the ground is from right to left. Particles are enlarged for illustrative purposes.

cloud in the pilot's FOV.

A further comparison of the quantity of particles entrained into the flow fields for each CG simulation is shown in Fig. 3.45. From Fig. 3.45(a), it can be seen that the total number of particles entrained into the flow field is less by a factor of about 2 times for the CG fore case. However, in Fig. 3.45(b) it is observed that the CG fore case produces slightly more particles in the initial spike of particles in the best region of the pilot's FOV than the CG aft case. It is possible that there is a trade off between total particles entrained overall and the number of particles in the pilot's FOV that comes with changing the position of the CG, and hence changing the final tilt of the rotor.

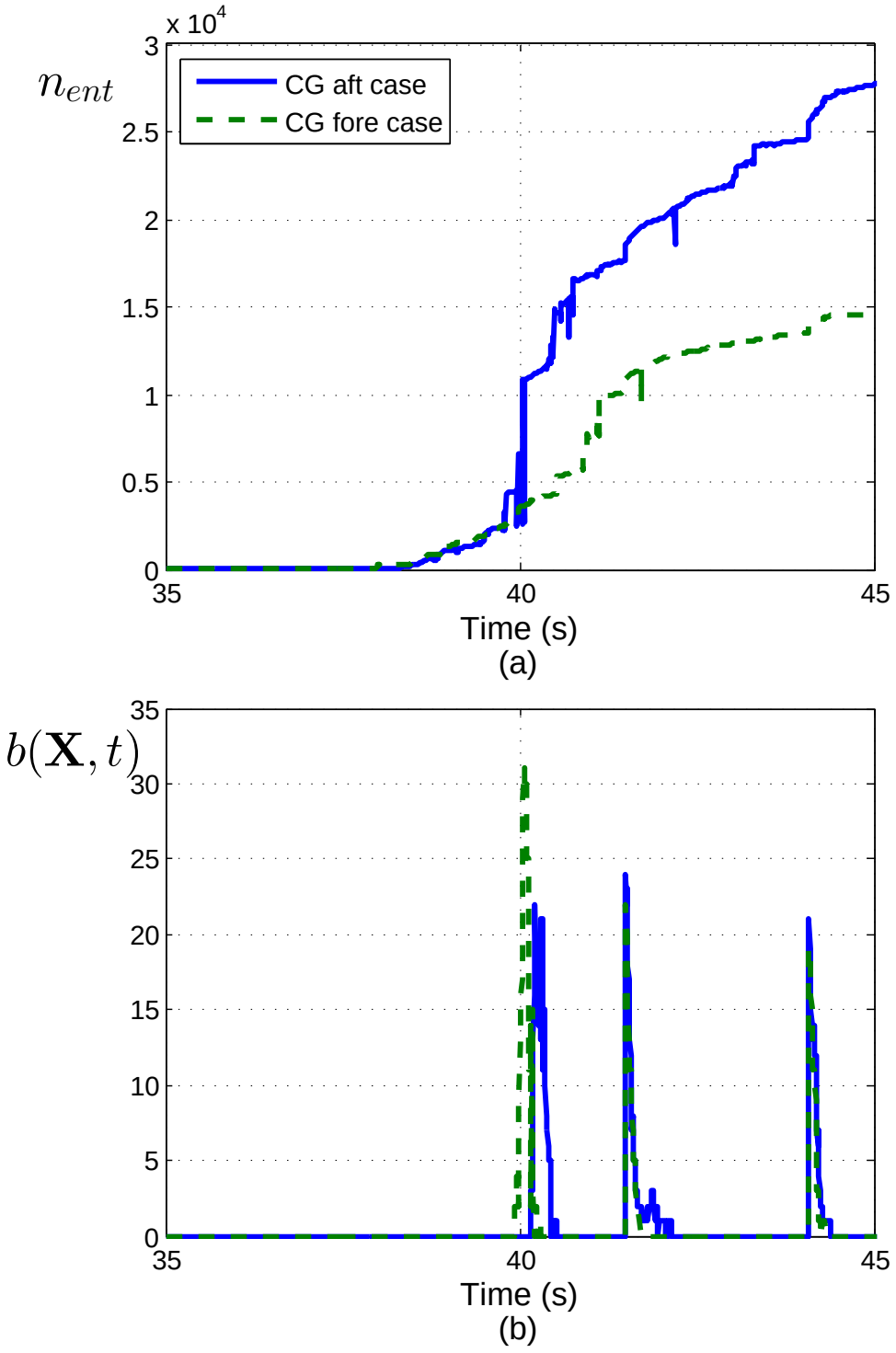

Figure 3.45: Particle counts comparison during the simulations for the CG aft position study and the CG fore position study for (a) the total number of particles entrained in the field and (b) the number of particles in the best region of the FOV ($b(\mathbf{X}, t)$.

Chapter 5

Conclusions and Future Work

In this thesis, a free-vortex method model was coupled with a sophisticated rotorcraft flight dynamics model. A method for approach profile following was developed, and integrated into the coupled model. This model was then used to perform a brownout mitigation study through flight path optimization by using the methodology from a previous mitigation study performed by Tritschler [2].

5.1 Conclusions

From the results obtained during this study, the following conclusions have been drawn:

1. The new approach used to trim with the coupled model is more accurate and computationally efficient than the previous method. By allowing the model to trim for fixed inflow at each step then updating the inflow based on the new trim variables, an extra layer of convergence was established. This processed guaranteed that the final wake geometries would be evaluated from the final trim variables, and also eliminated unnecessary function calls to the wake that slowed the trim convergence timing.

2. A simple method for controlling the states was presented. It was demonstrated that it is possible to use a controller the state variables to track on a specified

approach profile. An accurate actual trajectory resulted from customizing the controller for the flight condition at each time step. In addition, with this method the pilot stick inputs remained inside a reasonable range that is realistic relative to their actual limits.

3. The design space for the approach profile optimization proved itself to be non-convex and contained at least two optima. The optimization resulted in local and global optimum of shallow and steep angles respectively. The results are consistent with the approaches found by the Tritschler study, which are also consistent with current operational strategies used by pilots who encounter (or may encounter) brownout conditions.

4. While the optimum approaches found were very similar to that of the Tritschler study, the characteristics of the resulting brownout cloud and flow field were changed by the use of a higher-fidelity flight dynamics model. The addition of a fuselage to the simulation changed the position of the center of gravity of the aircraft, and hence changed the rotor tip-path-plane pitch angle. The difference in rotor pitch angle caused the blade tip vortices to impinge on the ground more inboard of the rotor than during the Tritschler study, resulting in the dust particles being uplifted closer to the main rotor. The forward pitching of the rotor also resulted in greater fuselage pitch up angles seen during the maneuver. Furthermore, changing the CG of the helicopter changes the characteristics of the resulting brownout cloud.

5. The results of the current study further validate Tritschler's conclusion that

the ground vortex is very important to the formation of a brownout dust cloud.

5.2 Recommendations for Future Work

As this study encompassed many disciplines including rotorcraft dynamics modeling, free-vortex modeling, brownout simulation, and optimization, there are many possible directions for future work to move. Based on the results and conclusion of the current study, some recommendations for future work are as follows:

1. While this study found two local optimums, it is possible that because the design space is clearly non-convex more optimums exist in other areas. A further optimization needs to be performed to more greatly explore the design space in order to see if any other optimums exist that are less operationally accepted or known. This study could be further expanded to study the effects of the fuselage center of the gravity on the formation of a brownout dust cloud. Additionally, the brownout simulation framework can be extended to other optimizations, such as rotor design and fuselage design. This framework could also be applied to an optimization of where in the fuselage to place the CG.

2. Other opportunities exist for the use of the approach profiling formulation. The approach profile could be utilized to model the profile required to land if, for example, a one-engine inoperative condition. The engine out case could be placed into an optimization framework and find an optimal landing approach profile for this case.

3. The current approach profile simulation lacks a pilot model, which results in unrealisticly quick stick control movements. This behavior is not as realistic in terms of pilot reaction, and so the addition of a pilot model would add the more smooth motions of a human operator. A more realistic set of controls could be incredibly important as it could provide a pilot with more comprehensive directions to operate the helicopter in conditions such as brownout or an engine inoperative.

Appendix A

Building the Approach Profile Following Controllers Example

The following section gives an example of the building process of a controller. For brevity, only the condensed rigid body matrix $\mathbf{A}_1$ and $\mathbf{B}_1$ (see Eq. 2.5.3 are shown here. The case shown here is for a flight path angle of 6° and a flight velocity of 60 kts.

The condensed rigid body $\mathbf{A}_1$ and $\mathbf{B}_1$ matrices are shown below.

$$\mathbf{A}_1 = \begin{bmatrix} 0 & 0 & 0 & 1.00 & -0.04 & 0.04 & 0 & 0 & 0 & 0.44 & 10.58 & 0 \\ 0 & 0 & 0 & 0.04 & 1.00 & 0 & 0 & 0 & 0 & -14.36 & 0.44 & 100.71 \\ 0 & 0 & 0 & -0.04 & 0 & 1.0 & 0 & 0 & 0 & -4.17 & -100.63 & \\ 0 & 0 & 0 & -0.02 & 0 & 0.04 & -1.40 & -11.93 & -4.52 & 0 & -32.15 & 0 \\ 0 & 0 & 0 & 0 & -0.08 & -0.01 & 13.71 & -0.21 & -98.95 & 32.15 & 0 & 0 \\ 0 & 0 & 0 & -0.09 & -0.01 & -0.62 & 12.15 & 99.51 & 2.85 & 0 & -1.21 & 0 \\ 0 & 0 & 0 & -0.01 & -0.06 & 0.04 & -3.92 & -0.38 & 0.04 & 0 & 0 & 0 \\ 0 & 0 & 0 & -0.01 & 0.01 & 0.01 & 0.19 & -1.48 & -0.18 & 0 & 0 & 0 \\ 0 & 0 & 0 & 0 & 0 & 0.01 & -0.01 & -0.28 & 0.01 & -0.52 & 0 & 0 \\ 0 & 0 & 0 & 0 & 0 & 0 & 1.00 & 0 & 0.04 & 0 & 0 & 0 \\ 0 & 0 & 0 & 0 & 0 & 0 & 0 & 1.00 & 0 & 0 & 0 & 0 \\ 0 & 0 & 0 & 0 & 0 & 0 & 0 & 0 & 1.00 & 0 & 0 & 0 \end{bmatrix} \tag{A.1}$$

$$\mathbf{B}_1 = \begin{bmatrix} 0 & 0 & 0 & 0 \\ 0 & 0 & 0 & 0 \\ 0 & 0 & 0 & 0 \\ 0.02 & -1.22 & 0.58 & 0.79 \\ 0.35 & 0.02 & 0.17 & -1.05 \\ 0.63 & -2.26 & -7.86 & 1.67 \\ 1.17 & 0.20 & 0.41 & -0.63 \\ -0.02 & 0.42 & 0.14 & -0.07 \\ 0.07 & -0.01 & 0.01 & 0.41 \\ 0 & 0 & 0 & 0 \\ 0 & 0 & 0 & 0 \\ 0 & 0 & 0 & 0 \end{bmatrix} \tag{A.2}$$

The $\mathbf{Q}$ and $\mathbf{R}$ matrices used for the LQR controller for the 6° set are:

$$\mathbf{Q}_6 = \text{ diag}\left(\begin{bmatrix} .0001 & .0001 & .0001 & 10 & 1 & 1 & 100 & 100 & 100 & 10 & 1000 & 100 \end{bmatrix}\right) \tag{A.3}$$

$$\mathbf{R}_6 = 8 \begin{bmatrix} 1 & 0 & 0 & 0 \\ 0 & 1 & 0 & 0 \\ 0 & 0 & 1 & 0 \\ 0 & 0 & 0 & 1 \end{bmatrix} \tag{A.4}$$

The resulting LQR controller $\mathbf{K}$ for this example is:

$$\mathbf{K} = \begin{bmatrix} 0 & 0.01 & 0 & 0.12 & 0.07 & 0.12 & 2.29 & 1.23 & 0 & 3.42 & -3.97 & 4.349 \\ 0 & 0 & 0 & -1.08 & 0.01 & 0.07 & 0.47 & 9.84 & 2.65 & 0.14 & 22.43 & 0.28 \\ 0 & 0 & 0 & -0.18 & 0.04 & -0.26 & 0.27 & -0.92 & 0.66 & 1.59 & 13.70 & 1.61 \\ 0 & 0 & 0 & 0.01 & -0.31 & -0.03 & -1.65 & -0.60 & 10.63 & -3.04 & -0.20 & 1.13 \end{bmatrix} \tag{A.5}$$

Additionally, the $\mathbf{Q}$ and $\mathbf{R}$ matrices for the 0° and 12° sets, respectively, are:

$$\mathbf{Q}_0 = \text{ diag}\left(\begin{bmatrix} .0001 & .0001 & .0001 & 1 & 10 & 1 & 100 & 100 & 1000 & 10 & 1000 & 1000 \end{bmatrix}\right) \tag{A.6}$$

$$\mathbf{R}_0 = 11.5 \begin{bmatrix} 1 & 0 & 0 & 0 \\ 0 & 1 & 0 & 0 \\ 0 & 0 & 1 & 0 \\ 0 & 0 & 0 & 1 \end{bmatrix} \tag{A.7}$$

$$\mathbf{Q}_{12} = \text{diag}\left(\begin{bmatrix} .00008 & .0001 & .00001 & 10 & 1 & 10 & .1 & 10 & .1 & 10 & 1000 & 100 \end{bmatrix}\right) \tag{A.8}$$

$$\mathbf{R}_{12} = 20 \begin{bmatrix} 1 & 0 & 0 & 0 \\ 0 & 1 & 0 & 0 \\ 0 & 0 & 1 & 0 \\ 0 & 0 & 0 & 1 \end{bmatrix} \tag{A.9}$$

Bibliography

[1] Mapes, P., Kent, R., Wood, R.,"DoD Helicopter Mishaps FY85-05: Findings and Recommendations," U.S. Air Force, 2008.

[2] Tritschler, J., *Contributions to the Characterization and Mitigation of Rotorcraft Brownout*, Ph.D. Dissertation, University of Maryland, 2012.

[3] Syal, M., *Development of a Lagrangian-Lagrangian Methodology to Predict Brownout Dust Clouds*, Ph.D. Dissertation, University of Maryland, 2012.

[4] Johnson, B., Leishman, J. G., and Sydney, A., "Investigation of Sediment Entrainment Using Dual-Phase, High-Speed Particle Image Velocimetry," *Journal of the American Helicopter Society*, Vol. 55; (4), October, 2010, pp. 042003 1–16.

[5] Sydney, A., Baharani, A., and Leishman, J. G., "Understanding Brownout using Near-Wall Dual-Phase Flow Measurements," American Helicopter Society International 67th Annual Forum Proceedings, Virginia Beach, VA, May 3–5, 2011.

[6] Milluzzo, J., Sydney, A., Rauleder, J., and Leishman, J. G., "In-Ground-Effect Aerodynamics of Rotors with Different Blade Tips," American Helicopter Society International 66th Annual Forum Proceedings, Phoenix, AZ, May 11–13, 2010.

[7] Shao, Y., Raupach, M. R., and Findlater, P. A., "Effect of Saltation Bombardment on the Entrainment of Dust by the Wind," Journal of Geophysical Research, Vol. 98, No. D7, February 1993, pp. 12,719–12,726.

[8] Lu, H., and Shao, Y., "A New Model for Dust Emission by Saltation Bombardment," *Journal of Geophysical Research*, Vol. 104; No. D14, July 1999, pp. 16,827–16,842.

[9] Shao Y., "A Model for Mineral Dust Emission," Journal of Geophysical Research, Vol. 106, No. D17, September 2001, pp. 20,239–20,254.

[10] Syal, M., Govindarajan, B., and Leishman, J. G., "Mesoscale Sediment Tracking Methodology to Analyze Brownout Cloud Developments," American Helicopter Society International 66th Annual Forum Proceedings, Phoenix, AZ, May 11–13, 2010.

[11] Hu, Q., Gumerov, N., Duraiswami, R., Syal, M., and Leishman, J. G., "Toward Improved Aeromechanics Simulations Using Recent Advancements in Scientific Computing," American Helicopter Society International 67th Annual Forum Proceedings, Virginia Beach, VA, May 3–5, 2011.

[12] Kalra, T. S., Lakshminarayan, V. K., and Baeder, J. D., "CFD Validation Of Micro Hovering Rotor In Ground Effect," American Helicopter Society International 66th Annual Forum Proceedings, Phoenix, AZ, May 11–13, 2010.

[13] Thomas, S., Lakshminarayan, V. K., Kalra, T. S., and Baeder, J. D., "Eulerian-Lagrangian Analysis of Cloud Evolution using CFD Coupled with a Sediment Tracking Algorithm," American Helicopter Society International 67th Annual Forum Proceedings, Virginia Beach, VA, May 3–5, 2011.

[14] Syal, M., Rauleder, J., Tritschler, J. K., and Leishman, J. G., "On the Possibilities of Brownout Mitigation Using a Slotted-Tip Rotor Blade," 29th AIAA Applied Aerodynamics Conference Proceedings, Honolulu, HI, June 27–30, 2011.

[15] Cheng, R., *A High-Ordered, Linear Time-Invariant Model for Application to Higher Harmonic Control and Flight Control System Interaction*, Ph.D. Dissertation, University of Maryland, 2003.

[16] Howlett, J. J., "UH-60A Black Hawk Engineering Simulation Program - Volume II - Mathematical Model," NASA CR-166309, December 1981.

[17] Ballin, M. G., "Validation of a Real-Time Engineering Simulation of the UH-60A Helicopter," NASA TM-88360, 1987.

[18] Kim, F. D., Celi, R., and Tischler, M. B., "High Order State Space Simulation Models of Helicopter Flight Mechanics," *Journal of the American Helicopter Society*, Vol. 38, No. 2, October 1993.

[19] Kim, F. D., Celi, R., and Tischler, M. B., "Forward Flight Trim Calculation and Frequency Response Validation of a High-Order Helicopter Simulation Model," *Journal of Aircraft*, Vol. 30, No. 6, November-December 1993.

[20] Turnour, S. R. and Celi, R., "Modeling of Flexible Blades for Helicopter Flight Dynamics Applications," Journal of the American Helicopter Society, Vol. 41, No. 1, January 1996.

[21] Celi, R., "Helicopter Rotor Blade Aeroelasticity in Forward Flight with an Implicit Structural Formulation," *AIAA Journal*, Vol. 30, No. 9, September 1992.

[22] Spence, A. M., *A Design-Oriented Aeromechanical Analysis for Hingeless Rotor Helicopters in Straight and Turning Flight*, Ph.D. Dissertation, Department of Aerospace Engineering, University of Maryland, College Park, MD, 1994.

[23] He, C. J. and Peters, D. A., "Optimization of Rotor Blades for Combined Structural, Performance, and Aeroelastic Characteristics," *Structural Optimization*, Vol. 5, No. 1/2, December 1992.

[24] Leishman, J. G. and Q., N. K., "State Space Representation of Unsteady Airfoil Behavior," *AIAA Journal*, Vol. 28, No. 5, May 1990.

[25] Theodore, C. and Celi, R., "Flight Dynamic Simulation with Refined Aerodynamic and Flexible Blade Modeling," Proceedings of the 56th Annual Forum of the American Helicopter Society, Virginia Beach, VA, May 2000.

[26] Bagai, A. and Leishman, J. G., "Rotor Free-Wake Modeling using a Relaxation Technique - Including Comparisons with Experimental Data," Proceedings of the 50th Annual American Helicopter Society Forum, Washington D.C., May 1994.

[27] Fusato, D., *Design Sensitivity Analysis and Optimization for Helicopter Handling Qualities Improvement*, Ph.D. Dissertation, University of Maryland, 2002.

[28] Ribera, M., *Helicopter Flight Dynamics Simulation with a Time-Accurate Free-Vortex Wake Model*, Ph.D. Dissertation, University of Maryland, 2007.

[29] Leishman, J. G., Bhagwat, M. J., and Bagai, A., "Free-Vortex Filament Methods for the Analysis of Helicopter Rotor Wakes," Journal of Aircraft, Vol. 39, No. 5, September-October 2002, pp. 759–775.

[30] Juhasz, O., Celi, R., Tischler, M., Ivler, C., "Flight Dynamic Simulation Modeling of Large Flexible Tiltrotor Aircraft," 68th Annual Forum of the American Helicopter Society, Fort Worth, TX, May 1-3, 2012.

[31] Theodore, C. R., *Helicopter Flight Dynamic Simulation with Refined Aerodynamic Modeling*, Ph.D. Dissertation, University of Maryland, 2000.

[32] Bhagwat, M. J., and Leishman, J. G., "Accuracy of Straight-Line Segmentation Applied to Curvilinear Vortex Filaments," Journal of the American Helicopter Society, Vol. 46, (2), April, 2001, pp. 166–169.

[33] Weissinger, J., "The Lift Distribution of Swept-Back Wings," NACA TM 1120, 1947.

[34] Ananthan, S., *Analysis of Rotor Wake Aerodynamics During Maneuvering Flight Using a Free-Vortex Wake Methodology*, Ph.D. thesis, University of Maryland, 2006.

[35] Bhagwat, M. J., *Mathematical modeling of the Transient Dynamics of Helicopter Rotor wakes Using a Time-Accurate Free-Vortex Method*, Ph.D. thesis, University of Maryland, 2001.

[36] Bhagwat, M. J., and Leishman, J. G., "Time-Accurate Modeling of Rotor Wakes Using A Free-Vortex Wake Method," 18th AIAA Applied Aerodynamics Conference Proceedings, Denver, CO, August, 2000.

[37] Celi, R., "Helicopter Rotor Dynamics in Coordinated Turns," Journal of the American Helicopter Society, Vol. 36, No. 4, October 1991, pp. 39–47.

[38] More, J. J., Garbow, B. S., and Hillstrom, K. E.,*Users Guide for MINPACK-1.* Argonne National Laboratory, Report ANL-80-74, August 1980.

[39] Athans, M. and Falb, P. L., *Optimal Control*, McGraw-Hill, New York, 1966.

[40] McRuer, D., Graham, D., and Ashkenas, I., *Aircraft Dynamics and Automatic Control*, Princeton University Press, 1973.

[41] Aoyama, Y., and Nakano, J., *RS/6000 SP: Practical MPI Programming*, IBM Red- books, 1999.

[42] Anonymous, "NVIDIA CUDA C Programming Guide," Version 4.1, NVIDIA, 2011.

[43] Heffley, R. K., "A Model for Manual Decelerating Approaches to Hover," 15th Annual Conference on Manual Control Proceedings, November, 1979, pp. 545–554.

[44] Rash, C. E., McLean, W. E., Mozo, B. T., Licina, J. R., and McEntire, B. J., "Human Factors and Performance Concerns for the Design of Helmet-Mounted Displays," 37th European Rotorcraft Forum Proceedings, Gallarate (VA), Italy, September 13–15, 2011.

[45] Hoh, R. H., "Investigation of Outside Visual Cues Required for Low Speed and Hover," 12th AIAA Atmospheric Flight Mechanics Conference Proceedings, Snowmass, CO, August 19–21, 1985, pp. 337–349.

[46] Drees, J. M., and Hendal, W. P., "Airflow Patterns in the Neighborhood of Helicopter Rotors," Aircraft Engineering, Vol. 23, (266), 1951, pp. 107–11.

[47] Leishman, J. G., *Principles of Helicopter Aerodynamics*, Cambridge University Press, New York, NY, 2nd ed., 2006.

[48] Vanderplaats, G. N., "Approximation Concepts for Numerical Airfoil Optimization," Technical Paper 1370, NASA, 1979.

[49] Vanderplaats, G. N., *Numerical Optimization Techniques for Engineering Design: With Applications*, McGraw-Hill, New York, NY, 1984.

[50] Kufeld, R. M., Balough, D. L., Cross, J. L., Studebaker, K. F., and Jennison, C. D., "Flight Testing of the UH-60A Airloads Aircraft," Proceedings of the American Helicopter Society 50th Annual Forum, Washington D.C., May 1994.